UNIVERSITY OF CALIFORNIA
Santa Barbara

“Growth and Characterization of Aluminum Gallium Nitride/ Gallium Nitride Ultraviolet Detectors”

A dissertation submitted in partial satisfaction
of the requirements for the degree of

Doctor of Philosophy

in

Electrical and Computer Engineering

by

Giacinta Parish

Committee in charge:

Professor Umesh K. Mishra, Chairperson
Professor Steven P. DenBaars
Doctor James P. Ibbetson
Professor Brett D. Nener
Professor James S. Speck

March 2001

The dissertation of Giacinta Parish is approved

Committee Chairperson

March 2001

March 2001

Acknowledgments

The opportunity to be at one of the foremost research universities in the world for GaN research is one I will always be grateful for, and there are many people who inspired, guided and assisted me. I want to thank my adviser Umesh Mishra for accepting me to be one of his students. Thank you for all your support and guidance during my time at UCSB. It has been both an educational and enjoyable experience to work in the Mishra Group at UCSB. This was reinforced by the fantastic collaborative atmosphere and the many talented people in the extended solid-state research community at UCSB.

The members of my defense committee all had constructive and helpful advice and information for me. As head of the MOCVD lab Steve DenBaars had constant contact and input into my work in GaN and AlGaN growth. I benefited greatly from the insights and suggestions of James Ibbetson, both while he was also working in the MOCVD lab at UCSB, and when he moved to Cree Lighting. I am very grateful to Jim Speck for his knowledge of and assistance in materials characterization. And, although Brett Nener was on the other side of the world at the University of Western Australia, emails, phone calls and several visits to UCSB ensured he was also a constant source of support and help.

To Stacia Keller I owe more gratitude than I can express, for teaching me so much about MOCVD, and for the extent of research into AlGaN growth that we accomplished together.

I'm also glad to have shared the experience with my fellow students in the Mishra Group. To Can Zheng, Dan Green, DJ Jena, Huili Xing, James Champlain, Jeff Yen, Lee McCarthy, Likun Shen, Naiqian Zhang, Peter Kozodoy, Prashant Chavarkar, Primit Parikh, Rama Vetury, Rob Coffie, Rob Underwood, Sten Heikman, Tim Wisleder and Yifeng Wu – thank you all for your companionship and your collaboration. And to the members of the York Group who shared our office – Amit Nagra, Bruce Liu, Jane Xu, Nick Cheng, Paolo Maccarini, Pengcheng Jia, and Vicki Chen – I offer the same thanks. Similarly to the many students and researchers in the MOCVD group who I have shared with, been helped by, and learned from all these years – Amber Abare, Andreas Stonas, Beck Mason, Bernd Keller, Brendan Moran, Dave Kapolnek, Greg Fish, Hugues Marchand, Mike Craven, Mike Mack, Monica Hansen, Patrick Abraham, Paul Fini, Tal Margalith and Tom Katona– thank you all. To the gang at The University of Western Australia I am also indebted. They got me to UCSB, they helped me along the way with offshore advice, simulations, and data, and they brought me home: thank you Laurie Faraone, John Dell, Charlie Musca, Joe Jin Kuek, Sabine Betts, Dave Pulfrey at UBC, and all the rest of the crew. There are many others who have made the journey to this point possible with their support and assistance. In the MOCVD lab it was Brian Carralejo, and in the cleanroom Jack Whaley, Bob Hill and Mike Anzlowar, all of you have my unending gratitude. For administrative support and so much more – thank you Cathy Fogarty, Lee Baboolal, Joann Erving and Val De Veyra. And thanks to the guys in the electrical engineering workshop - Bob Stevenson, Avery Juan and Raul Ramirez. I wish to especially thank Eric Tarsa at Cree Lighting for his important input into this work with the design of the solar-blind detector. I am also grateful to Lifan Chen for TEM measurements, to Professor Joe Campbell and his student Charles Collins at UT Austin for the final responsivity measurements, and to Siegfried Fleischer for his invaluable help in creating the spectral and temporal response measurement setups.

To Jason my dear darling supportive husband: I don't know what it would have been like doing this without you. You always believed in me, even more than I did. Thank you for your patience, love and endless encouragement. To mum and dad the same is true. Your support has made a huge difference in reaching this point and I will always be grateful. And to all my and Jason's family and friends – thank you all.

Finally I would like to acknowledge the financial support from the Office of Naval Research and the Air Force Office of Scientific Research that made this work possible. I would also like to acknowledge the fellowships that enabled me to attend UCSB - the Fulbright fellowship from the Australian-American Fulbright Association and the Hackett Scholarship from the University of Western Australia.

Vita

June 29, 1972	Born (Giacinta Matassa) — Perth, Australia
March 1995	B. Eng., Electronic. — The University of Western Australia
March 1995	B. Sc., Chemistry — The University of Western Australia
1995-96	Teaching Assistant — Department of Electrical and Electronic Engineering, The University of Western Australia
March 1997	M. Eng. Sc. — The University of Western Australia
1996-2000	Research Assistant — Department of Electrical and Computer Engineering, University of California, Santa Barbara

Publications

1. D.L. Pulfrey, J.J. Kuek, M.P. Leslie, B.D. Nener, G. Parish, U.K. Mishra, P. Kozodoy and E.J. Tarsa, "High UV/solar rejection ratios in GaN/AlGaN/GaN p-i-n photodiodes" *IEEE Trans. on Electron Device.* **48**(3) 100-2 (2001).

2. G. Parish, M. Hansen, B. Moran, S. Keller, S.P. DenBaars and U.K. Mishra, "AlGaN/GaN solar-blind ultraviolet photodiodes on SiC substrate" *Proc. IEEE CORNELL* Ithaca, USA, 215-24 (2000).

3. S. Keller, G. Parish, J.S. Speck, S.P. DenBaars and U.K. Mishra, "Dislocation reduction in GaN films through selective island growth of InGaN" *Appl. Phys. Lett.*, **77**(17), 2665-7 (2000). *J. Appl. Phys* **87**(8) 3900-4 (2000)

4. N.Q. Zhang, S. Keller, G. Parish, S. Heikman, S.P. Denbaars and U.K. Mishra, "High breakdown GaN HEMT with overlapping gate structure" *IEEE Electron Device Lett.* **21**(9) 373-5 (2000)

5. E. J. Tarsa, P. Kozodoy, J. Ibbetson, B. P. Keller, G. Parish and U. K. Mishra, “Solar-blind AlGaN-based inverted heterostructure photodiodes” *Appl. Phys. Lett.*, **77**(3), 316-8 (2000).

6. G.A. Umana-Membreno, J.M. Dell, Y.-F. Wu, G. Parish and U.K. Mishra, "Anomalous drain current-voltage characteristics in AlGaN/GaN MODFETs at low temperatures" *Microelectronics Journal* **31**(7) 531-6 (2000)

7. J. Antoszewski, M. Gracey, J.M. Dell, L. Faraone, T.A. Fisher, G. Parish, Y.-F. Wu and U.K. Mishra, "Scattering mechanisms limiting two-dimensional electron gas mobility in $Al_{0.25}Ga_{0.75}N$/GaN modulation-doped field-effect transistors" *J. Appl. Phys* **87**(8) 3900-4 (2000).

8. G. Parish, S. Keller, S. P. DenBaars and U. K. Mishra, “SIMS Investigations into the effect of growth conditions on residual impurity and silicon incorporation in GaN and $Al_xGa_{1-x}N$” *J. Electron. Mater.* **29**(1), 15-20 (2000).

9. D. L. Pulfrey, J. J. Kuek, B. D. Nener, G. Parish, U. K. Mishra, E. J. Tarsa “Towards an AlGaN, solar-blind, p-i-n photodetector” *Phys, Stat. Sol. (A)* **176**, 169-73 (1999)

10. S, Keller, G. Parish, P. T. Fini, S. Heikman, C.-H. Chen, N. Zhang, S. P. DenBaars and U. K. Mishra, “Metalorganic chemical vapor deposition of high mobility AlGaN/GaN heterostructures” *J. Appl. Phys.* **86**(10), 5850-7 (1999).

11. G. Parish, S. Keller, P. Kozodoy, J. P. Ibbetson, H. Marchand, P. T. Fini, S.B. Fleischer, S. P. DenBaars, U. K. Mishra and E.J. Tarsa, “High-performance (Al,Ga)N-based solar-blind ultraviolet p-i-n detectors on laterally epitaxially overgrown GaN” *Appl. Phys. Lett.* **75**(2), 247-9 (1999).

12. C.-H. Chen, K. Krishnamurthy, S. Keller, G. Parish, M. Rodwell, U. K. Mishra and Y.-F. Wu, “AlGaN/GaN dual-gate modulation-doped field-effect transistors” *Electron. Lett.* **35**(11), 933-4 (1999).

13. J. J. Xu, Y.-F. Wu, S. Keller, G. Parish, S. Heikman, B. J. Thibeault, U. K. Mishra and R. A. York, “1-8-GHz GaN-based power amplifier using flip-chip bonding” *IEEE Microwave Guided Wave Lett.* **9**(7), 280-1 (1999).

14. G.A. Umana-Membreno, J.M. Dell, L. Faraone, Y.-F. Wu, G. Parish and U.K. Mishra, "Anomalous drain current-voltage characteristics in AlGaN/GaN MODFETs at low temperatures" *Proc. SPIE* **3893** 454-60 (1999).

15. G. Parish, S. Keller, P. Kozodoy, J. P. Ibbetson, H. Marchand, P. T. Fini, S.B. Fleischer, S. P. DenBaars, U. K. Mishra and E.J. Tarsa, “Low dark current p-i-n (Al,Ga)N-based solar-blind UV detectors on laterally epitaxially overgrown GaN” *Proc. IEEE COMMAD* Perth, Australia, 175-8 (1998).

16. G. Parish, S. Keller, P. T. Fini, R. Vetury, C.-H. Chen, S. P. DenBaars, U. K. Mishra and Y.-F. Wu, “MOCVD growth and properties of thin $Al_xGa_{1-x}N$ layers on GaN” *Proc. IEEE COMMAD* Perth, Australia, 478-81 (1998).

17. G. A. Umana-Membreno, J. M. Dell, B. D. Nener, L. Faraone, G. Parish, Y.-F. Wu and U. K. Mishra, “Low temperature shallow-trap related output-admittance frequency dispersion in AlGaN/GaN MODFETs” *Proc. IEEE COMMAD* Perth, Australia, 252-5 (1998).

18. J. Antoszewski, M. Gracey, J. M. Dell, L. Faraone, G. Parish, Y.-F. Wu and U. K. Mishra, “Magneto-transport studies in AlGaN/GaN MODFETs” *Proc. IEEE COMMAD* Perth, Australia, 256-9 (1998).

19. C.-H. Chen, S. Keller, G. Parish, R. Vetury, P. Kozodoy, E. L. Hu, S. P. DenBaars, U. K. Mishra and Y.-F. Wu, “High-transconductance self-aligned AlGaN/GaN modulation-doped field-effect transistors with regrown ohmic contacts” *Appl. Phys. Lett.* **73**(21), 3147-9 (1998).

20. R. Vetury, H. Marchand, G. Parish, P. T. Fini, J.P. Ibbetson, S. Keller, J. S. Speck, S. P. DenBaars and U. K. Mishra, “First demonstration of AlGaN/GaN heterostructure field effect transistor on GaN grown by lateral epitaxial

overgrowth (LEO).” *Proc. 25th Intl. Symp. Compound Semicond.* Nara, Japan 177-83 (1998).

21. R. Vetury, Y.-F. Wu, P. T. Fini, G. Parish, S. Keller, S. P. DenBaars and U. K. Mishra, “Direct measurement of gate depletion in high breakdown (405V) AlGaN/GaN heterostructure field effect transistors” *Proc IEEE IEDM* San Francisco, USA 55-8 (1998).

22. C. A. Musca, J. F. Siliquini, G. Parish, J. M. Dell and L. Faraone, “A monolithic dual-band HgCdTe infrared detector” *J. Cryst. Growth* **184-185**, 1284-7 (1998)

23. G. Parish, “Development of a monolithic dual-band HgCdTe infrared detector structure”, *Unpublished M. Eng. Sc. Thesis*, (1997) The University of Western Australia, Perth, Australia.

24. G. Parish, C. A. Musca, J. F. Siliquini, J. Antoszewski, J. M. Dell, B. D. Nener, L. Faraone and G. J. Gouws, “A monolithic dual-band HgCdTe infrared detector structure” *IEEE Electron Device Lett.* **18**(7), 352-4 (1997)

25. G. Parish, C. A. Musca, J. F. Siliquini, J. Antoszewski, J. M. Dell, B. D. Nener, L. Faraone and G. J. Gouws, “Fabrication and modelling of a prototype dual-band HgCdTe infrared detector structure” *Proc. IEEE COMMAD* Canberra, Australia, 46-9 (1996).

Abstract

Growth and Characterization of Aluminum Gallium Nitride/Gallium Nitride for Ultraviolet Detectors

by Giacinta Parish

There are many areas of potential utilization of the alloy $Al_xGa_{1-x}N$, not the least of which are ultraviolet detector applications. These include flame and heat sensors, missile plume detection, and secure-from-earth inter-satellite communications. The $Al_xGa_{1-x}N$ bandgap can be tailored from 4.3eV (x_{Al}=0) to 6.2eV (x_{Al}=1), corresponding to a band-edge wavelength range of 365nm to 200nm, to suit each unique application. Solar radiation below approximately 300nm wavelength is absorbed by ozone in the atmosphere. Thus, for applications in the presence of a large solar radiation background, a *solar-blind* detector that exhibits no spectral response for wavelengths at or above 300nm is extremely desirable. For solar-blind detectors a composition of greater than 30% Al is needed.

The first phase of this work involved the optimization of metalorganic chemical vapor deposition epitaxial growth of $Al_xGa_{1-x}N$ ($x_{Al} \geq 0.3$) on GaN templates. It was found that defect formation in the $Al_xGa_{1-x}N$ is exacerbated as x_{Al} is raised. This could be partially counteracted by maximizing the mobility of Al surface species during growth, and by reducing threading dislocation density in the GaN template.

The second phase of the work examined the effect of defects on GaN-based p-i-n photodiodes. The presence of threading dislocations (especially mixed-character dislocations) was found to increase the leakage current, broaden the spectral response, and lengthen the response decay time. Defects in the i-layer, most likely point defects, were another source of leakage current. The sidewalls did not contribute to leakage current.

The final phase of the project was the development of bulk AlGaN growth on SiC substrates for use in solar-blind UV detectors. A nucleation layer or ramped growth rate was required to avoid cracking due to tensile strain. Si-doping of the n-type buffer introduced further tension in the film. The threading dislocation density in the AlGaN grown on SiC was very high – $2\text{-}5 \times 10^{10}$ cm^{-2} – much higher than for GaN. Because the threading dislocations were primarily edge-type, reasonably low diode leakage currents could still be obtained. An insulating buffer was required to suppress photocurrent contributions from the SiC substrate. Solar-blind p-GaN/ i-AlGaN/n-AlGaN photodiodes with a peak responsivity of 0.08 A/W were fabricated.

Table of contents

Chapter 1. Introduction

GaN and its alloys with InGaN and AlGaN form a wide-bandgap semiconductor material system with numerous optical and electronic device applications. The wavelength range spans from 1.9eV (InN) to 6.2eV (AlN), covering the technologically important ultraviolet (UV) and visible spectral ranges. Also, due to the wide bandgap and high bond strength the material has a high chemical and radiation resistance. With no semiconductor material previously satisfying commercial demands for blue, green and UV lasers and light-emitting devices this has been the first immediate focus of GaN research and progress. With a high breakdown field and large predicted electron saturation velocity, GaN-based materials are also suited for high power, high frequency transistors for microwave applications. In this area commercial potential is close to being realized. The spectral range, which has been utilized with success for light emitting devices, can also be exploited for detectors. The bandgap of $Al_xGa_{1-x}N$ can be tailored to fulfill many UV detector applications better than the commercially available alternatives. The development of AlGaN and GaN for UV detectors forms the subject of this thesis. The studies include both the effect of the material quality and of the device design on the UV detector performance. Material quality is a critical issue due to the relative immaturity of the GaN material technology.

1.1 Defects – dislocations (extended defects) and point defects

Although interest in GaN for its envisaged potential (as described above) began in the 1970's, significant progress was not made until the late 1980's and the 1990's. Only then did methods to overcome both the lack of a suitable substrate and the serious problems with point defects began to break through in the research community

1.1.1 Substrates

For GaN and its alloys the issue of device performance is interlinked with that of the high threading dislocation densities (10^7-10^9 cm^{-3}) present due to the lattice-mismatched substrates used. To this date there has been no successful technique devised for production of bulk GaN substrates of technologically suitable size. The most closely lattice-matched substrate of reasonable cost is sapphire. SiC is more closely matched, however is very costly.

The substrate used the most, with a compromise between lattice match and cost, has been sapphire. Amano and Akasaki and co-workers[1] made consistent growth of single crystal epitaxial GaN a reality with development of a two-layer deposition process. They first deposited a thin AlN nucleation layer at reduced temperatures, and then grew the epitaxial GaN on top. That opened the gate for the initial rush of GaN development in the early 90's. Despite the large generation of dislocations in the material to accommodate the lattice mismatch, much progress was made in device development in all areas. However to achieve the true potential of GaN and its alloys the dislocations, with their detrimental effects on device performance, must be eliminated.

Use of a silicon carbide substrate has also been investigated with the premise that the improved properties due to the closer lattice and thermal match will, in certain applications, justify the high cost of the substrate. This appears well founded in the case of high electron mobility transistors (HEMT's), where superior properties are consistently obtained on SiC, due not only to the better GaN epitaxial material but also to the better thermal conductivity of the SiC substrate[2,3].

The advent of lateral epitaxial overgrowth (LEO) heralded a new era of improvement for this material system. Selective epitaxy of GaN using SiO_2 masks had already been investigated for growth of pyramidal arrays for field emitters. Then in 1997 several groups reported on the reduced dislocation density in material grown laterally across the mask from the mask openings[4,5]. The revelation that this overgrown material was virtually dislocation-free spurred an explosion of research into optimization and utilization of the LEO technique. Nakamura et al., the first researchers to obtain commercially viable blue laser diodes using GaN-based materials, increased the lifetime of continuous wave operation of the laser to over 10,000 hours by using LEO substrates[6]. Kozodoy et al. were the first to demonstrate a side-by-side comparison of devices – GaN p-n diodes – on dislocated and LEO GaN from the same wafer[7]. The leakage current was dramatically reduced for the diodes on LEO with reduced threading dislocations. The following year UCSB also revealed improvements in the gate leakage current for high electron mobility transistors (HEMTs) on LEO GaN[8], and in leakage current, spectral responsivity, and response time for AlGaN/GaN UV photodiodes on LEO GaN. This latter work will be discussed in Chapter 3.

LEO involves a processing step and at least one regrowth step, and is therefore not the ultimate solution for the future of commercial GaN devices. Instead it is a stepping-stone, a simulation of when, ultimately, there will be a bulk GaN substrate. Currently this goal does seem obtainable, through the use of Halide Vapor Phase Epitaxy (HVPE), but there is a long way to go yet.

1.1.2 Impurities and doping

As well as the issues surrounding the threading dislocations in epitaxial GaN, point defects have been another critical issue, mostly because of the high n-type background carrier concentration and difficulties in p-type doping. Both native defects and residual impurities have been investigated. Carbon and oxygen are the most common impurities in III-V semiconductors. Sources of the impurities in metalorganic chemical vapor deposition (MOCVD) growth are numerous and include the carrier gases, air exposure during wafer loading and leaks in the gas handling system. In addition, the precursors themselves can be contaminated. Oxygen impurities related to the precursor synthesis, particularly of TMAl, have caused problems for a long time. In addition, metal-organic precursors intrinsically contain carbon. In the case of group-III nitrides, the ammonia purity is another critical issue, as water is a significant impurity, again as a result of the synthesis process.

Carbon and oxygen impurities in group-III nitrides have been associated with both deep and shallow levels. For example, the source of the n-type background carrier concentration in as-grown GaN is a subject of much debate[9]. Although possible that it is due to nitrogen vacancies[10,11], there is also a great deal of support for the view that it is in fact due to impurities such as oxygen[12,13,14,15,16]. Oxygen is believed to be a shallow donor in GaN, with a transition to a DX-like state under hydrostatic pressure or with increasing Al content[4,17,18]. Carbon, an amphoteric impurity in (Al)GaN, is predicted to be a shallow acceptor when incorporated on a nitrogen site. This, according to the theoretical calculations, is energetically favorable over incorporation on Ga site due to the large differences in the atomic radii.[19] However, experimental findings have implied a link between carbon impurities and the yellow luminescence commonly observed in GaN, which has been attributed to a transition from a shallow donor to a deep acceptor (E_c- 860 meV). [20,21] Carbon impurities are also believed to be a source of donor compensation[22]. The persistent photoconductivity effect observed in GaN-based devices has also been linked to impurities[23,24].

Hydrogen impurities, also inherent to the MOCVD process both as a carrier gas and in the precursors, are the primary reason p-type doping of GaN could not be achieved until 1988. Again, it was the work of Amano et al., which led the way to success[25]. They discovered that the dopant Mg, which had hitherto not produced the expected p concentrations, was activated after electron beam irradiation. It has been found that hydrogen content in p-GaN limits the effectiveness of the Mg atoms, although the exact nature of the complexes causing this is unknown[26,27]. It was revealed by Nakamura[28] that annealing the p-type material in a N_2 ambient could also activate the material. Much work has been done at UCSB, particularly by Kozodoy[29], to optimize this process for our material and device development.

Silicon is known to be a shallow donor in GaN and is commonly used as an n-type dopant. Though less troublesome than Mg, it has also suffered from compensation effects, which again have been linked to the residual impurities C and O[19].

1.2 AlGaN-based devices

High-x_{Al} $Al_xGa_{1-x}N$ (referring, for the purposes of this dissertation, to $x_{Al} \geq 0.3$) devices have only been pursued in the latter part of the 90's. The first AlGaN photodetectors were not reported until 1996[30,31], and high-x_{Al} HEMTs (higher than 25% Al) were not reported until 1998[32]. By far the most published interest in AlGaN-based devices has been for HEMTs, with the first published observation of a two-dimensional electron gas (2DEG) by Asif Khan et al. in 1992[33] for an $Al_xGa_{1-x}N$/GaN heterostructure (for x_{Al} = 0.04 – 0.25). They then demonstrated their first HEMT in 1994[34].

One reason for the keen interest in AlGaN/GaN HEMTs, besides the high breakdown and robust nature of the material, is the extremely large charge density of the 2DEG formed at the AlGaN/GaN interface. The charge density, n_s, is formed even without modulation doping in the AlGaN, with the source of the charge believed to be surface donor(s)[35]. The large 2DEG is enabled by polarization-induced charge at the AlGaN/GaN interface. GaN and AlN are believed to contain sizeable spontaneous polarization[36]. They also possess high piezoelectric constants, leading to substantial piezoelectric polarization in strained films. For MOCVD-grown AlGaN/GaN heterostructures on sapphire (for which the AlGaN is under tensile strain), the spontaneous and piezoelectric polarizations are in the same direction. At the AlGaN/GaN interface the discontinuity in polarization induces a very high positive sheet charge. This enables the large 2DEG charge density at the AlGaN/GaN interface. The strong polarization-induced fields at the interface also ensure that the 2DEG is very tightly bound.

The initial work in this thesis involved optimization of AlGaN growth within the context of an AlGaN/GaN HEMT structure, before moving onto UV detectors. Whilst Khan et al. had demonstrated the first HEMT, it was UCSB which played a leading role in pushing the performance through improving the nature of the GaN insulating buffer[37], modifying device dimensions[38], and increasing x_{Al}[32]. Flip-chip bonding provided additional improvements[39,40], as well as an extensive study into the growth and doping of the AlGaN layers[41,42]. This latter aspect formed part of this dissertation and will be discussed in detail in Chapter 2. Combining all these improvements with the additional thermal management and defect improvement obtained by growth on a SiC substrate, the best reported results to date for AlGaN/GaN HEMTs were obtained recently by Cree Lighting[43] with a power density of 9.8 W/mm and a power added efficiency of 47% at 8.2 GHz.

1.3 (Al)GaN photodetectors

$Al_xGa_{1-x}N$ is an attractive candidate for many UV detector applications, including flame and heat sensors, missile plume detection, secure-from-earth inter-satellite communications, UV calibration and monitoring devices for medical and biological applications, and other commercial applications such as plasma diagnostics and engine monitoring. These roles have primarily been filled in the past by photomultiplier tubes and Si detectors. The photomultiplier tubes are inefficient and inferior to semiconductor devices. Si has a narrow bandgap (1.1eV) and therefore requires filtering to operate as a UV detector. In contrast the bandgap of $Al_xGa_{1-x}N$ can be tailored between 3.4 and 6.2eV. This provides an obvious advantage over Si, as filtering can be bulky and/or expensive. The robustness of $Al_xGa_{1-x}N$ also offers the potential for stable device operation in hostile environments. SiC, although similar in robustness to GaN, has a bandgap of 2.9eV, narrower than GaN, and no potential to tailor the bandgap through alloying. Therefore SiC detectors would also require filtering for many UV applications.

Another advantage of $Al_xGa_{1-x}N$ over Si and SiC is its direct bandgap - Si and SiC have indirect bandgaps. An electron transition between the top of the valence band and the bottom of the conduction band in an indirect-gap semiconductor requires a change not just in the electron energy but in the electron momentum as well. Thus the absorption process will require participation not just of a photon and an electron but of a phonon (or phonons) as well. For light energies well above the bandgap this can be accomplished relatively efficiently by a vertical excitation of the electron to high in the conduction band. This is followed by a relaxation to the bottom of the conduction band through transfer of momentum to phonons. However, closer to the bandgap energy a phonon is required for momentum transfer as part of the non-vertical excitation process. Because three bodies must participate, the likelihood of absorption becomes less at wavelengths closer to the bandgap.

The external quantum efficiency of a photodetector is proportional to the absorption coefficient:

$$\eta = (1 - R)\zeta\left[1 - \exp(-\alpha d)\right] \tag{1.0}$$

Here η is the quantum efficiency, R the optical power reflectance at the surface, ζ the fraction of electron-hole pairs generated that actually contribute to photocurrent, α the absorption coefficient and d the depth of the photodetector. Due to the absorption processes described above, the absorption coefficient and hence the quantum efficiency of an indirect-gap semiconductor gradually decreases as the illumination energy approaches the bandgap energy. The spectral response of the detector therefore drops off earlier and more gradually than it would with a direct-gap semiconductor. For a direct-gap semiconductor the response peaks at the bandgap energy and then drops off rapidly as the absorption coefficient sharply drops for sub-bandgap illumination.

1.3.1 Photodetectors

There are two significant categories of semiconductor photodetectors – photoconductive, for which an increase in conductivity is measured due to photon-generated carriers, and photovoltaic, for which photon-generated carriers can contribute to current via a charge-separating junction (a depletion region). The most common type of photovoltaic detector is the p-n or p-i-n junction photodiode. Another common type is the Schottky barrier (SB) photodiode, in which the depletion region is due to a Schottky contact to p- or n-type bulk material. These three types of detector – photoconductor, p-i-n photodiode, and SB photodiode, are represented schematically in Figure 1.1. In the figures the impinging light is assumed to have energy $h\nu > E_G$, the bandgap of the semiconductor. Thus absorption in the semiconductor creates photogenerated electrons (open circles) and holes (filled circles).

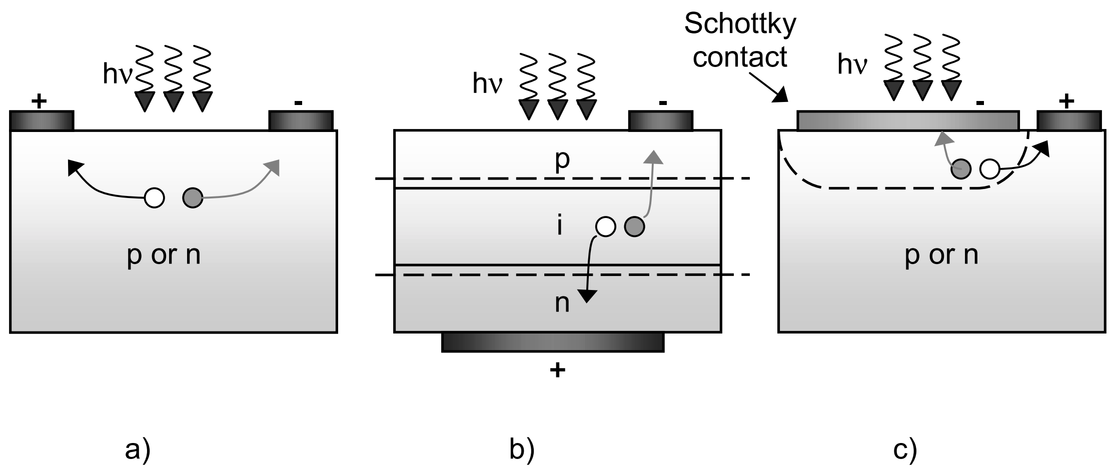

Figure 1.1 Schematic of photogenerated carriers in a a) photoconductor, b) p-i-n photodiode and c) Schottky barrier photodiode. The electrons (open circles) and holes (filled circles) are created by absorption of light with $h\nu > E_G$.

The photoconductor, in Figure 1.1a, is essentially a resistor, with an applied bias at the ohmic contacts used to separate the photogenerated electrons and holes and measure the corresponding photocurrent. In the photodiodes, the main photocurrent contribution is from photogenerated carriers in the depletion region (between the dashed lines in Figure 1.1b and between the dashed line and the Schottky contact in Figure 1.1c), which are separated by the electric field and recombine in the bulk regions or at the contacts. In all types of semiconductor photodetector the mechanism of absorption of above-bandgap energy light to create photocurrent means that the bandgap energy of the semiconductor determines the region of operation (visible, infrared, ultraviolet) of the detector. As will be discussed in Section 1.3.2, the bandgap range of $Al_xGa_{1-x}N$ is ideally suited for ultraviolet detectors.

Photoconductors have two major advantages - internal gain, and fabrication simplicity - over photovoltaic devices. However they require biasing, exhibit high dark, or leakage, currents, and furthermore are very slow when fabricated using GaN-based material. Schottky barrier diodes are potentially the fastest detectors, but suffer from worse leakage than p-i-n diodes due to the small barrier height, and also from lower efficiency due to the narrow depletion region, combined with the short diffusion lengths in GaN for carriers generated outside the depletion region. Thus p-i-n diodes (with the i region inserted to extend the depletion region and thus the high-field absorbing region of the detector) are the detectors of choice in this work.

There are a number of figures of merit used to indicate photodetector performance. The most fundamental of these is the *responsivity*, which measures detector output for a given input, and is defined as:

$$\Re = \frac{\text{signal output}}{\text{illumination input}} \quad . \tag{1.1}$$

Signal output is measured either as a voltage or a current, and input as the power of the target light-source, so that the conventional units of responsivity are V/W or A/W, respectively. In this work current responsivity is used, so that:

$$\Re = \frac{i_{photo}}{P_{\lambda}} = \frac{q\eta}{h\nu} \ , \tag{1.2}$$

in which i_{photo} is the photocurrent, P_{λ} the illumination power at wavelength λ (frequency ν), and η the external quantum efficiency of the device. The energy of the illumination increases with wavelength, and so therefore does the responsivity of the detector. Due to the detection mechanism by photon absorption, photons of energy less than the bandgap E_G will not be absorbed. Thus there is a *cutoff wavelength*, λ_c, beyond which the responsivity will be zero. There is further variation in responsivity due to the convention of using input power in the calculation. The number of photons per incident watt increases with wavelength so that R also increases with wavelength until λ_c is reached.

Most other detector parameters are defined in terms of noise. Noise is electrical output other than the desired detector signal, and can be either external (electrical interference, amplifier noise) or fundamental to the detection process, such as the non-constant arrival of photons, non-photonic generation and recombination of carriers (such as thermal generation and recombination at traps), and random carrier motion in the detector.

A commonly used figure of merit for photodiode noise is the zero-bias *dynamic resistance*, R_o, of the device (measured in the absence of illumination), usually given as R_oA, where A is the area of the detector. In this work the currents near zero bias were too low to be measured and so R_o could not used for evaluation of noise. Instead the dark current measured in the absence of illumination is quoted; referred to as the *leakage current*, J_L, which is a measure of the noise at reverse bias (in order for sufficient sensitivity of the device the leakage current must be much lower in magnitude than the photocurrent). Most other reports of GaN and AlGaN UV detectors in the literature also use this parameter. In the case of a wide-bandgap semiconductor such as GaN and AlGaN the leakage current is expected to be limited by surface leakage and/or space-charge region effects[44].

Realistic assessment of the detector sensitivity requires consideration of both the responsivity and the noise of the detector. The *Noise Equivalent Power (NEP)* is the ratio of the two:

$$NEP = \frac{I_N}{\Re} \,, \tag{1.4}$$

in which I_N is the root-mean-square (rms) noise current. However, this figure is still dependent on the area of the diode.

Another figure of merit discussed in this work and in the literature is the *response time* of the diode. The response time is usually limited by either the RC time constant of the detector + circuit or the charge carrier lifetimes. The response time τ will limit the bandwidth of the circuit:

$$\Delta f = \frac{1}{2\pi\tau} \tag{1.5}$$

In this study the speed of interest was the fall time of the detector response – the decay rate of the signal output after illumination ceases, rather than the rise time of the signal output after illumination initiates. For GaN-based detectors this has been the more difficult parameter to control, as will be seen below.

The ultimate measure of detector performance is the *Specific Detectivity*, which is independent of the detector area, A, and combines the responsivity, noise performance and bandwidth of the detector:

$$D^{*} = \frac{\sqrt{A\,\Delta f}}{NEP} \tag{1.6}$$

The larger D* is, the better the detector. When the detector is limited by thermal noise the detectivity becomes[45]:

$$D^{*} = \frac{q\eta}{h\upsilon}\sqrt{\frac{R_o A}{4kT}} \tag{1.7}$$

Thus a high R_o is desirable for high detectivity. Because R_o could not be measured, detectivity figures could not be calculated for the detectors presented in this thesis.

1.3.2 What is solar-blind operation?

Of the various UV detector applications, many require detection of the target UV signal in the presence of the immense background radiation signal of the sun. Within a certain wavelength range the UV radiation from the sun is absorbed by the ozone in the earth's atmosphere and does not reach the earth's surface. Figure 1.2[46] indicates this, with a comparison between the extraterrestrial solar radiation (above atmosphere) and the solar radiation at the earth's surface (below atmosphere). It can be seen that at around 300nm (energy 4.1eV) the amount of solar radiation reaching the earth's surface drops dramatically. A solar-blind detector, therefore, is one that only detects light below this wavelength. This energy falls within the range of bandgap energies spanned by $Al_xGa_{1-x}N$ (2.0-3.4eV), making it an ideal material candidate for such detectors.

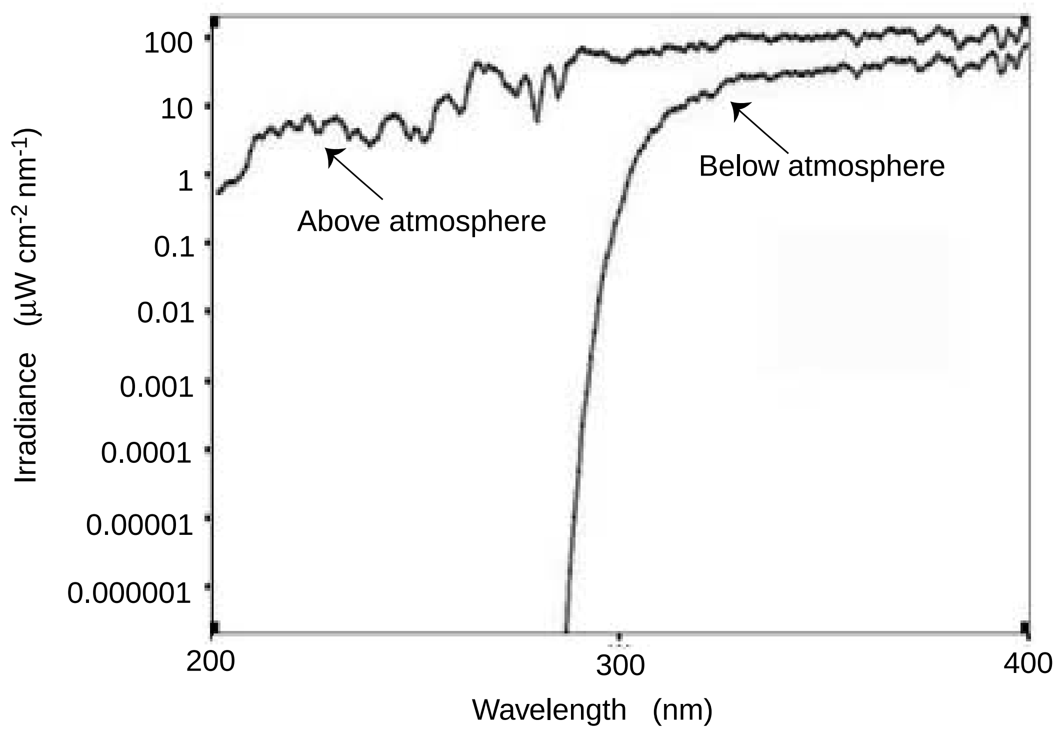

Figure 1.2 Solar UV irradiance at the top and the bottom of the earth's atmosphere (US 1976 standard atmosphere, 343 DU ozone, sun at zenith)[46].

Review papers have had some variation on what the exact upper limit for solar-blind character is – a paper summarizing UV detector requirements for AlGaN technology in 1997[47] gave 300nm as the upper limit, while a recent study by Schreiber et al of the US Airforce[48] states 280nm to be the upper limit. Using the earlier information, the solar-blind UV detectors in this study were designed to have a cutoff wavelength below 300nm; which necessitates an AlGaN composition of greater than 30%. With the revised definition of solar-blind limits a slight increase in composition will be necessary for future work.

1.3.3. Visible-blind GaN-based detectors

The first GaN UV detector of any merit was a GaN photoconductor published by Khan et al. in 1992[49]. The devices had extremely high gains (peak responsivity of 1000A/W at 5V bias) but also high response times (1ms), due to a very long minority carrier lifetime. In 1993 the same group published their first GaN SB photodiode[50]. The first GaN p-n photodiode papers were published in 1995, by two separate groups[51,52]. These first photovoltaic detectors also had slow response times (on the order of μs for the SB and ms for the p-n). The problems of slow response time and frequency- and power-dependence of responsivity experienced with the early photoconductive devices have persisted in most reported photoconductive devices[30,31,49].

Improvements in material have allowed corresponding advancement of device properties, particularly for the photovoltaic devices. SB devices have been recently reported with peak responsivity of 0.19A/W, leakage currents of 3nA/cm^2 at –5V and

RC-limited response times of 15ns[53], while SB diodes deposited on LEO GaN were reported with 1ns response time[54]. Visible-blind p-i-n photodiodes have been reported with responsivities of 0.1-0.2 A/W, leakage currents of 2-12 nA/cm^2 at –5V, and response times of 12-17ns[55,56,57,58]. Some of the groups utilized an $Al_xGa_{1-x}N$ layer for the n-layer to give a narrow-band response when backside illuminated. The use of a p-$Al_{0.1}Ga_{0.9}N$ instead of p-GaN also was shown to improve responsivity and speed[58,59]. Visible-blind GaN photodiodes have now reached such an acceptable stage of technology that the first visible blind UV camera using a 32x32 array of visible-blind p-GaN/i-GaN/n-$Al_{0.2}Ga_{0.8}N$ detectors has been reported[60].

1.3.4. Solar-blind AlGaN-based detectors

The first solar-blind detectors, reported in 1996 (by two separate groups), were simple AlGaN photoconductors, which suffered from the same long minority carrier lifetime-induced problems as GaN photoconductors, compounded by a high resistance of the films[30,31]. In 1998 Osinsky et al. reported the first solar-blind SB detector, with a peak responsivity of 0.07A/W at 290nm, but high leakage currents of 10μA/cm2 and slow response time of 1μs[61]. The following year, in collaboration with Cree Lighting (then Nitres, Inc.) we reported the first solar-blind p-i-n photodiode, with peak responsivities of 0.05A/W at 285nm and low leakage currents of 10nA/cm^2 at –5V and response times of 4.5-6.5ns, when deposited on LEO GaN templates[62]. These devices will be discussed in Chapter 3. Recently the focus in the GaN research community has shifted from visible-blind to solar-blind detectors, with many groups now improving material quality enough for realization of high quality AlGaN-based detectors. Several groups have achieved this by use of higher x_{Al}-buffers enabling both higher quality AlGaN detector layers (deposited on top), and filtering for backside illumination. Using this technique Karrer at al. reported the first fast AlGaN photoconductors, with no gain (responsivity of 0.1A/W at 300nm) and response times of 40ns[63], and Lambert et al. demonstrated p-i-n diodes with responsivity of 0.08 A/W at 278nm and leakage currents of 5nA/cm^2 at –5V, comparable to our results using LEO GaN[64]. The lowest leakage currents of 0.4-3.5nA/cm2 at -5 V were reported by Pernot et al., using a dislocation reduction technique involving an AlN interlayer (discussed in Chapter 2 and 3)[65]. However their responsivities were low, only 0.012A/W at 270nm, with slow response times of 17μs. Walker et al. also reported very high x_{Al} (0.7-0.9) AlGaN p-i-n detectors with a peak responsivity of 0.05A/W at 232 nm[66]. However the leakage currents were extremely high, 400μA/cm^2 at –10V. In their report no detail was given as to how growth of such thick high-x_{Al} structures was obtained, but these high leakage currents are an indication that the AlGaN was highly defective and possibly even cracked (the diodes were deposited on GaN templates).

1.4 Synopsis of this thesis

1.4.1 Chapter 2

With the requirement of solar-blind character of AlGaN-based detectors, the development of MOCVD growth of high-quality $Al_xGa_{1-x}N$ with x_{Al} of 0.3 or greater was a critical component of this dissertation. Chapter 2 details the development of

MOCVD growth of $Al_xGa_{1-x}N$ using sapphire substrates, with x_{Al} ranging from 0.2 to 0.65. The principles for MOCVD growth at UCSB are outlined, and some initial studies into bulk AlGaN growth are presented. This is followed by investigations into effect of growth conditions and x_{Al} on AlGaN morphology and 2DEG properties, which utilized thin AlGaN layers deposited on GaN base layers. Finally impurity incorporation as a function of x_{Al} and growth conditions will be discussed.

1.4.2 Chapter 3

Further to the studies of the AlGaN growth, are more fundamental studies regarding the ever-present threading dislocations in epitaxially grown GaN and AlGaN. In Chapter 3 several different studies of the effect of threading dislocations on photodiode characteristics are presented. The first study looks at the effect of different threading dislocation densities and makeup (screw, mixed, edge) on GaN p-i-n diode leakage current and spectral response. This includes presentation of a technique utilizing silicon nitride/InGaN interlayers to reduce edge dislocation density. Following that the leakage current in GaN p-i-n diodes with a reduced TDD is examined as a function of electric field/intrinsic layer thickness and diode size, to ascertain other causes of leakage current besides threading dislocations. Finally the photodetector characteristics (leakage current, spectral response, and pulsed response) of solar-blind p-GaN/i-AlGaN/n-GaN diodes are compared with and without threading dislocation reduction.

1.4.3 Chapter 4

In Chapter 4 further studies of the p-GaN/i-AlGaN/n-GaN solar-blind detector structure are presented, with a view to an improved device design. Moves are made to a detector with thicker i-AlGaN, and n-AlGaN instead of n-GaN. Unsuccessful investigations into dislocation reduction utilizing LEO techniques for bulk $Al_{0.35}Ga_{0.65}N$ are presented. This is followed by experiments into the growth of thick $Al_{0.35}Ga_{0.65}N$ on SiC substrate. This was undertaken with the belief that the benefits to detector performance, as well as the possibility of avoiding costly and time-consuming LEO, would outweigh the increase in substrate cost ensuing from the use of SiC. These experiments include studies of the nucleation technique and of the $Al_{0.35}Ga_{0.65}N$ growth conditions and doping, as well as attempts to reduced the high edge dislocation density by using Si_xN_y interlayers. Finally the results for solar-blind $Al_xGa_{1-x}N$ detectors grown on SiC substrates are presented, including a comparison of devices with and without a conducting buffer.

1.5 References

1. H. Amano, N. Sawaki, I. Akasaki, and Y. Toyoda, "Metalorganic vapor phase epitaxial growth of a high quality GaN film using an AlN buffer layer." *Appl. Phys. Lett*. **48**, 353-355 (1986).

2. S.T. Sheppard, K. Doverspike, W.L. Pribble, S.T. Allen, and J.W. Palmour, "High power GaN/AlGaN HEMTs on silicon carbide", *56th Annual Device Research Conference*, June 1998.

3. R. Gaska, J.W. Yang, A. Osinsky, Q. Chen, M. Asif Khan, A.O. Orlov, G.L. Snider, and M.S. Shur, “Electron transport in AlGaN-GaN heterostructures grown on 6H-SiC substrates.” *Appl. Phys. Lett.* **72,** 707-709 (1998).

4. T.S. Zheleva, H. Nam, M.D. Bremser, and R.F. Davis, “Dislocation density reduction via lateral epitaxy in selectively grown GaN structures.” *Appl. Phys. Lett.* **71,** 2472-2474 (1997).

5. D. Kapolnek, S. Keller, R. Ventury, R.D. Underwood, P. Kozodoy, S.P. Den Baars, and U.K. Mishra, “Anisotropic epitaxial lateral growth in GaN selective area epitaxy.” *Appl. Phys. Lett.* **71**, 1204-1206 (1997).

6. S. Nakamura, M. Senoh, S.I. Nagahama, N. Iwasa, T. Yamada, T. Matsushita, H. Kiyoku, Y. Sugimoto, T. Kozaki, H. Umemoto, M. Sano and K. Chocho, “InGaN/GaN/AlGaN-based laser diodes with modulation-doped strained-layer superlattices grown on an epitaxially laterally overgrown GaN substrate.” *Appl. Phys. Lett.* **72**, 211-213 (1998).

7. P. Kozodoy, J.P. Ibbetson, H. Marchand, P.T. Fini, S.Keller, J.S. Speck, S.P. Den Baars, and U.K.Mishra, “Electrical characterization of GaN *p-n* junctions with and without threading dislocations.” *Appl. Phys. Lett.* **73**, 975-977 (1998).

8. R. Vetury, H. Marchand, G. Parish, P. T. Fini, J.P. Ibbetson, S. Keller, J. S. Speck, S. P. DenBaars and U. K. Mishra, “First demonstration of AlGaN/GaN heterostructure field effect transistor on GaN grown by lateral epitaxial overgrowth (LEO).” *Proc. 25th Intl. Symp. Compound Semicond.* Nara, Japan 177-183 (1998).

9. W. Kim, A.E. Botchkarev, A. Salvador, G. Popovici, H. Tang & H. Morkoç, “On the incorporation of Mg and the role of oxygen, silicon and hydrogen in GaN prepared by reactive molecular beam epitaxy.” *J. Appl. Phys.* **82**, 219-226 (1997).

10. C.Y. Hwang, Y. Li, M.J. Schurman, W. E. Mayo, Y. Lu & R.A. Stall, “The role of impurities in LP-MOCVD grown gallium nitride.” *Mat. Res. Soc. Symp. Proc.*; **395**, 521-526 (1996).

11. A.Y. Polyakov, M. Shin, D.W. Greve, M. Skowronski & R. G. Wilson, "High resistivity $Al_xGa_{1-x}N$ layers grown by MOCVD." *MRS Internet J. Nitride Semicond. Res.* **1** (1996).

12. C.G. Van de Walle, C. Stampfl, and J. Neugebauer, "Theory of doping and defects in III-V nitrides." *J. Cryst. Growth* **189/190**, 505-510 (1998).

13. M. Topf, W. Kriegseis, W. Burkhardt, I. Dirnstorfer, D. Meister and B.K. Meyer, "Residual donors in GaN epitaxial films – a correlation of HALL effect, SIMS and photoluminescence data." *Mater. Sci. Forum* **264-268**, 1323-1326 (1998).

14. C. Stampfl and C.G. Van de Walle, "Doping of $Al_xGa_{1-x}N$." *Appl. Phys. Lett.* **72**, 459-461 (1998).

15. W. Seifert, R. Franzheld, E. Butter, H. Sobotta & V. Riede, " On the origin of free carriers in high-conducting n-GaN." *Cryst. Res. & Technol*. **18**, 383-390 (1983).

16. B.-C. Chung & M. Gershenzon, "The influence of oxygen on the electrical and optical properties of GaN crystals grown by metalorganic vapor phase epitaxy." *J. Appl. Phys.* **72,** 651-659 (1992).

17. C. Wetzel, H. Amano, I. Akasaki, T. Suski, J.W. Ager, E.R. Weber, E.E. Haller & B. K. Meyer," Localized donors in GaN: spectroscopy using large pressures." *Mat. Res. Soc. Symp. Proc.* **482**, 489-500 (1998).

18. M.D. McCluskey, N. M. Johnson, C.G. Van de Walle, D.P. Bour, M. Kneissl and W. Walukiewicz, "Metastability of oxygen donors in AlGaN." *Phys. Rev. Lett.* **80**, 4008-4011 (1998).

19. P. Boguslawski and J. Bernholc, "Doping properties of C, Si and Ge impurities in GaN and AlN." *Phys. Rev. B.* **56**, 9496-9505 (1997).

20. T. Ogino and M. Aoki, "Mechanism of yellow luminescence in GaN." *Jpn. J. Appl. Phys.* **19**, 2395-2405 (1980).

21. R. Zhang and T.F. Kuech, “Carbon and hydrogen induced yellow luminescence in gallium nitride grown by halide vapor phase epitaxy.” *Mat. Res. Soc. Symp. Proc.* **482**, 709-714 (1998).

22. C.-Y. Hwang, M.J. Schurman, W. E. Mayo, Y.-C. Lu, R.A. Stall and T. Salagajj, “Effect of structural defects and chemical impurities on Hall mobilities in low pressure MOCVD grown GaN.” *J. Electron. Mater.* **26**, 243-251 (1997)

23. J.Z. Li, J.Y. Lin, H.X. Jiang, M. Asif Khan and Q. Chen, “Persistent photoconductivity in a tow-dimensional electron gas system formed by an AlGaN/GaN heterostructure.” *J. Appl. Phys.* **82,** 1227-1230 (1997).

24. F. Binet, J.Y. Duboz, E. Rosencher, F. Scholz and V. Härle, “Mechanisms of recombination in GaN photodetectors.” *Appl. Phys. Lett.* **69**, 1202-1204 (1996).

25. H. Amano, M. Kito, K. Hiramatsu, and I. Alasaki, “P-type conduction in Mg-doped GaN treated with low-energy electron beam irradiation (LEEBI).” *Jpn. J. Appl. Phys., Part 2.* **28**, L2112-L2214 (1989).

26. J.I. Pankove, “GaN and Related Materials” edited by S. J. Pearton (Gordon and Breach, New York, 1997) pp.1-9.

27. C.G. Van de Walle, “Defects, doping and interfaces in III-V nitrides.” SPIE. **3283,** 52-59 (1998).

28. S. Nakamura, N. Iwasa, M. Senoh, and T. Mukai, “Hole compensation mechanism of p-type GaN films.” *Jpn. J. Appl. Phys., Part 1* **31,** 1258-1266 (1992).

29. P. Kozodoy, “Magnesium-doped gallium nitride for electronic and optoelectronic device applications.” *PhD Thesis*, Electrical and Computer Engineering, University of California, Santa Barbara (1999).

30. D. Walker X. Zhang, P. Kung, A. Saxler, S. Javadpour, J. Xu,. And M. Razeghi, “AlGaN ultraviolet photoconductors grown on sapphire.” *Appl. Phys. Lett.* **68**, 2100-2101 (1996).

31. B.W. Lim, Q.C. Chen, J.Y. Yang, and M. Asif Khan, “High responsivity intrinsic photoconductors based on $Al_xGa_{1-x}N$.” *Appl. Phys. Lett.* **68**, 3761-3762 (1996).

32. Y.-F. Wu, B.P. Keller, P. Fini, S. Keller, T.J. Jenkins, L.T. Kehias, S.P. DenBaars, and U.K. Mishra, “High Al-content AlGaN/GaN MODFET’s for ultrahigh performance.” *IEEE Electron Lett.* **19**, 50-53 (1998).

33. M. Asif Khan, J.N. Kuznia, J.N. Van Hove, N. Pan, and J. Carter, “Observations of a two-dimensional electron gas in a low pressure metalorganic chemical vapor deposited GaN-$Al_xGa_{1-x}N$ heterojunctions.” *Appl. Phys. Lett.* **60**, 3027-3029 (1992).

34. M.A. Khan, J.N. Kuznia, D.T. Olson, W.J. Schaff, J.W. Burm, and M.S. Shur, “Microwave performance of a 0.2μm gate AlGaN/GaN heterostructure field effect transistor.” *Appl. Phys. Lett.* **65**, 1121-1123 (1994).

35. J.P. Ibbetson, P.T. Fini, K.D. Ness, S.P. DenBaars, U.K. Mishra, and J.S. Speck, “Polarization effects, surface states, and the source of electrons in AlGaN/GaN heterostructure field effect transistors.” *Appl. Phys. Lett.* **77**, 250-252 (2000).

36. F. Bernardini, V. Fiorentini, and D. Vanderbilt, “Spontaneous polarization and piezoelectric constants of III-V nitrides.” *Phys. Rev. B* **56,** R10024-10027 (1997).

37. Y.-F. Wu, S. Keller, P. Kozodoy, B.P. Keller, P. Parikh, D. Kapolnek, S.P. DenBaars, and U.K. Mishra, “Bias dependent microwave performance of AlGaN/GaN MODFET’s up to 100 V.” *IEEE Electron Device Lett.***18**, 290-292 (1997).

38. Y.-F. Wu, B.P. Keller, S. Keller, N.X. Nguyen, M. Le, C. Nguyen, T.J. Jenkins, L.T. Kehias, S.P. DenBaars, and U.K. Mishra, “Short channel AlGaN/GaN MODFET’s with 50GHz f_t and 1.7 W/mm output power at 10 GHz.” *IEEE Electron Device lett.* **18**, 438-440 (1997).

39. B.J. Thibeault, B.P. Keller, Y.-F. Wu, P. Fini, U.K. Mishra, C. Nguyen, N.X. Nguyen, and M. Le, “High performance and large area flip-chip bonded AlGaN/GaN MODFET’s.” *56th Annual Device Research Conference,* Charlottesville, VA June 1998.

40. Y.-F.Wu, B.J.Thibeault, J.J. Xu, R.A. York, S. Keller, B.P. Keller, and U.K. Mishra, "GaN HEMTs grown on sapphire substrates for microwave power amplification." *57th IEEE Device Research Conference,* Santa Barbara, CA June 1999.

41. G. Parish, S. Keller, P. T. Fini, R. Vetury, C.-H. Chen, S. P. DenBaars, U. K. Mishra and Y.-F. Wu, "MOCVD growth and properties of thin AlxGa1-xN layers on GaN." *Proc. IEEE* COMMAD Perth, Australia, 478-481 (1998).

42. S, Keller, G. Parish, P. T. Fini, S. Heikman, C.-H. Chen, N. Zhang, S. P. DenBaars and U. K. Mishra, "Metalorganic chemical vapor deposition of high mobility AlGaN/GaN heterostructures." *J. Appl. Phys.* **86**(10), 5850-5857 (1999).

43. "Nitres develops AlGaN/GaN HEMTs with record power performance." *Compound Semiconductor* **6** (1), (2000).

44. M. Razeghi and A. Rogalski, "Semiconductor ultraviolet detectors." *J. Appl. Phys.* **79**, 7433-7473 (1996).

45. J.D. Brown, Zhonghai Yu, J. Mathews, S. Harney, J. Boney, J.F. Schetzina, J.D. Benson, K.W. Dang, C. Terrill, T. Nohava, W. Yang, and S. Krishnankutty, "Visible-blind UV digital camera based on 32x32 array of GaN/AlGaN p-i-n photodiodes." *MRS Internet J. Nitride Semicond. Res* **4**, 9 (1999).

46. Figure provided by B.D. Nener (private communication), The University of Western Australia (2001).

47. M. Razeghi and A. Rogalski, "AlGaN ultraviolet detectors." *Proc. SPIE* **2999**, 275-286 (1997).

48. P. Schreiber, T. Dang, G. Smith, T. Pickenpaugh, P. Gerhed, D. Littleton, "Solar blind UV region and UV detector development objectives." *Proc. SPIE* **3629**, 230-248 (1999).

49. M. Asif Khan, J.N. Kuznia, D.T. Olson, J.M. Van Hove, M. Blasingame, and L.F. Reitz, "High-responsivity photoconductive ultraviolet sensors based on insulating single-crystal GaN epilayers." *Appl.Phys. Lett.* **60** (23), 2917-2919 (1992).

50. M. Asif Khan, J.N. Kuznia, D.T. Olson, M. Blasingame, and A.R Bhattarai, "Schottky barrier photodetector based on Mg-doped *p*-type GaN films." *Appl. Phys. Lett.* **63** (18), 2455-2456 (1993).

51. Q. Chen, M. Asif Khan, C.J. Sun, and J.W. Yang, "Visible-blind ultraviolet photodetectors based on GaN *p-n* junctions." *Electronics Letters* **31** (20), 1781-1782 (1995).

52. X. Zhang, P. Kung, D. Walker, J. Piotrowski, A. Rogalski, A. Saxler, and M. Razeghi, "Photovoltaic effects in GaN structures with *p-n* junctions." *Appl. Phys. Lett.* **67,** 2028-2030 (1995).

53. V. Adivarahan, G. Simin, J.W. Yang, A. Lunev, M. Asif Khan, N.Pala, M. Shur, and R. Gaska, "SiO_2-passivated lateral-geometry GaN transparent Schottky-barrier detectors." *Appl. Phys. Lett.* **77**, 863-865 (2000).

54. E. Monroy, F. Calle, E. Muñoz, B. Beaumont, F. Omnès, and P. Gibart, "High UV/visible contrast photodiodes based on epitaxial lateral overgrown GaN layers." *Electronics Letters* **35,** 1488-1489 (1999).

55. A. Osinsky, S. Gangopadhyay, R. Gaska, B. Williams, M.A. Khan, D Kuksenkov, and H. Temkin, "Low noise p-π-n GaN ultraviolet photodetectors." *Appl. Phys. Lett.* **71,** 2334-2336 (1997).

56. J.C. Carrano, T. Li, P.A. Grudowski, C.J. Eiting, D. Lambert, J.D. Schaub, R.D. Dupuis, and J.C. Campbell, "Low dark current *pin* ultraviolet photodetectors fabricated on GaN grown by metal organic chemical vapor deposition." *Electronics Letters* **34**, 692-694 (1998).

57. W. Yang, T. Nohova, S. Krishnankutty, R. Torreano, S.t McPherson, and H. Marsh, "Back-illuminated GaN/AlGaN heterojunction photodiodes with high quantum efficiency and low noise." *Appl. Phys. Lett.* **73**, 1086-1088 (1998).

58. G. Smith, M.J. Estes, T. Dang, A.A. Salvador, Z. Fan, G. Xu, A. Botchkarev, H. Morkoc, and P. Wolf, "Megahertz bandwidth $Al_xGa_{1-x}N$/GaN-based pin detectors." *Proc. SPIE* **3287,** 198-205 (1998).

59. T. Li, A.L. Beck, C. Collins, R.D. Dupuis, J.C. Campbell, J.C. Carrano, M.J. Schurman, and I.A. Ferguson, "Improved ultraviolet quantum efficiency using a semitransparent recessed window AlGaN/GaN heterojunction *p-i-n* photodiode." *Appl. Phys. Lett*. **75**, 2421-2423 (1999).

60. J.D. Brown, Zhonghai Yu, J. Mathews, S. Harney, J. Boney, J.F. Schetzina, J.D. Benson, K.W. Dang, C. Terrill, T. Nohava, W. Yang, and S. Krishnankutty, "Visible-blind UV digital camera based on 32x32 array of GaN/AlGaN p-i-n photodiodes." *MRS Internet J. Nitride Semicond. Res.* **4**, 9 (1999).

61. A. Osinsky, S. Gangopadhyay, B.W. Lim, M.Z. Anwar, M.A. Khan, D.V. Kuksenkov, and H. Temkin, "Schottky barrier photodetectors based on AlGaN." *Appl. Phys. Lett.* **72**, 742-744 (1998).

62. G. Parish, S. Keller, P. Kozodoy, J. P. Ibbetson, H. Marchand, P. T. Fini, S.B. Fleischer, S. P. DenBaars, U. K. Mishra and E.J. Tarsa, "High-performance (Al,Ga)N-based solar-blind ultraviolet p-i-n detectors on laterally epitaxially overgrown GaN." *Appl. Phys. Lett.* **75**(2), 247-249 (1999).

63. U. Karrer, A. Dobner, O. Ambacher, and M. Stutzmann, "AlGaN-based ultraviolet light detectors with integrated optical filters." *J. Vac. Sci. Technol.B* **18,** 757-760 (2000).

64. D.H. Lambert, M.M. Wong, U. Chowdhury, C. Collins, T. Li, K. Kwon, B.S. Shelton, T.G. Zhu, J.C. Campbell, and R.D. Dupuis, "Back illuminated AlGaN solar-blind photodetectors." *Appl. Phys. Lett.* **77,** 1090-1092 (2000)

65. C. Pernot, A. Hirano, M. Iwaya, T. Detchprohm, H. Amano, and I. Akasaki, "Solar-blind UV photodetectors based on GaN/AlGaN p-i-n photodiodes." *Jpn. J. Appl. Phys.* **39,** 387-389 (2000).

66. D. Walker, V. Kumar, K. Mi, P. Sandvik, P. Kung, and M. Razeghi, "Solar-blind AlGaN photodiodes with very low cutoff wavelength." *Appl. Phys. Lett.* **76,** 403-405 (2000).

Chapter 2. AlGaN growth using sapphire substrate

2.1 Introduction

As described in the introductory chapter, the focus of this work is on the development of $Al_xGa_{1-x}N$ for solar-blind photodetectors, and thus of $Al_xGa_{1-x}N$ with greater than 30% aluminum content. Literature detailing growth investigations of such high-composition AlGaN has been minimal, although in recent years it has been receiving more attention. In general, however, when reviewing both the literature and the results presented in this chapter, it becomes apparent that alloying GaN with significant quantities of Al presents more challenges to growth than with GaN alone.

2.1.1 Epitaxially grown bulk AlGaN

At the onset of this study, it was evident from the literature that bulk AlGaN of a high structural and electrical quality is very difficult to grow[1,2,3,4,5]. It is hard to achieve atomically smooth, step-flow growth of compositionally uniform, defect-free, and, depending on the substrate, crack-free AlGaN of high composition. Recent results of $Al_{0.5}Ga_{0.5}N$ deposited on bulk AlN substrates[6] are at a very early stage of development, although use of this substrate is expected to eventually show improvement. Most bulk AlGaN reported has, as with GaN, been deposited on sapphire substrates. Again, similarly to GaN, the use of a low temperature nucleation layer was shown to help.[7] Many recent reports reveal little progress in overcoming the difficulties in AlGaN growth[8,9,10]. One notable exception has been the work of Iwaya et al.[11]. This group has achieved pronounced improvements in quality of thick

(>1μm) $Al_xGa_{1-x}N$ layers deposited on a low-temperature AlN interlayer on GaN templates on sapphire (with an AlN nucleation layer), with no degradation in properties as x_{Al} is raised. Also, recently reported UV detectors fabricated from bulk AlGaN grown on sapphire substrate with a thick higher-x_{Al} AlGaN buffer have indicated AlGaN of relatively high quality[12,13].

Compounding the difficulties in obtaining device-quality AlGaN is the difficulty in doping. Many of the studies referenced above reported a monotonic increase in resistivity (with a decrease in both carrier concentration and mobility) of undoped AlGaN with increasing Al content (at low compositions, undoped AlGaN is usually n-type). Even when doped intentionally n-type with silicon or germanium, electrically conducting material has not been obtained for x_{Al} greater than 0.5[1,3]. Although there has been much theoretical and experimental research into the insulating nature of AlGaN and AlGaN:Si, controversy about its cause still exists. There is general agreement that oxygen, a shallow donor in GaN, and ever-present in MOCVD-grown AlGaN, becomes a DX center in $Al_xGa_{1-x}N$ above x_{Al}=0.3[14]. More questionable is whether in addition to an increase in ionization energy as the bandgap widens, Si becomes a DX center, or whether some other defect such as Al vacancies cause compensation[15,16]. Furthermore, p-type doping has not been reported for $Al_xGa_{1-x}N$ at the compositions of interest in this study. However even for lower compositions of x_{Al} = 0.1-0.2, research again shows that p drops significantly as x_{Al} is increased[17,3]. As in the case of silicon doping, this is due at least in part to the increase in activation energy of Mg as x_{Al}, and hence E_G, increases[15].

2.1.2 AlGaN/GaN heterostructures

The growth of AlGaN/GaN heterostructures is also difficult, exacerbated by the lattice and thermal mismatch between the AlGaN and the underlying GaN (a_{GaN} = 3.189Å, a_{AlN} = 3.112Å at 300K; $\alpha_{GaN} = 5x10^{-6}K^{-1}$, $\alpha_{AlN} = 5.3x10^{-6}K^{-1}$ at 600K[18]). To avoid cracking, the AlGaN layers must be thin, so that an assessment of bulk AlGaN properties cannot be obtained with such structures. Nevertheless, Hall measurements of the 2DEG formed at the AlGaN/GaN interface allow some assessments with regard to AlGaN quality. This is especially advantageous when considering that for bulk AlGaN the difficulty in obtaining low-resistance material precludes effective electrical measurements. Hall studies of the 2DEG, including temperature-dependent measurements, can indicate the effects of alloy clustering, interface roughness, dislocations and point defects. Furthermore, epitaxial growth of thin layers on a standard GaN template allows the surface morphology to be assessed with respect to growth conditions without the need to develop unique nucleation schemes for each AlGaN composition. Very little had been published regarding AlGaN/GaN heterostructures when we began our studies. Some of the results which we previously published, and are presented here, have been confirmed by others such as Eiting et al.[19]

2.1.3 Synopsis of the chapter

This chapter will detail the development of MOCVD growth of $Al_xGa_{1-x}N$ using sapphire substrates, with x_{Al} ranging from 0.2 to 0.65. In Section 2.1 the principles for MOCVD growth at UCSB are outlined, and some initial studies into bulk AlGaN growth are presented. This is followed in Section 2.2 by the investigations into the effect of growth conditions and x_{Al} on AlGaN morphology and 2DEG properties, which utilized thin AlGaN layers deposited on GaN base layers. Finally in Section 2.4 impurity incorporation as a function of x_{Al} and growth conditions will be discussed.

2.2 MOCVD Growth at UCSB

The material for the growth studies presented in this chapter was grown by MOCVD in a two-flow horizontal quartz reactor, using the precursors trimethylgallium (TMGa), trimethylaluminum (TMAl) and ammonia. Disilane (DiSi) was used for n-type doping with Si. For the AlGaN/GaN heterostructures the growth of the GaN base layers was initiated on the sapphire substrate with an approximately 20 nm thick GaN layer grown at 525 °C while the main GaN layer was grown at temperatures between 1040 and 1125 °C[20]. A wide parameter space was explored for the growth of the AlGaN layers: The TMGa flow and the TMAl flow were varied between 0.6 – 77 μmol/min and the ammonia flow between 0.03 – 0.32 mol/min. Variations in growth rate were achieved by changing the group III flows. The growth temperature ranged from 800 to 1125 °C. The growth temperature was measured by means of a thermocouple inserted into the graphite susceptor, protected by a quartz sheath. The total gas flow was kept constant at 11 l/min. The reactor pressure for GaN and AlGaN growth was 760 and 76 torr, respectively, except for the impurity incorporation experiments, when 300 torr was also used.

High-resolution x-ray diffraction with a Phillips Materials Research Diffractometer was used for composition determination. To obtain Si doping incorporation and impurity concentrations, SIMS analysis was performed, by Evans East.

2.2.1 Al incorporation

A prominent issue, which complicates AlGaN growth by MOCVD, is the occurrence of pre-reactions between the precursors when TMAl and NH_3 are used[21,22,23,24]. There have been many reports of the effect of these pre-reactions on the incorporation of Al into the AlGaN[22]. The solid phase composition is always less than the gas phase composition of reactants, and in some cases incorporation of Ga is also inhibited by the presence of TMAl. In general reducing the growth pressure can minimize the effect, but this then limits the parameter space available for optimization of the AlGaN growth. In the reactor used for these experiments, the group III and group V precursors were separated prior to the hot-zone. Even so, a low growth pressure of below 150 torr was necessary to avoid significant pre-reactions.

Even at low pressures, the incorporation efficiency was strongly dependent on growth conditions, namely the growth temperature and the growth rate. Figure 2.1 shows that for a constant ratio of TMAl/TMGa=0.5 the aluminum mole fraction in the solid, x^s_{Al} , rises with increasing growth temperature (Figure 2.1a) and drops with increasing growth rate (Figure 2.1b). These trends were reproducible over many experiments. An increase of the growth temperature (T_{gr}) from 1070 to 1125 °C caused the aluminum mole fraction in the $Al_xGa_{1-x}N$ layers to rise from x_{Al} = 0.37 to x_{Al} = 0.42, at a constant TMGa and TMAl input flow of f_{TMAl}+f_{TMGa} = 38 μmol/min. The aluminum mole fraction increased from x_{Al} = 0.36 to x_{Al} = 0.52 when the TMGa and TMAl input flows were decreased from 76 to 19 μmol/min at Tgr = 1125 °C. These two trends are consistent with the lowering of the GaN growth rate with respect to the AlN growth rate in both situations. This was revealed by investigations both of the AlGaN thickness and of the growth of GaN itself.

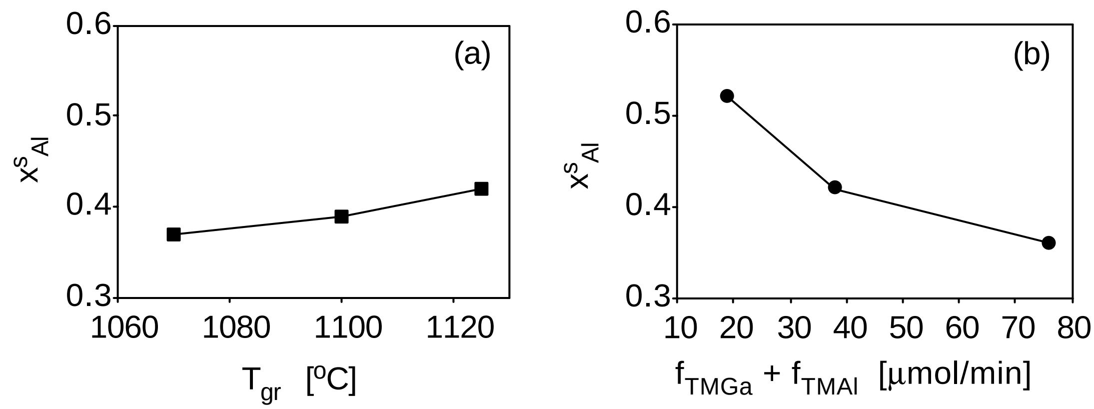

Figure 2.1 Dependence of the aluminum mole fraction x_{Al} in the $Al_xGa_{1-x}N$ layers on a) the growth temperature for $f_{TMAl} + f_{TMGa}$ = 38 μmol/min and b) the TMAl and TMGa input flow at a T_{gr} = 1125 °C. The TMAl/TMGa ratio was 0.5. These trends were reproducible over many experiments.

Separate investigations into the growth rate of GaN revealed that even with the product of flow and growth time kept constant, the GaN thickness was changing with TMGa flow. Figure 2.2 shows the dependence of the growth rate (r) of GaN grown at 1070°C on the TMGa flow.

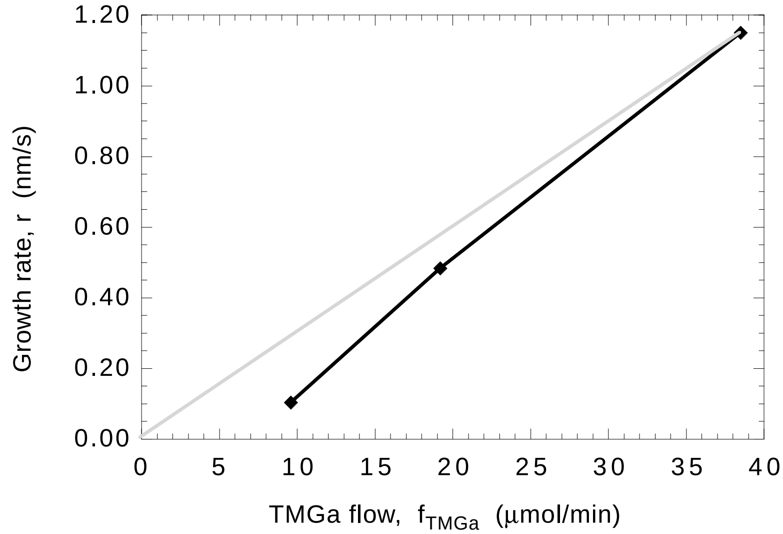

Figure 2.2 Growth rate as a function of TMGa flow for GaN grown at 1070°C, 760 torr and NH_3 flow of 0.27 mol/min. Experimental results are shown in black. The grey dotted line assumes ideal (linear) behavior for the highest input flow.

The grey dotted line assumes ideal (linear) behavior for the highest input flow. It is evident that there is a non-linear dependence; with the growth rate slowing at lower flows. Even at a relatively high growth rate of 0.48 nm/s (1.74 µm/hr) this non-linearity already exists. A linear dependence is expected only when the input partial pressure of Ga-species, p_{Ga}^{o}, is much higher than the equilibrium partial pressure of the gallium, p_{Ga}^{eq}, so that p_{Ga}^{eq} can be neglected.

If p_{Ga}^{eq} can be neglected then

$$r \propto \left(p_{Ga}^{o} - p_{Ga}^{eq}\right) \tag{2.1}$$

may be simplified to

$$r \propto p_{Ga}^{o} \tag{2.2}$$

where p_{Ga}^{o} is proportional to the TMGa input flow.[25'26] At low input flows and high temperatures (and therefore high p_{Ga}^{eq}) this simplification is not valid and this results in the non-linear dependence seen in Figure 2.2. In addition to this, higher growth temperatures will lower the sticking probability of Ga-species on the epitaxial surface.

On the other hand, p_{Al}^{eq} is always much smaller than p_{Al}^{o} under the experimental conditions in this study and can be neglected. Hence, with increasing T_{gr} and decreasing p_{Ga}^{o} , the composition of the AlGaN is given by

$$x_{Al}^{s} = \frac{k_{Al}\left(p_{Al}^{o}\right)}{k_{Al}\left(p_{Al}^{o}\right) + k_{Ga}\left(p_{Ga}^{o} - p_{Ga}^{eq}\right)} \ . \tag{2.3}$$

In the above equation k_{Al} and k_{Ga} are the transport coefficients, which represent the incorporation efficiency for the entire growth process (including pre-reactions, gas-phase transport, surface kinetics and so on).

2.2.2 Bulk AlGaN growth on sapphire

Initial, limited studies into the bulk growth of AlGaN on sapphire substrates were carried out at UCSB. Different nucleation and growth conditions were attempted, without success in simultaneously achieving smooth, specular and crack-free layers. The first attempts utilized the same nucleation scheme as was used for GaN templates. After deposition of a 200Å low-temperature GaN nucleation layer, thin high temperature layers of 500-2000Å GaN were grown, followed by 1-1.5μm bulk $Al_{0.3}Ga_{0.7}N$ layers. The AlGaN layers were grown at 1080°C, a slightly higher temperature than for GaN layers, with growth conditions otherwise comparable to GaN template growth. These films were not specular, and exhibited (0002) rocking-curve full-width half-maximum (FWHM) values of 1200-1600 arc-seconds. Similar AlGaN films were deposited on thin AlN layers obtained by high-temperature exposure of the sapphire (Al_2O_3) to NH_3. Again the films were not specular, with large hexagonal surface features visible by optical microscopy, although the FWHM values were reduced to 600-700 arc-seconds. Finally, the bulk layers were again initiated with deposition of a 200Å low-temperature GaN nucleation layer, this time followed by thin higher-temperature layers of 300-700Å GaN grown at 76 torr (the lower pressure induces faster coalescence of the nucleation islands due to increased lateral overgrowth), and 1μm bulk $Al_{0.3}Ga_{0.7}N$ layers. In this case the AlGaN layers were growth under low-ammonia conditions, as this had been found to improve the surface morphology of thin AlGaN layers on GaN (see next section for discussion of these studies). The films obtained this way were in fact specular, but optical microscopy revealed a highly granular surface, and many cracks. Again, the (0002) rocking curve FHWM was very high, ranging from 1000-1200 arc-seconds.

2.2.3 AlGaN/GaN heterostructures

As explained in the introduction to this chapter, the bulk of the investigations into the effect of growth conditions and x_{Al} on morphology and 2DEG properties utilized AlGaN/GaN heterostructures. Thin $Al_xGa_{1-x}N$ layers of 2 – 30 nm were grown on 3 μm thick semi-insulating GaN on c-plane sapphire substrates. A cross-section of these structures is given in Figure 2.3. The properties of the 2DEG forming at the heterojunction were studied using modulation doped $Al_xGa_{1-x}N$/GaN structures. Unless otherwise stated, the AlGaN layer was divided into a 2.5 nm thick undoped spacer layer, a 10 nm thick silicon doped layer ($[Si]_{SIMS}$ = 1 x 10^{19} cm^{-3}) and an undoped cap layer of a thickness of 5 nm for $x_{Al} \leq 0.35$ and a thickness of 2 nm for $x_{Al} \geq 0.4$. The electrical properties of the 2DEG formed at the AlGaN/GaN interface were evaluated by Van der Pauw Hall measurements.

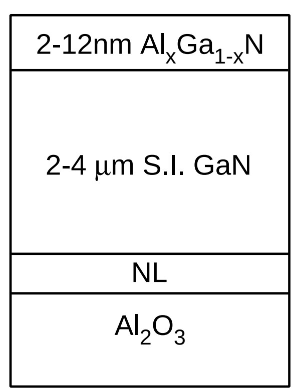

Figure 2.3. Experimental $Al_xGa_{1-x}N$/GaN layer structures.

2.2.4 LEO growth technique

As was discussed in Chapter 1, the use of LEO techniques has been shown to significantly reduce the high dislocation densities usually present in GaN and its alloys. As part of the investigations into surface morphology and defect structure of the AlGaN, a thin AlGaN layer was also deposited onto an LEO GaN template, using the process developed at UCSB[27]. Atomic force microscopy (AFM) and transmission electron microscopy (TEM) studies have shown that in the laterally overgrown regions the defect densities are less than 10^6 cm^{-2}. Figure 2.4 gives a schematic of the LEO growth process.

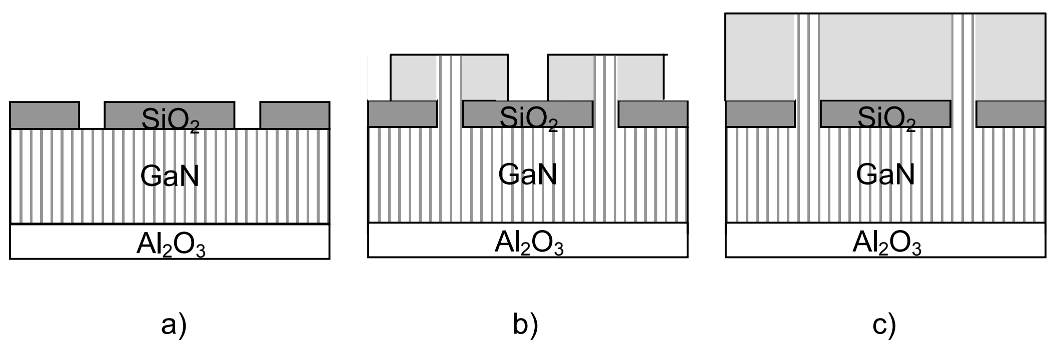

Figure 2.4. Schematic of LEO GaN growth.

a) SiO_2 pattern on GaN template. Exposed areas of dislocated GaN (seed) are 5µm wide with 40µm periodicity. b) Lateral growth occurs from GaN seed areas. Vertical lines indicate threading dislocations. These propagate vertically, but not laterally, into the overgrowth wings. c) Further lateral growth results in coalescence of wings, then vertical growth continues.

For the LEO GaN template, a 2μm thick GaN wafer was patterned with SiO_2 stripes. These stripes were 35 μm wide, with a periodicity of 40 μm. This left 5μm stripes of the underlying GaN (seed region) exposed. Subsequent regrowth on this wafer resulted in selective epitaxial growth of GaN wings laterally across the SiO_2 mask.

2.3 Surface morphology of AlGaN/GaN heterostructures

The surface morphology of the layers was studied by atomic force microscopy (AFM) using a Digital Instruments Nanoscope III, operated in tapping mode. The root-mean-square (RMS) roughness of the surfaces was calculated using the AFM software.

2.3.1 Effect of x_{Al}

AFM imaging of the thin AlGaN layers revealed a very strong dependence of the surface morphology on the composition. Figure 2.5 presents the AFM images of the surfaces of 18 nm thick $Al_xGa_{1-x}N$ films, with x_{Al} values of (a) 0.2, (b) 0.4 and (c) 0.6, along with (d) the surface of a typical GaN base film. The surface of the $Al_{0.2}Ga_{0.8}N$ film (Figure 2.5a) resembles the surface of the GaN base film (Figure 2.5d). The surface is characterized by a step-like structure. Each step corresponds to an (Al,Ga)-N bi-layer. The steps merge at threading dislocations with a screw component, which are seen as dark spots in the image. The smaller dark spots, which are independent of the step structure, originate from edge dislocations[28].

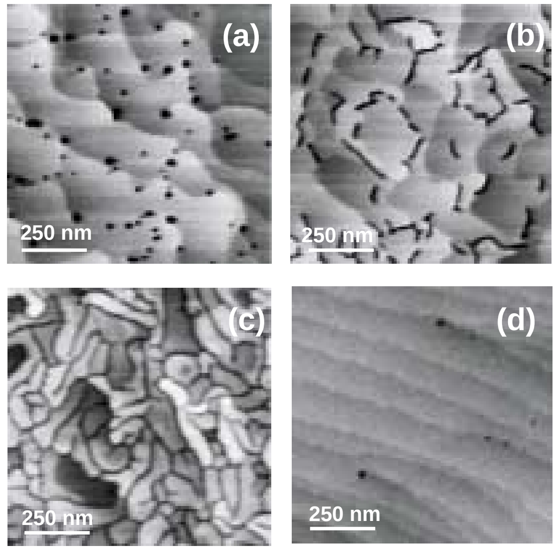

Figure 2.5 AFM images of 20nm thick $Al_xGa_{1-x}N$ showing change in morphology with x_{Al}. a) x_{Al} = 0.2, b) x_{Al} = 0.4, c) x_{Al} = 0.6, d) typical GaN base layer. The greyscale is 3 nm.

At higher Al mole fractions, dark lines are observed, representing structural defects. These appear to form connections between individual dislocations from the underlying film. Interrupted growth studies revealed that these defects were not formed at the interface but developed as the layer became thicker. A 2nm thick layer of x_{Al} = 0.6 thus looked very similar to Figure 2.5a. The density of these defects increases with increasing x_{Al}, comparable to a transition into an island growth mode. Initial TEM investigations have suggested that the observed defects are caused by stacking faults. The tendency of increased defect formation with increasing Al content and increasing strain in the AlGaN layer is thus made evident

2.3.2 Effect of growth conditions

Figure 2.6 illustrates the effect of the NH_3 flow on the surface morphology of 20 nm thick $Al_{0.35}Ga_{0.65}N$ layers. The structural defect density is seen here to increase with increasing NH_3 flow (V/III ratio). At the highest NH_3 flow of 6 l/min, the growth switched completely into an island growth mode. Obviously, the tendency for structural defect formation in the AlGaN layer is not only related to strain in the AlGaN, but also to the growth kinetics. In this case the formation of defects is suppressed by decreasing the concentration of adsorbed N-species on the surface, by lowering NH_3 flows. The decreased concentration of N-species increases the surface mobility of adsorbed Ga- and Al-species. The higher the Al mole fraction in the film, the more pronounced this effect, due to the higher bond strength of Al-N (2.88eV) compared to Ga-N (1.93eV) [29].

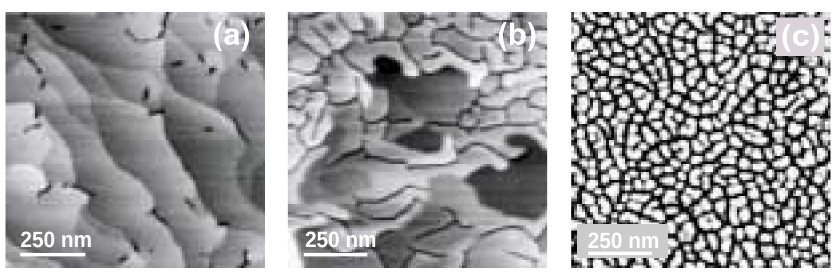

Figure 2.6 AFM images of 20nm thick $Al_{0.35}Ga_{0.65}N$ showing effect of f_{NH3} on morphology. a) f_{NH3}=1.5 l/min, b) f_{NH3}=3 l/min, c) f_{NH3}=6 l/min. The greyscale is 3 nm.

In contrast to the strong effect of the ammonia flow, no significant effect of growth temperature on surface morphology was observed for temperatures between 800 and 1125°C. By optimization of the growth rate at each temperature (using lower growth rates at lower temperatures to compensate for the lower adatom mobility), a comparable surface could be obtained for the same composition. This is demonstrated in Figure 2.7, which shows a 20 nm thick film of $Al_{0.3}Ga_{0.7}N$ grown at 800°C, which is very similar-looking to the morphology in Figure 2.6a. At these temperatures, the growth rate was an order of magnitude lower than for high temperatures ($T \geq 1060$°C), for which a growth rate on the order of 1-6 Å/s was appropriate.

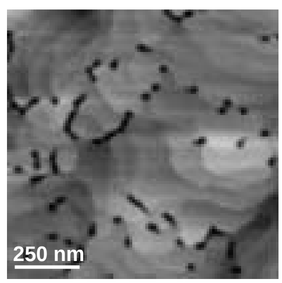

Figure 2.7 AFM image of 20nm thick $Al_{0.3}Ga_{0.6}N$ grown at 800°C. The greyscale is 3nm.

2.3.3 Effect of underlying GaN template

Recalling Figure 2.5b in particular, it was evident from the previous AFM images at various stages of defect formation that the initiation of the defects occurred primarily at the threading dislocations. This role of dislocations in facilitating defect formation appears to be confirmed when examining AlGaN layers deposited on LEO GaN.

Figure 2.8 is an AFM image of a 20nm $Al_{0.3}Ga_{0.7}N$ layer grown on an LEO GaN template. A much higher number of structural defects are visible in the dislocated seed region.

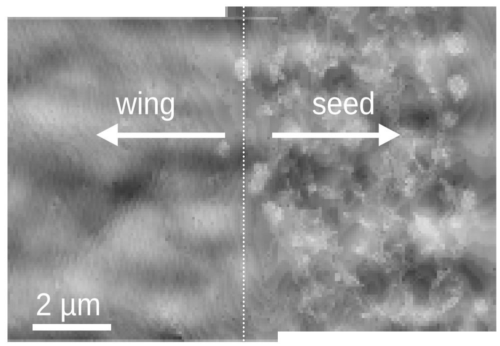

Figure 2.8. AFM image across seed and wing regions of $Al_{.3}Ga_{.7}N$/GaN heterostructure, showing change in dislocation structure and morphology on LEO GaN wings.

2.4. Electrical properties of AlGaN/GaN heterostructures

Standard Hall measurements using a Van der Pauw pattern were taken at 300K and at 77K for the AlGaN/GaN heterostructures. This allowed assessment of the effect of different AlGaN growth conditions and compositions on the sheet charge and mobility of the 2DEG. To ensure optimal quality for device applications all of the AlGaN films under discussion in this section were grown with a low NH_3 flow of 1.5l/min. For some structures temperature-dependent Hall was also measured between 77 and 300K.

2.4.1 Effect of x_{Al}

The effect of x_{Al} on the carrier properties of the 2DEG is immediately apparent when examining Figure 2.9. As the composition is increased from 0.25 to 0.45 the mobility rapidly drops from 1400 to 1050 cm^2/Vs, while the sheet charge increases from $1x10^{13}$ to $1.7x10^{13}$ cm^{-2}. Due to the increased strain, conduction band discontinuity, and piezoelectric field obtained with higher x_{Al}, a higher sheet charge is created which is increasingly tightly confined[30]. Thus for a non-zero surface roughness the increase in surface charge alone could account for the reduced mobility at higher x_{Al}.

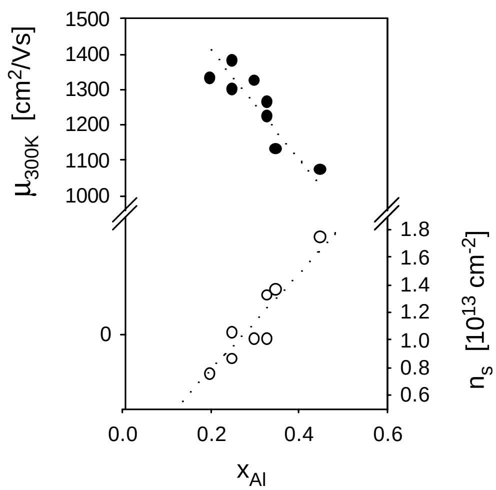

Figure 2.9 Dependence of the electron mobility (filled circles) and the sheet carrier density (open circles) measured at 300 K on the aluminum mole fraction in the $Al_xGa_{1-x}N$ layer.

In Figure 2.10 it can be seen that at low measurement temperatures the electron mobility declined even faster with increasing x_{Al} (T = 15 K, x_{Al} =0.34: μ_{2DEG} = 4400 cm^2/Vs, x_{Al} =0.36: μ_{2DEG} = 2800 cm^2/Vs). At low temperatures phonon scattering mechanisms, which are superimposed on the behavior at room temperature, are less efficient[31]. In addition to the impact of the surface roughness, as x_{Al} increases more difficulties are presented in the growth of a laterally smooth and vertically abrupt heterojunction, as seen from the surface morphology investigations. The expansion of structural defects in the near surface region of the Al_xGa_{1-x} N layer as shown in Figure2.5c may result in local variations in the strain field, which also contribute to the decrease of μ_{2DEG}. Furthermore, the generally low mobility and lack of enhancement at low temperatures for the sample with x_{Al} = 0.65 is not typical of 2DEG behavior. Insensitivity of sheet carrier concentration to measurement temperature (not shown) for this and the other two samples does, however, affirm the presence of a 2DEG. The results for x_{Al} = 0.65 therefore indicate the presence of a significant number of band-tail states[30], possibly due to alloy clustering in addition to the surface roughness. Several other groups have measured strong alloy disorder in AlGaN in the past[32,33,34,10].

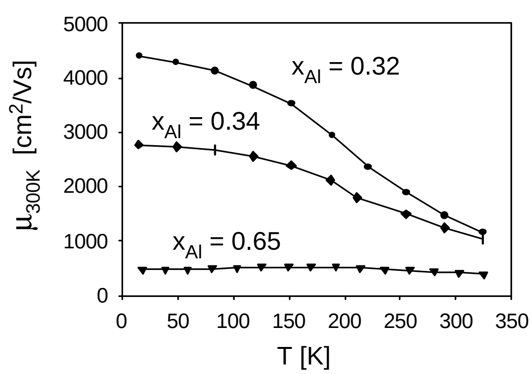

Figure 2.10 Temperature dependence of the electron Hall mobility for samples with different aluminum mole fraction x_{Al} in the $Al_xGa_{1-x}N$ layer.

2.4.2 Effect of growth conditions

The lack of effect of growth temperature on surface morphology seen previously is reiterated when inspecting Figure 2.11. Here μ_{2DEG} and n_s measured at 77K are plotted as a function of growth temperature. No significant dependence is seen. This was also true for variations in growth rate (not shown).

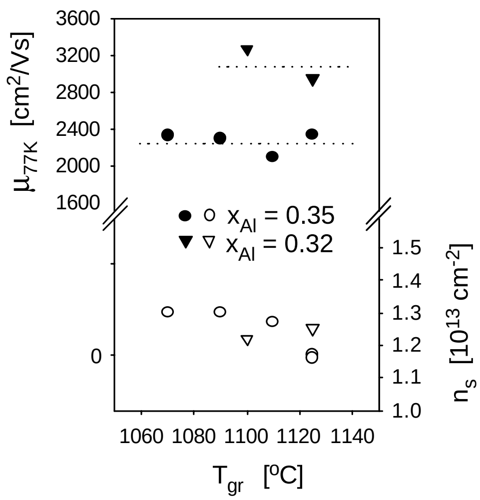

Figure 2.11 Dependence of the electron mobility (filled symbols) and the sheet carrier density (open symbols) measured at 77 K on the growth temperature of the $Al_xGa_{1-x}N$ for x_{Al} = 0.35 (circles) and x_{Al} = 0.32 (triangles).

2.5 Impurity incorporation during $Al_xGa_{1-x}N$ growth

In this work, carbon and oxygen impurity levels, as well as silicon doping, in MOCVD-grown GaN and AlGaN, were investigated as a function of growth conditions and Al content. Multi-layer (Al)GaN structures were deposited by MOCVD on sapphire substrates. Each structure consisted of sequences of GaN and/or AlGaN layers grown with a specific growth parameter varied in each layer. To assist in identification of the various layers in the SIMS analysis, layers were alternately unintentionally doped or doped with silicon. Each structure was capped with a thick (1000Å-5000Å) GaN layer to avoid surface artifacts in the layer analysis. For the AlGaN layers composition was varied from x_{Al} = 0.04 to x_{Al} = 0.50. The growth parameters that were investigated were growth temperature, growth rate, silicon doping, carrier gas and V/III ratio.

SIMS analysis was performed at Evans East used cesium ion bombardment to obtain concentration depth profiles. Quantification of the profiles was accomplished by analyzing ion implanted GaN standards. Detection limits due to background in GaN for each species were nominally: oxygen, $6x10^{16}$ cm^{-3}; carbon, $6x10^{16}$ cm^{-3}; and silicon, $1x10^{16}$ cm^{-3}. The detection limits in AlGaN were nominally: oxygen, $2x10^{17}$ cm^{-3}; carbon, $2x10^{17}$ cm^{-3}; and silicon, $5x10^{16}$ cm^{-3}.

2.5.1 Effect of growth conditions

Figure 2.12 compares measured C, O, and Si concentrations with GaN growth temperature. It can be seen that the carbon content decreases as the growth temperature is raised. The same trends were also observed for AlGaN. (For example, for x_{Al}=0.04, C decreased from [C]=$5x10^{17}$ cm^{-3} at T=1050°C to [C]=$1.2x10^{17}$ cm^{-3} at T=1070°C.) The reason for this may be found in Kuech et al.'s discussion of the decrease in carbon incorporation with increasing arsine (AsH_3) in (Al)GaAs[35]. They attributed that to an increased probability of removal of methyl groups (when TMGa is used) from the surface, through conversion to methane by reacting with adsorbed hydrogen atoms produced from the arsine decomposition:

$$CH_3(ad) + H(ad) \rightarrow CH_4(g)\,. \tag{2.4}$$

In the growth of (Al)GaN using ammonia as the nitrogen precursor, significantly better pyrolysis of the NH_3 will occur as the temperature is raised, which results in more adsorbed hydrogen. This may consequently lead to the lower carbon incorporation by increased conversion of methyl groups to methane as in (2.4). The inset in Figure 2.12 shows the logarithm of the carbon concentration plotted versus 1/T. The slope yields an overall reaction enthalpy $\Delta_R H$ of about 170 kJ/mol for the processes involved in carbon incorporation in GaN.

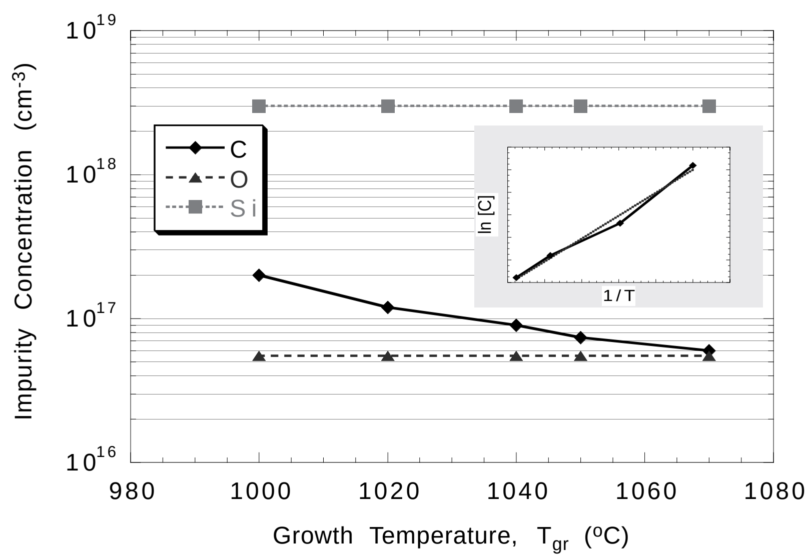

Figure 2.12. Impurity concentrations as a function of growth temperature for GaN grown at 760 torr with TMGa flow of 38.5 μmol/min and NH_3 flow of 0.27 mol/min. The inset shows the logarithm of the carbon concentration plotted versus 1/T.

Oxygen and silicon incorporation did not appear to be affected by growth temperature in the range investigated. However the oxygen concentrations measured were in the vicinity of the detection limit for the SIMS and so no definitive statement can be made. It is expected that oxygen content would decrease with increasing temperature due to the increased volatility of the Ga_2O_3[25]. The silicon incorporation was not expected to vary with temperature due to the fact that disilane was used as the precursor, which is known to have a constant distribution coefficient over a wide range of growth parameters[35].

Considering the previous discussion with respect to the role of the ammonia in impurity incorporation it should come as no surprise that the impurity incorporations are also affected by ammonia flow (V/III ratio). Figure 2.13 maps incorporation of C, O and Si as a function of NH_3 flow for GaN growth.

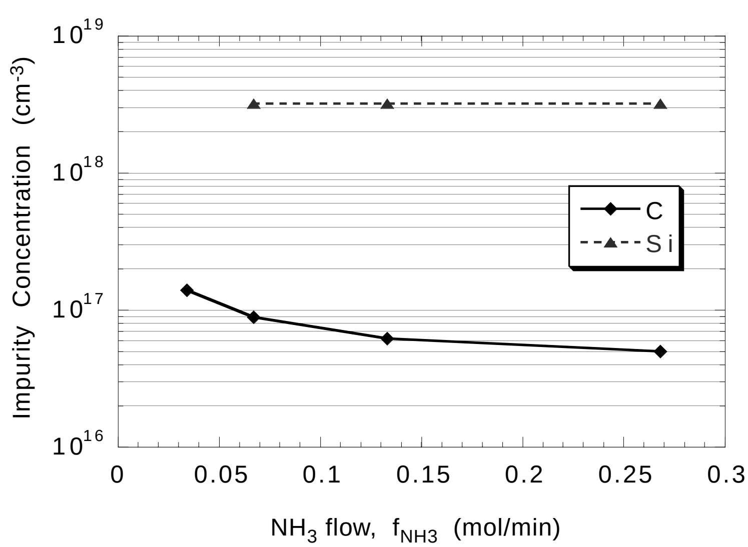

Figure 2.13 Impurity concentration as a function of NH_3 flow for GaN grown at 1070°C, 760 torr and TMGa flow of 38.5 μmol/min.

Once again carbon incorporation is the most strongly influenced, and decreases as ammonia flow increases. (The apparent leveling off of this decrease at higher NH_3 flows is due to the detection limits for carbon being reached and is not true behavior.) The same trend was seen for AlGaN. (For example, for x_{Al}=0.07, C decreased from [C]=$6x10^{17}$ cm^{-3} for f_{NH3}=0.07 mol/min to [C]=$1.2x10^{17}$ cm^{-} for f_{NH3}=0.13 mol/min.) There are two effects to be considered with respect to the decline as ammonia flow increases. Firstly there is the greater availability of hydrogen species for methyl conversion, as discussed above, leading to the observed reduction. Secondly, the increased availability of nitrogen species reduces the likelihood of formation of nitrogen vacancies (which are the preferred carbon sites). Moreover, as the ratio of N-species to C-species increases, the probability of forming a Ga-C bond instead of a Ga-N bond decreases. Unfortunately the requirement of higher NH_3 flow for reduced C incorporation in AlGaN is in direct conflict with the requirement of lower NH_3 flow for improved surface morphology.

Although it appears unaffected by ammonia pressure, the level of oxygen present was again too close to the detection limits for any firm conclusions to be drawn. Other experiments with $Al_{0.25}Ga_{0.75}N$ indicate a slight reduction in the oxygen concentration at higher ammonia flows (from [O]=$2.3x10^{17}$ cm^{-3} at f_{NH3}=0.07 mol/min to [O]=$1.4x10^{17}$ cm^{-3} at f_{NH3}=0.13 mol/min). It would perhaps be expected that the amount of oxygen would increase with ammonia flow, as water in the ammonia is believed to be one of the major sources of oxygen impurities. Obviously, however, the competitive adsorption effect between oxygen and nitrogen dominates, similar to the discussion above for the incorporation of carbon. That is, with an increased supply of nitrogen the likelihood of Ga-O bond formation is suppressed. Finally, as seen for growth temperature, silicon incorporation is scarcely affected by ammonia flows.

In Figure 2.14, the C, O and Si concentrations in GaN are plotted against the TMGa flow. The Si/Ga ratio and the NH_3 flow were kept constant. From the figure it would appear that neither C, O nor Si concentrations are strongly affected by the TMGa input flow and the growth rate. But the impurity concentrations are so close to the detection limits that the true dependencies may be more pronounced than is visible in this figure. In any event, it can be seen that the amount of carbon rises perceptibly with the growth rate. The same behavior was found when performing the study with AlGaN.

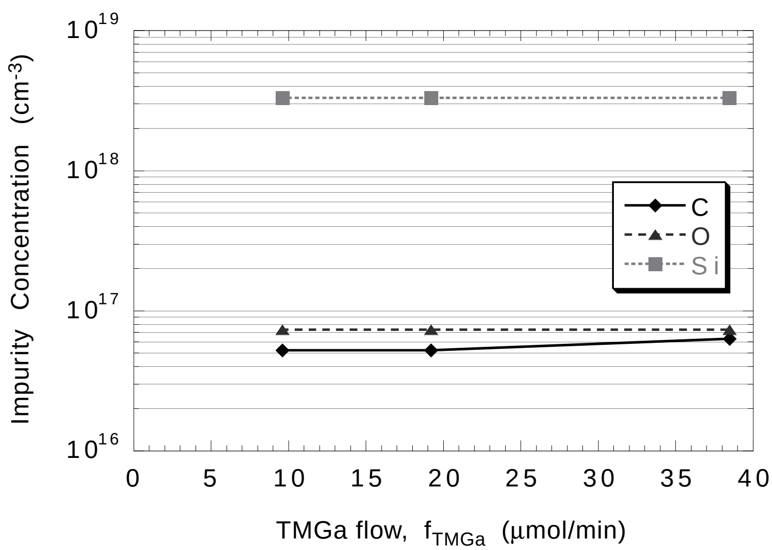

Figure 2.14. Impurity concentrations as a function of TMGa flow for GaN grown at 1070° C, 760 torr and NH_3 flow of 0.27 mol/min.

The increase in carbon concentration is to be expected, as the methyl groups from the TMGa are the presumed source of carbon impurities. It would also be expected that there would be an increase in both oxygen and carbon concentrations, resulting from the lower V/III ratio at higher group III input flows, since the NH_3 flow was kept constant for this segment of the experiment.

2.5.2 Effect of x_{Al}

Figures 2.15a and 2.15b plot [C] and [O] against x_{Al}. Due to the difficulty of growing many thick AlGaN layers of different composition in one structure (cracking and strain often make meaningful comparisons difficult, affecting especially the oxygen incorporation), the plots combine data from several different wafers. Given the sample-to-sample variation always present in the absolute magnitude of results from SIMS analysis, there is a large scatter in the data. However the overall trends are clear, that both oxygen and carbon content increase with the Al content. These results mirror the findings of Kuech et al.[35] for AlGaAs.

Due to the affinity of Al-species for oxygen[36], and considering furthermore that oxygen impurities in the TMAl precursor itself can be a contamination source, it is not surprising that the incorporation of oxygen in the AlGaN is enhanced. The tendency of Al to react with oxygen-bearing compounds is at least partly due to the high stability of the oxide Al_2O_3[37].

a)

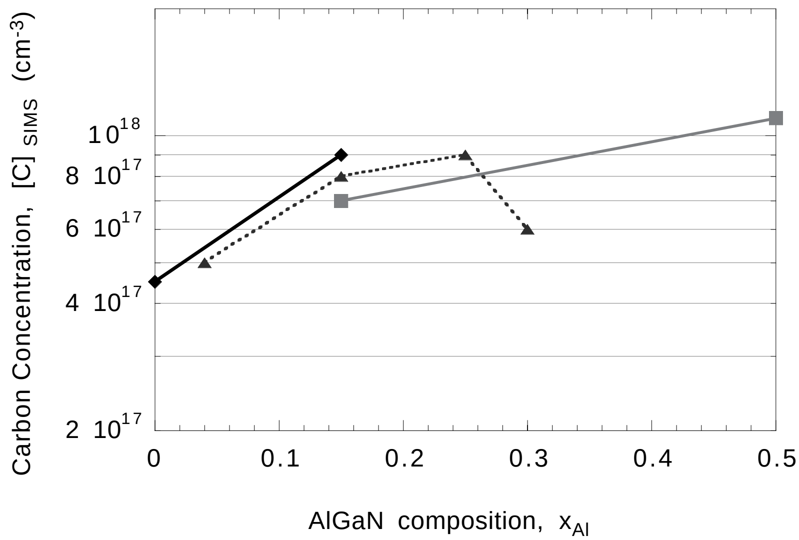

b)

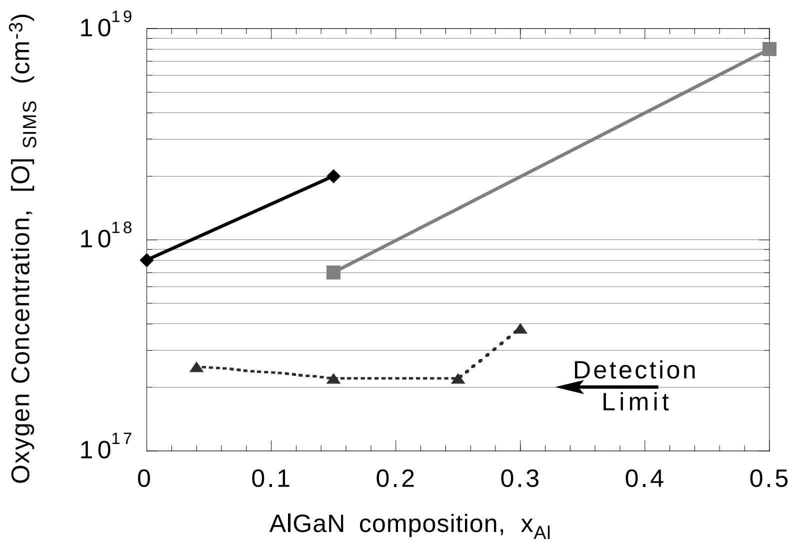

Figure 2.15 Impurity concentration as a function of aluminum content for AlGaN grown at 1080°C and 300 torr. Different symbols/lines indicate data from different wafers. a) Carbon concentration. b) Oxygen concentration.

The increase in carbon concentration could be related to the increased supply of methyl groups due to the addition of TMAl (the Al content was varied by increasing the TMAl flow and keeping TMGa constant). But increasing TMGa in the growth of GaN did not cause such dramatic increases in the carbon concentration. Although the exact reaction pathway for formation of AlGaN from the metalorganic components is not known, the higher carbon concentration in AlGaN is most likely related to the higher bond strength of Al-C (2.9 eV) vs. Ga-C (2.6 eV) [25].

2.5.3 Si incorporation

Figure 2.16 depicts the Si content in $Al_xGa_{1-x}N$ of varying x_{Al}; as a function of Si to group III atomic flow ratio. The data were derived by varying the disilane flow while keeping the group III flow constant, as well as by varying the Al and/or Ga flows at a constant disilane input flow. Again there is scatter in the data due to wafer-to-wafer variation. Despite this the figure does show that the Si incorporation is linear with the flow ratio. Interestingly, this linear dependence exists even though for the growth conditions used, the Al-incorporation efficiency into the solid, k_{Al}, is always considerably smaller than that of gallium, k_{Ga}. This was discussed in depth in Section 2.2.1. Obviously, disilane participates in these pre-reactions, which results in an overall linear dependence of the Si incorporation on the Si/(Ga+Al) ratio, regardless of whether it was the DiSi or the TMAl and/or the TMGa flows that were varied.

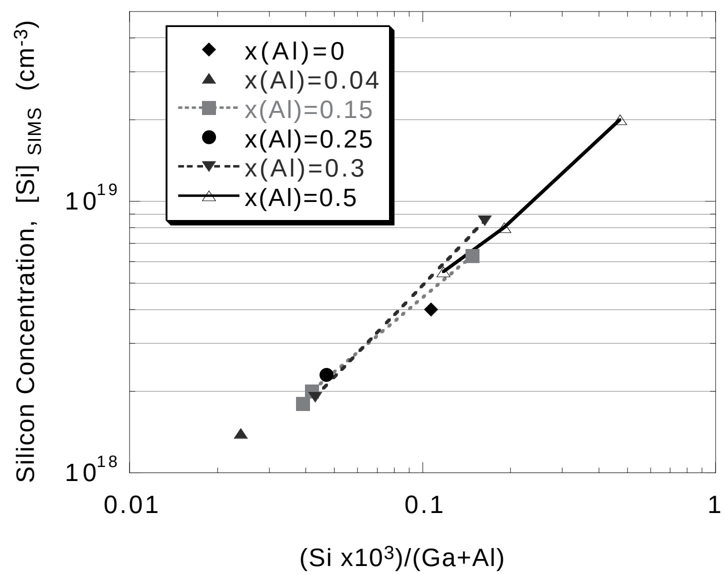

Figure 2.16 Silicon concentration as a function of Si to group III atomic flow ratio, for AlGaN with x_{Al} from 0 to 0.5. Data points were taken from many different wafers. Growth temperature was 1080°C, and flow ratio was varied by changing the DiSi flow and/or the TMAl and/or TMGa flows.

Another, perplexing effect was observed with respect to the silicon doping of the AlGaN. Figure 2.17 exhibits the carbon and silicon concentrations in a selected region from one of the SIMS spectra obtained during this study. Here a small, but distinct, step in carbon content between the doped and undoped regions of the AlGaN is visible. Specifically, the carbon incorporation decreases in the silicon-doped layer. This phenomenon was consistently observed in AlGaN layers of moderate-to-high composition (15% and higher) whereas it was not detected in GaN or $Al_{.07}Ga_{.93}N$. This effect is not well understood and clearly needs to be investigated further, but may be related to the pre-reactions in the gas phase involving the TMAl and the Si_2H_6.

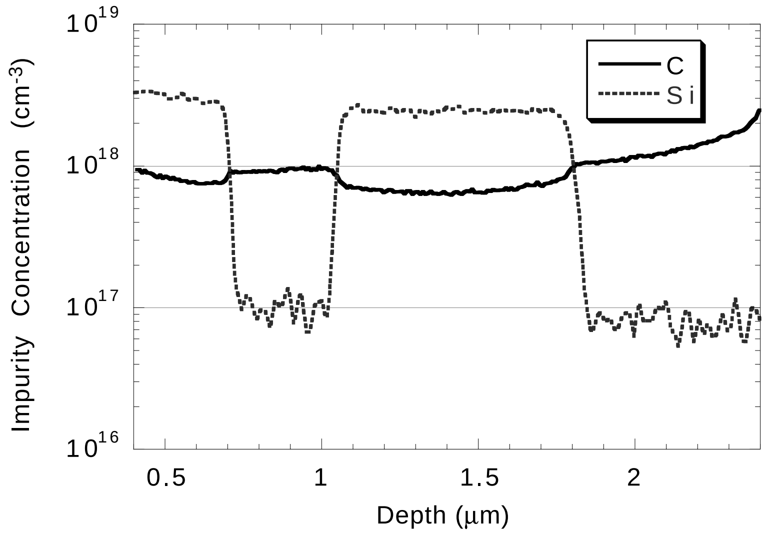

Figure 2.17. Selected region of SIMS results for $Al_{.25}Ga_{.75}N$, showing carbon and silicon impurity concentrations as a function of sputter depth.

2.6 Conclusions

Amongst the primary factors affecting the growth of AlGaN are the low mobility of Al adatoms and high bond strength of Al to N, O and C. Due to these factors extra measures must be taken into account for growth of AlGaN as there is an increased tendency for defect formation compared to GaN, which is exacerbated the higher the Al content. Growth conditions must be tailored to maximize the mobility of the adatoms. Reduction of NH_3 flows (V/III ratio) was found to be most effective for this, although this in turn results in higher impurity (C and O) incorporation. However, raising the growth temperature can help offset this effect. Thus the optimal growth conditions (in our reactor) consisted of a NH_3 flow of 1.5l/min and a growth temperature of 1125°C. Under these conditions a growth rate on the order of 3Å/s was suitable. Threading dislocations, besides being defects themselves, catalyze the enhanced defect formation in AlGaN. For AlGaN layers grown on GaN the use of reduced NH_3 flows combined with growth on LEO GaN can result in a surface morphology that is comparable to the LEO GaN.

2.7 References

1. D. Walker, X. Zhang, A. Saxler, P. Kung, J. Xu, and M. Razeghi, “Intrinsic $Al_xGa_{1-x}N$ detectors for the entire compositional range.” *Proc SPIE* **2999**, 267-274 (1996)

2. S. Ruffenach-Clur, O. Briot, B. Gil, R.-. Aulombard, and J.L. Rouviere, “MOVPE growth and structural characterization of $Al_xGa_{1-x}N$.” *MRS Internet J. Nitride Semicond. Res.* **2,** 27 (1997).

3. M.D. Bremser, W.G. Perry, T. Zhevela, N.V. Edwards, O.H. Nam, N. Parikh, D.E. Aspnes, and Robert F. Davis, “Growth, doping and characterization of $Al_xGa_{1-x}N$ thin film alloys on 6H-SiC(0001) substrates.” *MRS Internet J. Nitride Semicond. Res.* **1,** 8 (1996).

4. M. Shin, A.Y. Polyakov, M. Skowronski, G.S. Rohrer, and R.G. Wilson, “Surface defects in GaN and $Al_xGa_{1-x}N$ epilayers deposited on sapphire by organometallic vapor phase epitaxy.” *Mat. Sci. Forum* **264-268,** 1251-1254 (1998).

5. W.V. Lundin, A.S. Usikov, B.V. Pushnyi, U.I. Ushakov, M.V. Stepanov, N.M. Shmidt, T.V. Shubina, A.V. Sakharov, N.N. Faleev, V.A. Solov’ev, A.A. Sitnikova, Yu.A. Kudriavtsev, B.Ya. Ber, and Yu.M Zadiranov, “Optical and structural studies of thick AlGaN alloy layers and AlGaN/GaN heterostructures on sapphire substrates.” *Mat. Sci. Forum* **264-268,** 1315-1318 (1998).

6. L.J. Schowalter, J.C. Rojo, G.A. Slack, Y. Shusterman, R. Wang, I. Bhat, and G. Arunmozhi, "Epitaxial growth of AlN and $Al_{0.5}Ga_{0.5}N$ layers on aluminum nitride substrates." *J. Cryst.* Growth **211,** 78-81 (2000).

7. Y. Koide, N. Itoh, K. Itoh, N. Sawaki, I. Akasaki, "Effect of AlN buffer layer on AlGaN/α-Al_2O_3 heteroepitaxial growth by metalorganic vapor phase epitaxy." *Jpn. J. Appl. Phys*. **27,** 1156-1161 (1988).

8. F. Omnès, N. Marenco, B. Beaumont, Ph. de Mierry, E. Monroy, F. Callè, and E. Muñoz, "Metalorganic vapor-phase epitaxy-grown AlGaN materials for visible-blind ultraviolet photodetector applications."*J. Appl. Phys.* **86,** 5287-5292 (1999).

9. J.H. Mazur, M. Benamara, Z. Liliental-Weber, W. Swider, J. Washburn, C.J. Eiting,and R.D. Dupuis, "Effect of the doping and the Al content on the microstructure and morphology of thin $Al_xGa_{1-x}N$ layers grown by MOCVD." *MRS Internet J. Nitride Semicond. Res.* **5S1,** W3.77 (2000).

10. K.C. Zeng, J.Y. Lin, and H.X. Jiang, "Effects of alloy disorder on the transport properties of $Al_xGa_{1-x}N$ epilayers probed by persistent photoconductivity." *Appl. Phys. Lett.* **76**, 1278-1280 (2000).

11. M. Iwaya, N. Hayashi, T. Kashima, H. Amano, and I. Akasaki, "Realization of crack-free and high-quality thick $Al_xGa_{1-x}N$ for UV optoelectronics using low-temperature interlayer." *Appl. Surface Sci.* **159-160**, 405-413 (2000).

12. A.V. Sampath, E. Iliopoulos, K. Seth, Y. Fedyunin, H.M. Ng, P. Lamarre, Z. Feit, and T.D. Moustakas, "GaN photodiodes grown by MBE on HVPE and ELO-HVPE GaN/sapphire substrates." *Proc. SPIE* **3948,** 311-318 (2000).

13. D.J. Lambert, M.M. Wong, U. Chowdhury, C. Collins, T. Li, H.K. Kwon, B.S. Sheldon, T.G. Zhu, J.C. Campbell, and R.D. Dupuis, "Back illuminated AlGaN solar-blind photodetectors." *Appl. Phys. Lett.* **77,** 1900-1902 (2000).

14. M.D. McCluskey, C.G. Van de Walle, N.M. Johnson, D.B. Bour, and M. Kneissl, "*DX* Centers in AlGaN." *Intl. J. of Mod. Phys*. **B13,** 1363-1378 (1999).

15. C.G. Van de Walle, C. Stampfl, J. Neugebauer, M.D. McCluskey, and N.M. Johnson, "Doping of AlGaN alloys." *MRS Internet J. Nitride Semicond. Res.* **4S1,** G10.4 (1999).

16. C. Skierbiszewski, T. Suski, M. Leszczynski, M. Shin, M. Skowronski, M.D. Bremser, and R.F. Davis, "Evidence for localised Si-donor state and its metastable properties in AlGaN." *Appl. Phys. Lett.* **74,** 3833-3835 (2000).

17. L. Akasaki and H. Amano in *GaN,* edited by J.I. Pankove and T.D. Moustakas (Academic, New York, 1998) **1**, 459-472.

18. O. Ambacher "Growth and applications of group III-nitrides." *J. Phys. D: Appl. Phys.* **31,** 2653-2710 (1998).

19. C.J. Eiting, D.J.H. Lambert, H.K. Kwon, B.S. Shelton, M.M. Wong, T.G. Zhu, and R.P. Dupuis "Characterization of AlGaN/GaN heterostructures grown by metalorganic chemical vapor deposition." *Phys. Stat. Sol. (b)* **216,** 193-197 (1999).

20. B.P. Keller, S. Keller, D. Kapolnek, W.N. Yiang, Y.-F. Wu, H. Masui, X. Wu, B. Heying, J.S. Speck, U.K. Mishra, and S.P. DenBaars, "Metalorganic chemical vapor deposition growth of high optical quality and high mobility GaN." *J. Electron. Mater*. **24**, 1707-1709 (1995)

21. A. Thon & T. F. Kuech, "High temperature adduct formation of trimethylgallium and ammonia." *Appl. Phys. Lett.* **69**; 55-57 (1996).

22. J. Han, J.J. Figiel, M.H. Crawford, M. A. Banas, M.E. Bartram, R.M. Biefeld, Y.K. Song, and A.V. Nurmikko, "OMVPE growth and gas-phase reactions of AlGaN for UV emitters." *J. Cryst. Growth* **195,** 291-296 (1998).

23. T.G. Mihopoulos, V. Gupta, and K.F. Jensen, "A reaction-transport model for AlGaN MOVPE growth." *J. Cryst. Growth* **195,** 733-739 (1998).

24. F. Nakamura, S. Hashimoto, M. Hara, S. Imanaga, M. Ikeda, and H. Kawai, "AlN and AlGaN growth using low-pressure metalorganic chemical vapor deposition." *J. Cryst. Growth* **195,** 280-285 (1998).

25. G.B. Stringfellow *Organometallic Vapor-Phase Epitaxy* (1989) Academic Press, San Diego.

26. A. Koukitu, N. Takahashi, T. Taki, and H. Seki, "Thermodynamic analysis of $In_xGa_{1-x}N$ alloy composition grown by metalorganic vapor phase epitaxy." *Jpn. J. Appl. Phys*. **35,** L673-675 (1996) A. Koukitu, N. Takahashi, and H. Seki, "Thermodynamic study on metalorganic vapor-phase epitaxial growth of group III-nitrides." *Jpn. J. Appl. Phys*. **36,** L1136-1138 (1997).

27. H. Marchand, X.H. Wu, J.P. Ibbetson, P.T. Fini, P. Kozodoy, S. Keller, J.S. Speck, S.P. DenBaars, and U.K. Mishra, "Microstructure of GaN laterally overgrown by metalorganic chemical vapor deposition." *Appl. Phys. Lett.* **73**, 747-749 (1998).

28. X.H. Wu, P. Fini, E.J. Tarsa, B. Heying, S. Keller, U.K. Mishra, S.P. DenBaars, and J.S. Speck "Dislocation generation in GaN heteroepitaxy." *J. Cryst. Growth* **189/190,** 231-243 (1998).

29. S. Porowski, and I. Grzegory, "Phase diagram of AlN." *Properties of Group III Nitrides*, J.P. Edgar, Ed., London: INSPEC, 1994.

30. Y. Zhang, and J. Singh, "Charge control and mobility studies for an AlGaN/GaN high electron mobility transistor." *J. Appl. Phys*. **85,** 587-594 (1999).

31. L. Hsu and Walukiewicz "Electron mobility in $Al_xGa_{1-x}N$/GaN heterostructures." *Phys. Rev. B* **56,** 1520-1528 (1997).

32. D. Korakakis, K. F. Ludwig, Jr., and T. D. Moustakas, "Long range order in $Al_xGa_{1-x}N$ films grown by molecular beam epitaxy." *Appl. Phys. Lett.* **71**, 72-74 (1997)

33. B. Neubauer, A. Rosenauer, G. Gerthsen, O. Ambacher, and M. Stutzmann, "Analysis of composition fluctuations on an atomic scale in $Al_{0.25}Ga_{0.75}N$ by high-resolution transmission electron microscopy." *Appl. Phys. Lett.* **73**, 930-932 (1998)

34. A.V. Buyanov, J.A. Sandberg, B. E. Sernelius, P.O. Holtz, J.P. Bergman, B. Monemar, H. Amano and I. Akasaki, "Photoconductivity in n-type modulation-doped GaN/AlGaN heterostructures." *J. Cryst. Growth* **189/190**, 758-762 (1998)

35. T.F. Kuech, M.A. Tischler, R. Potemski, F. Cardone, and G. Scilla, ”Doping and dopant behavior in (Al,Ga)As grown by metalorganic vapor phase epitaxy.” *J. Cryst. Growth* **98,** 174-187 (1989).

36. T.F. Kuech, D.J. Wolford, E. Veuhoff, V. Deline, P.M. Mooney, R. Potemski, and J. Bradley, “Properties of high-purity $Al_xGa_{1-x}As$ grown by metal-organic vapor-phase-epitaxy technique using methyl precursors.” *J. Appl. Phys*. **62,** 632-643 (1987).

Chapter 3. Dislocations in GaN and their effect on p-i-n photodetectors.

As the technology for the growth of GaN has evolved, so has the knowledge of defects, which primarily result from the inadequate substrates used. Alongside have developed techniques to circumvent or eliminate these defects. In this chapter, the effect of dislocations on GaN-based p-i-n photodiodes will be examined. This particularly includes the effect of reduction of threading dislocation density (TDD) by various substrate and overgrowth alternatives. The primary goals of the investigation were to improve the leakage current and the cutoff characteristics of photodiodes.

3.1 Defects present in (Al)GaN

Whilst all defects, including extended and point defects (native and impurity) are of concern for ideal photodetector performance, the high threading dislocation density (TDD) present in GaN devices has been a primary concern in UV photodiode development over the last 5-10 years.

3.1.1 General crystal defect theory

A fine introduction to the concept of defects is given in the book "Introduction to Dislocations" by Derek Hull[1], and is summarized here. Point defects in a crystal occur when an atomic site is substituted or vacant, or an interstitional site is occupied. Substitutions and interstitial defects can arise by introduction of an impurity to the lattice or by displacement of an atom in the parent lattice from its ideal position. Stacking faults, which are surface defects, occur when the regular sequence of crystal plane stacking is interrupted. Threading dislocations - with which this chapter is primarily concerned - are linear lattice deformations, the two basic geometries of which are edge and screw dislocations, formed by application of a shear stress to the lattice. Edge dislocations occur when a partial plane of atoms is inserted into or removed from the crystal, thus displacing the atomic planes on either side. Screw dislocations occur when part of two adjacent lattice planes are shifted laterally with respect to each other. In many cases dislocation lines can have a mixed edge and screw character. Finally, grain boundaries are defects formed when a crystalline solid grows as a number of randomly oriented grains (known as a low angle boundary when the misorientation between the grains is small and the boundary consists of an array of dislocations), and twin boundaries occur when adjacent planes of a crystal are mirror images of each other. Further details regarding the basic definitions of defects can be found in Appendix A.

Due to the lattice mismatch between GaN and sapphire, true progress in epitaxial growth of GaN was not obtained until two-step growth initiation, involving a nucleation layer, was adopted and perfected by Amano et al[2]. At UCSB a low-temperature GaN nucleation layer was developed and optimized by Keller et al.[3,4], and was used for the growth on sapphire substrates in this work. When utilizing a nucleation layer between the substrate and the epitaxial crystal, the nucleation layer determines the occurrence of dislocations in the epitaxial crystal[5,6]. Furthermore, it is the nature of the nucleation layer after it is annealed during the temperature ramp, which determines the growth of the high temperature GaN layer[7]. If nucleation conditions result (after deposition and heating to overlayer growth temperature) in large, sparse islands which coalesce to form the epitaxial film, much of the stacking disorder manifests itself in dislocations along the basal plane which propagate laterally. Threading dislocations are also formed, some of which (of mixed character), are within the islands, and some of which (mostly pure edge) are formed at the coalescence boundary of the islands. On the other hand, with a very dense nucleation layer involving little lateral overgrowth for coalescence, the epitaxial layer contains a huge pure edge threading dislocation density formed at the nucleation layer grain boundaries.

Nucleation layers on SiC substrates require a different optimization, due to the different thermal and lattice mismatch between GaN, AlN and SiC compared to sapphire: $a_{Al2O3} > a_{GaN} > a_{AlN} > a_{SiC}$ and $\alpha_{Al2O3} > \alpha_{GaN} > \alpha_{AlN} > \alpha_{SiC}$[8]. Waltereit et al. measured strain in GaN grown on 6H-SiC with and without an AlN nucleation layer[9]. The lattice mismatch introduces compressive strain, whereas cooling introduces tensile strain. Without an AlN nucleation layer the compressive lattice mismatch strain was relieved during growth, with the film under tension after cooling due to the thermal mismatch, which caused cracking. With an AlN nucleation layer, which was coherently grown, there was only a slight compressive mismatch remaining after cool-down. Several groups have also analyzed the initial growth mechanism for AlGaN directly deposited on SiC without a nucleation layer, and found that there is an Al-rich layer deposited at the interface[10,11]. This Al-rich layer again acts to relieve the lattice strain during growth.

In addition to the identification of the defects present in GaN, many other experimental studies have provided insights into the consequences for electrical and optical behavior. For example, scanning capacitance measurements by Hansen et al.[12] confirmed the presence of negative charge in the area surrounding dislocations. Simultaneous scanning transmission microscopy and ballistic electron emission microscopy measurements by Brazel et al.[13] revealed the presence of localized traps, both acceptor-like and donor-like, in the vicinity of dislocations with a screw component. Additionally, compensation of donors in GaN:Si has been shown to decrease with decreasing edge-type dislocation density.[14] Calculations by Asbeck et al.[15] also predict piezoelectric charges resulting from the intersection of dislocations with surfaces and interfaces.

Further defect issues such as ordering and increased defect formation, obtained with addition of Al to GaN to form an alloy, were discussed in detail in Chapter 2.

3.1.2. Dislocation reduction techniques for GaN

As alluded to above, the characteristics of the nucleation layer strongly affect the dislocation density in the eventual epitaxial film. For epitaxial growth of GaN with a GaN nucleation layer, experiments at UCSB[3,4] showed the importance of short nitridation time of the sapphire as well as reduced TMGa flow to obtain an initially rough nucleation layer prior to the temperature ramp. Several papers have also described the benefits of depositing a thin SiN layer prior to the deposition of the GaN nucleation layer[16,17,18]. Even after optimization of the nucleation layer for GaN growth on sapphire and SiC, the TDD in the GaN is still generally in the range 10^8-10^9 cm^{-3}. Several groups have pioneered the use of different interlayers to further reduce the TDD. These include use of a SiN submonolayer that modifies the surface mobility of GaN layers deposited subsequently, resulting in reduction of TDD, mostly of edge character[19,20]. This will be discussed in more detail later, with respect to development of such a technique as part of this work. Amano et al. [21] have demonstrated that the use of a low-temperature AlN layer can result in GaN and AlGaN overlayers with fewer dislocations with a screw component. Furthermore, several groups have reported on the annihilation of threading dislocations at interfaces between GaN and AlGaN[22,23].

Finally, the reduction of the TDD by LEO techniques has been well documented by many groups, including UCSB[24], with the first detailed presentation of this reduction being a TEM study by Zheleva et al.[25]. Thorough experimental studies and modeling of the effect of mask orientation and layout, as well as growth parameters, on lateral growth rates, overgrowth profiles, and tilt in the LEO GaN have been made, and will not be detailed here[26,27,28].

3.1.3 Effects of defects on (Al)GaN photodetectors

Below is given a review of literature regarding the effect of defects on various types of GaN and AlGaN photodetectors. The work in this chapter is principally concerned with the effect of dislocations on photodiodes. In general, different mechanisms are involved with photoconductors, however it is still instructive to examine the knowledge base for defect activity in GaN-based photoconductors as well.

The most visible of issues for GaN photoconductors has been the high gain, long response times and frequency- and optical power-dependence of the responsivity – examples from early work were given in Chapter 1. The gain of a photoconductor is given by $g = \frac{\tau}{t_t}$, in which τ is the excess-carrier recombination lifetime time and t_t is the electron transit time across the detector. (The electrons travel faster than the holes, and can traverse the photoconductor/external circuit many times before they recombine with the holes.) Ideally high gain is obtained as the result of a short transit time of the electrons across the photoconductor. This requires high electron mobility. In the case of GaN photoconductors the recombination lifetime is artificially inflated by a long residence time of the minority carriers in traps, reducing the probability of recombination. Thus there is a high gain but it is at the expense of a long response time.

Many experiments have investigated the mechanisms for the long response times and high gain, and found that acceptor levels trapping photogenerated holes were the cause in n-type photoconductors[29,30,31]. Furthermore, Huang et al.[32] showed that by reducing the density of hole traps by altering growth conditions (although the actual source of the hole trap was undetermined) response time could be reduced and yet responsivity increased. Comparisons of GaN photoconductors grown on sapphire and HVPE GaN templates have shown that the sharpness cutoff at the band-edge can be improved[33,34], with Redwing et al. demonstrating 7 orders of magnitude drop in response within 20nm of the peak. With these improvements the response times are still on the order of ms. Nobody has yet demonstrated the behavior of GaN photoconductors in the absence of TDD such as on LEO GaN – in the study mentioned above the HVPE GaN still had a significant TDD.

In photovoltaic devices it has been the direct effect of threading dislocations that has been studied the most. Kozodoy et al.[35] were the first to demonstrate the reduction in leakage current obtained for GaN p-n structures deposited on LEO-GaN. Following those promising results we deposited a GaN/AlGaN/GaN p-i-n solar-blind detector structure on LEO-GaN. As well as a reduction in leakage current we observed an improvement in response time and in sharpness of cutoff. These results will be discussed in depth later in this chapter[36]. Subsequent investigations by other groups revealed similar results with a sharper cutoff and reduced response time and leakage current for GaN Schottky barrier photodiodes on LEO-GaN[37], and a sharper cutoff for $Al_{0.7}Ga_{0.3}N$ p-i-n photodiodes on LEO-GaN (leakage currents were not reported for those diodes)[38].

In addition to the benefits of LEO, there have been other studies detailing the effect of defects. Analysis of leakage current in GaN p-π-n photodiodes without TDD reduction determined that it resulted from defect hopping in the π-layer[39], although the nature of the defects was not revealed. Importantly, with use of the low-temperature AlN interlayer technique discussed above, in which mixed character but not edge-type dislocations were eliminated, Pernot et al. recently reported that leakage current was reduced to very low levels: 0.1nA/cm^2 at a reverse bias of 10V for $Al_xGa_{1-x}N$ (x_{Al} = 0 to 0.44) MSM[40] photodetectors and 0.4-3.5 nA/cm^2 at a reverse bias of 5V for p-GaN/i-$Al_{0.44}Ga_{0.56}N$/n- $Al_{0.44}Ga_{0.56}N$ photodiodes[41]. Without the interlayer, the MSM photoconductor properties became worse (increase in response time and PPC effects, as seen for photoconductors) as x_{Al} was increased and the material quality correspondingly decreased. This degradation of photodetector characteristics with increasing Al content has also been observed by Monroy et al. as a decrease in responsivity for $Al_xGa_{1-x}N$ p-i-n photodiodes ($0 \leq x_{Al} \leq 0.15$) [42], and as an increase in leakage current and ideality factor and decrease in cutoff sharpness and responsivity for $Al_xGa_{1-x}N$ Schottky barrier photodiodes ($0 \leq x_{Al} \leq 0.35$) [43].

3.1.4 Synopsis of this chapter

In this chapter several different studies of the effect of threading dislocations on photodiode characteristics are presented. In Section 3.2 the first study looks at the effect of different threading dislocation densities and character on GaN p-i-n diode leakage current and spectral response. As part of this, a technique utilizing silicon nitride/InGaN interlayers to reduce edge-type dislocation density is detailed. In Section 3.3 leakage current in GaN p-i-n diodes with a reduced TDD is examined as a function of electric field/intrinsic layer thickness, sidewall passivation, and diode size/perimeter-to-area. Finally in Section 3.4 the photodetector characteristics (leakage current, spectral response, and pulsed response) of p-GaN/i-AlGaN/n-GaN diodes are compared with and without threading dislocation reduction.

There are several transmission electron microscopy (TEM) images presented in this and the following chapter. The samples were prepared for TEM by wedge polishing followed by standard Ar^+ ion milling, and the images were recorded on a JEOL 2000FX microscope operated at 200kV. The AFM images were obtained using either a Digital Instruments Nanoscope III (smaller area scans) or a Digital Instruments D-3000 (larger area scans), both operated in tapping mode.

3.1.5 Mechanisms of p-i-n photodiodes

In a photodiode, current can result from light absorption (for light with at least the bandgap energy) in the bulk or the depletion regions. Figure 3.1 contains a) the schematic cross-section of a p-i-n photodiode, b) a band diagram (not to scale) figuratively indicating photocurrent mechanisms and c) the current-voltage characteristics for an illuminated and a non-illuminated photodiode.

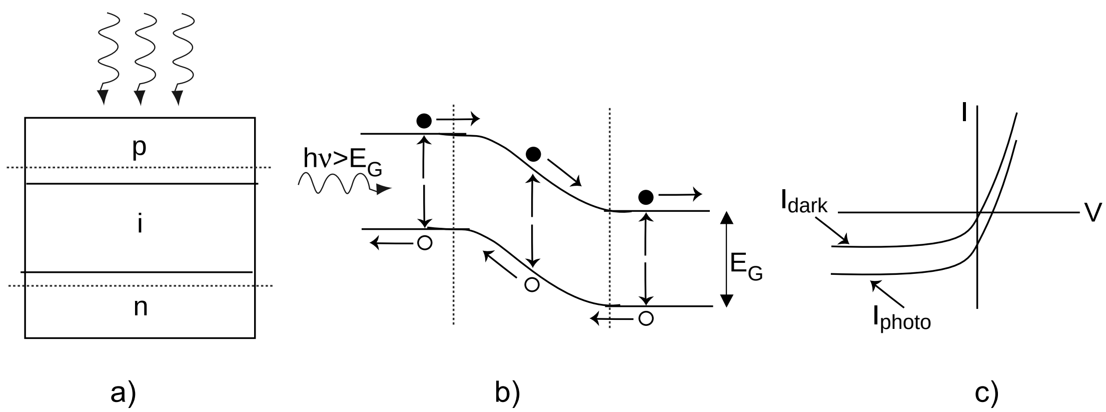

Figure 3.1 Operation of p-i-n photodiode (not to scale). a) Device cross-section – dotted lines indicate boundaries of depletion region. b) Band diagram indicating mechanism of photocurrent caused by electron-hole pair generation. c) I-V characteristics with (I_{photo}) and without (I_{dark}) above-bandgap illumination.

The electron-hole pairs generated in the depletion region are separated and swept by the high field towards the bulk regions, where they recombine as majority carriers. Also, minority carriers generated in the bulk regions within a diffusion length of the depletion region will, upon reaching the depletion region, be accelerated by the electric field to become majority carriers on the other side. The extension of the depletion region by an i-region increases the ratio of drift current (a faster process) to diffusion current. Together these two current mechanisms result in a downward shift of the I-V curve. In general photodiodes are operated either at zero bias (photovoltaic mode) or in reverse bias. This maximizes the difference between the dark current and the photocurrent, and thus maximizes the sensitivity. All diodes in this work were measured in the photovoltaic mode.

The dark current at reverse bias is referred to as the leakage current. It can result from numerous sources in the diode. Surface leakage currents include generation from surface states and tunneling induced near the surface. Surface leakage can be reduced by passivation or other surface treatment that ties up dangling bonds and thus reduces the density of surface states. Thermally generated currents include diffusion current in the bulk regions, generation-recombination current, inter-band and trap-to-band tunneling. Traps are expected to occur in the material as a result of both point defects and dislocations, which are known to be present.

Figure 3.2 indicates several of these thermal mechanisms: (i) intrinsic generation, (ii) trap-assisted generation (via deep or shallow traps), (iii) band-to-band tunneling, and (iv) trap-assisted tunneling. As discussed for photogenerated carriers, thermally generated carriers will contribute to leakage current if they are generated in or within a minority carrier diffusion length of the depletion region. In reverse bias, generation will always be the dominant process over recombination in the depletion region, but for wide gap semiconductors such as GaN the thermal excitation rate is small. Thus the diffusion and generation-recombination currents will be negligible, unless trap-assisted.

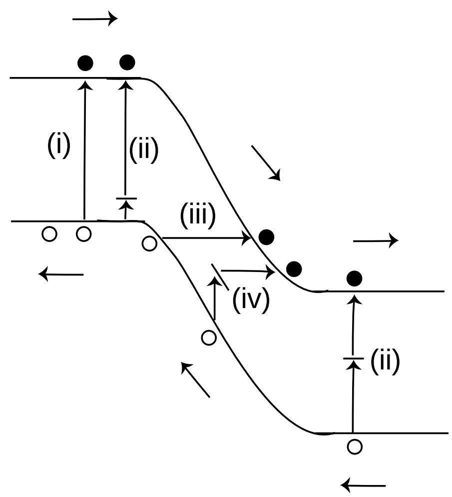

Figure 3.2 Examples of thermal generation processes in a p-i-n diode under reverse bias. (i) Intrinsic generation, (ii) trap-assisted generation, (iii) direct band-to-band tunneling and (iv) trap-assisted tunneling.

3.1.6 Device layout, processing and measurements

The cross-section for a typical diode structure for the devices discussed in this chapter is drawn in Figure 3.3a, with a photograph (surface view) of a processed diode in Figure 3.3b. Unless otherwise specified, device fabrication consisted of the following steps. The first step was activation of the p-layer by annealing at 950°C for 3 minutes in a N_2 ambient. Device definition began with deposition of thick Pd/Au (250Å/2000Å) p-contacts, which were annealed in N_2 at 650°C for 1 minute. This was followed by deposition of a semi-transparent Pd layer (30Å) across the remaining active surface of the diode. The mesa was then defined around this area by means of a Cl_2-based reactive ion etch to the n-layer. Ti/Al (100Å/2000Å) was deposited for n-contact formation, again annealed at 650°C. Then 2000Å-3000Å of SiO_2 was deposited everywhere (including sidewalls) by PECVD for isolation of the contact pads. After HF wet etching of via holes, thick Ti/Au (200Å/3000Å) contact pads were deposited. (A more detailed description of the fabrication process is given in appendix B.)

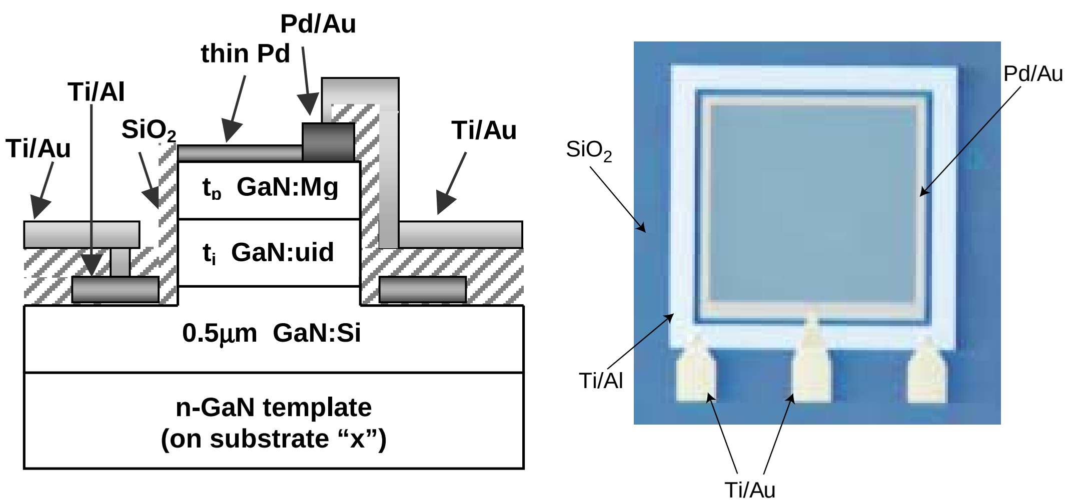

a) b)

Figure 3.3 GaN p-i-n diode structure (general). a) Schematic of cross-section. b) Photograph of processed 300µm x 300µm diode.

The current-voltage characteristics of the diodes were measured using a HP 4145 or 4155 Semiconductor Parameter Analyzer. All devices discussed in this thesis exhibited rectifying (diode) behavior. The forward bias characteristic for a representative diode (300μm x 300μm device; GaN p-i-n with t_i = 0.8μm and t_p=600Å) is given in Figure 3.4a. In Figure 3.4b the characteristic is redrawn using a semi-log scale. Dotted lines are drawn indicating the exponential dependence for an ideal p-n diode (ideality factor n=1) and an ideal diode under high injection conditions (n=2). It is apparent that the measured current is non-ideal, which was the case for all diodes measured.

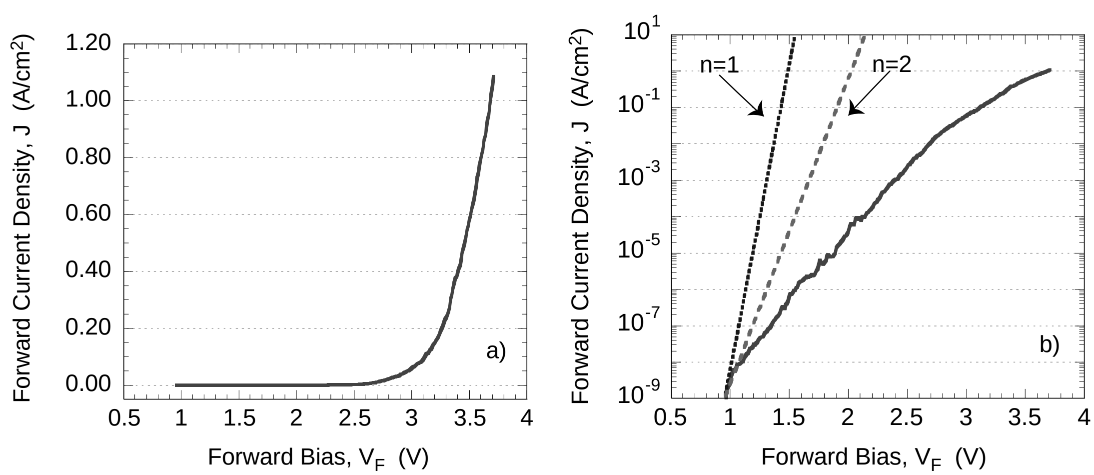

Figure 3.4 Forward bias characteristic of a typical GaN p-i-n diode plotted with a) linear scale, and b) semi-log scale. Dotted lines indicate slope for ideality factor n=1 and n=2 for ideal p-n diode.

The deviation is due to a combination of several factors. For p-i-n diodes under high injection conditions, recombination in the i-region results in a power-law dependence rather than exponential[44]. The characteristic steadily worsens with voltage as the diffusion length of the carriers in the i-region decreases.[45]. The higher the density of impurity centers the higher the recombination rate will be. This is exacerbated by

Auger recombination and by carrier-carrier scattering. Also, due to the high resistivity of the p-GaN the diodes have a high series resistance that further degrades the characteristic. The bulk of the I-V studies presented in this and the following chapter concern the reverse bias characteristics of the diodes, as part of the investigations into the noise performance of the detectors.

To assess the spectral behavior of the detectors, responsivity measurements were accomplished using a 75W xenon arc lamp, with wavelength selection using a monochromator. A lock-in-amplifier and low-noise current pre-amplifier were used to measure the signal, which was mechanically chopped at 310Hz. The power density of the excitation was determined with a calibrated UV Si photodetector.

The effect of including the semi-transparent current-spreading Pd layer is shown in Figure 3.5. 500μm x 500μm devices (GaN p-i-n with t_i = 0.6μm and t_p=600Å) were fabricated with and without the 30Å Pd layer. It can be seen from the spectral response that the device with the semi-transparent contact layer has a much higher photocurrent. Obviously the increased current collection afforded by this contact layer far outweighs the loss in efficiency due to absorption in the Pd (30Å Pd will have a transmission of 75% for light of 3.4-5 eV).

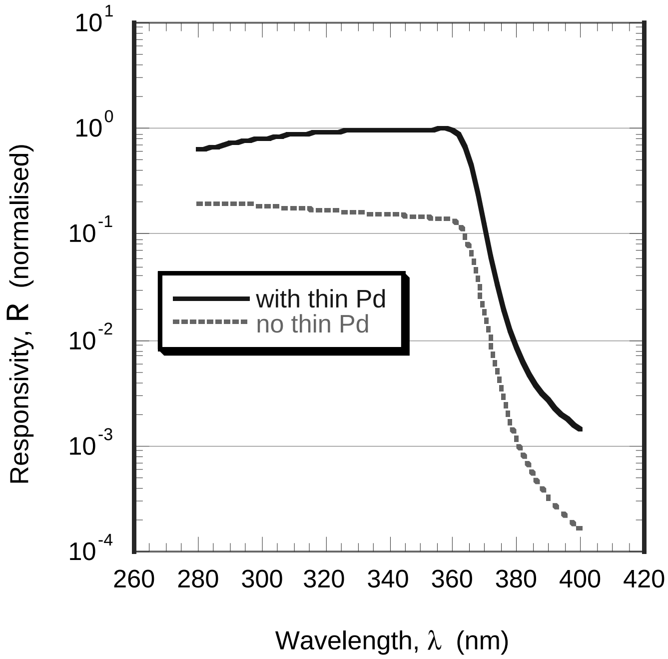

Figure 3.5 Measured responsivity for GaN p-i-n diodes with and without 30Å semi-transparent Pd contact layer. (normalized to peak responsivity of diode with thin Pd layer).

3.2 Threading dislocation reduction – effect on GaN p-i-n photodiodes

In order to provide a broad investigation of the effect of threading dislocations on photodiode leakage current and responsivity characteristics, a simple GaN p-i-n diode structure was deposited on standard templates as well as on several templates to which various dislocation reduction techniques had been applied. These were a template with SiN/InGaN interlayer technique in which the density of pure edge dislocations has been reduced, a GaN template on SiC substrate with an AlN nucleation layer, in which the mixed character TDD is very low, and an LEO template in which both edge and mixed TDD are significantly reduced. These are described in more detail below, apart from the LEO process, which was described in Section 2.2.5.

3.2.1 XRD as a tool for TDD comparison

Whilst TEM measurements are time-consuming and expensive, XRD measurements are a fast and convenient method for assessment of the TD density and makeup in films. Heying et al.[46] demonstrated the correlation between FWHM values of rocking curves both on-and off-axis with the edge and mixed components of the TDD in GaN. For GaN films grown on (0001) sapphire, as is the case here, the (0002) planes are not distorted by edge-type dislocations in the [0001] line directions, and the (0002) rocking curves are only sensitive to the screw TD content in the films (this includes mixed character TD's). On the other hand, the $(10\bar{1}2)$ and the $(20\bar{2}1)$ rocking curve peaks are broadened by TD's with either screw or edge character. Srikant et al. modeled this for epitaxial films that consist of a mosaic structure of slightly misoriented sub-grains[47] (this includes GaN on sapphire). Their model demonstrated that the sensitivity towards the tilt of the subgrains increases, the closer the inclination is to being in-plane. Thus the $(20\bar{2}1)$ rocking curve, at angle of 70° to the axis, will mostly reflect the pure edge TDD. They also point out, though, that the mosaic character determined by the XRD will only include dislocation networks that result in a misorientation between the film and the substrate. However some edge-type dislocations will result in aligned subgrains and therefore have no effect on the tilt and twist of the subgrains, i.e. the mosaic.

3.2.2 SiN/InGaN interlayer technique for TDD reduction

A method of dislocation reduction utilizing a submonolayer of silicon nitride (Si_xN_y) was developed as part of this work. This involved selective island growth of thin InGaN layers on top of the Si_xN_y. (In other work at UCSB, InGaN islands had been observed to grow in a spiral growth mode around threading dislocations with a screw component after partial passivation of the GaN surface with Si_xN_y[48].) Si_xN_y was deposited on top of a standard GaN template at the same temperature as the GaN (1070°C) by flowing NH_3 and DiSi. Then a 12nm thick $In_{0.1}Ga_{0.9}N$ layer was deposited at 790°C, followed by another GaN layer at 1070°C. This was repeated either two or four times. The Si_xN_y layer was either 0.07 or 0.14 Å.

Figure 3.6 indicates the results of XRD measurements for the different combinations of interlayers. If the model of Srikant et al.[47] is valid for the dislocations in the overgrown layers (if they affect the mosaic), the off-axis XRD FWHM values (shown here in units of arc-seconds) reveal a decrease in TDD compared to the underlying templates. In Figure 3.6a, samples without, with two, and with four interlayers are compared to study the effect of the number of interlayers. The underlying GaN template was 0.5μm, with 0.5μm between interlayers, and the total thickness after capping with GaN was kept constant at 3μm. The (0002) FWHM values were relatively unaffected by the number of interlayers, indicating the TDD with a screw component is unchanged. However, the $(10\bar{1}2)$ FWHM changes with the number of interlayers. Whilst the first two interlayers resulted in a decrease in the $(10\bar{1}2)$ FWHM, an increase to four interlayers caused it to increase again.

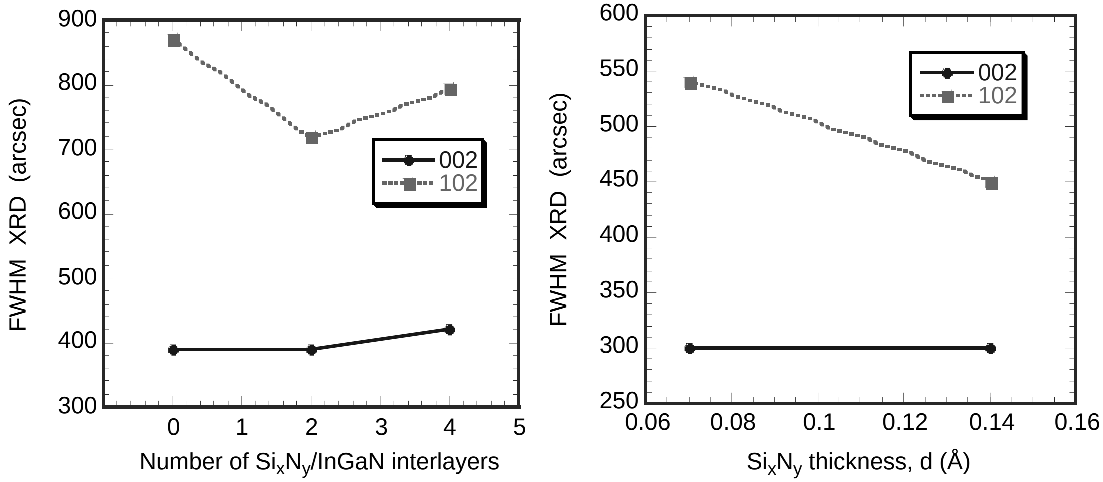

a) **b)**

Figure 3.6. FWHM of the (0002) and ($10\bar{1}2$) diffraction peaks for samples with silicon nitride/InGaN interlayers with a) different number of interlayers and b) different silicon nitride thickness.

In Figure 3.6b, samples with a Si_xN_y thickness of 0.07Å and 0.14Å are compared. For these wafers the underlying GaN template was 3µm, with 0.5µm GaN between two interlayers, and a GaN cap thickness of 2.5µm. (Note that the thicker underlying template results in an overall reduced TDD compared to the wafers in Fig 3.6a.) Here it can be seen that increasing the thickness of the Si_xN_y layer results in a lower ($10\bar{1}2$) FWHM. Other experiments utilizing this technique for GaN on Si revealed that increasing the thickness beyond 0.14Å was again detrimental. Thus the template used in the photodetector study to be described below utilized two (on a 2µm thick GaN template) with a nitride thickness of 0.14Å. This combination had the lowest ($10\bar{1}2$) FWHM and thus, if the mosaic model applies, the lowest edge-type TDD of the above wafers. Preliminary TEM studies were inconclusive as to the elimination of edge-type TD's using this technique. Note that the technique was only investigated using Si_xN_y and InGaN interlayers together. However the results of Tanaka et al.[19] for GaN templates on SiC, published after these studies were completed, were obtained without InGaN layers.

3.2.3 GaN templates on SiC substrate

Standard GaN templates on SiC substrate at UCSB utilize an AlN nucleation layer grown at reduced temperature. XRD, AFM and TEM studies have revealed that the resulting templates have a lower mixed character TDD compared to the standard GaN templates on sapphire, but a high edge-type TDD, comparable to or greater than on sapphire. (On sapphire there are very few pure screw TD's but both the mixed and edge TDD's are high and are comparable in magnitude[5].) The cross-sectional TEM micrographs in Figure 3.7, of GaN grown on SiC, demonstrate this.

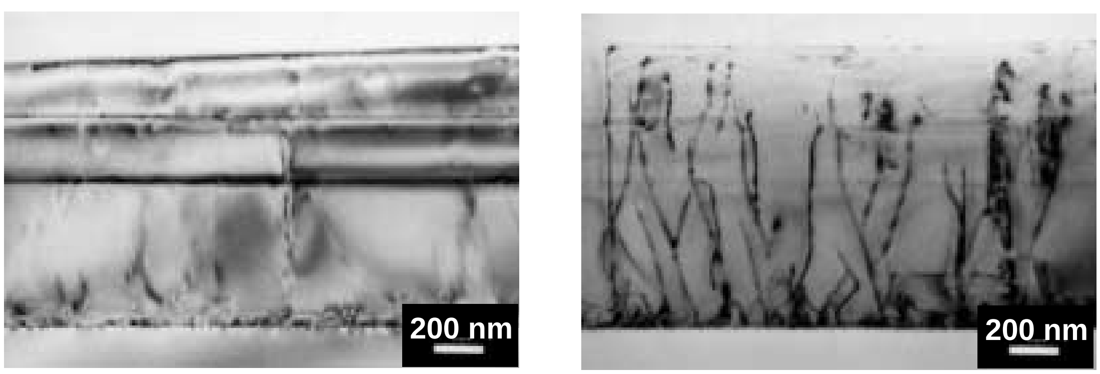

Figure 3.7 Cross-section (bright field) TEM micrograph of GaN on SiC with AlN nucleation layer. a) g = 0002, b) g = $11\bar{2}0$. (Note that there was also a laser structure deposited on top of the 2μm template for this particular wafer.)

In Figure 3.7a, g=0002 and only mixed and screw TD's will be visible. In figure 3.7b, g=$11\bar{2}0$ and only mixed and edge TD's will be visible. It is therefore obvious from the significantly higher number of TD's visible in Figure 3.7b that the edge-type TDD is high but the mixed character TDD is low.

The GaN template on SiC used in the photodetector study to be described below was grown under similar conditions to the template shown in Figure 3.7. It had a 750Å low temperature AlN nucleation layer, followed by a 750Å grade to GaN and then the high-temperature GaN epitaxial layer.

3.2.4 TDD comparison (by XRD) for the template study

Figure 3.8 compares the FWHM (shown here in units of arc-seconds) of the on- and off-axis diffraction peaks for four of the five wafers used in this study. These measurements were made after these wafers had identical GaN p-i-n structures deposited on each of them. The peak widths are plotted against the inclination angle during the XRD measurement, with extrapolation to an angle of 90° to indicate the pure edge component of the TDD. The FWHM for the LEO GaN template is not shown, as the diffraction peaks in that case were broadened by tilt in the underlying wings and not indicative of the true (low) TDD. The wafer indicated as "highly dislocated" was a template that was not grown under fully optimized conditions, and had a higher TDD than usual.

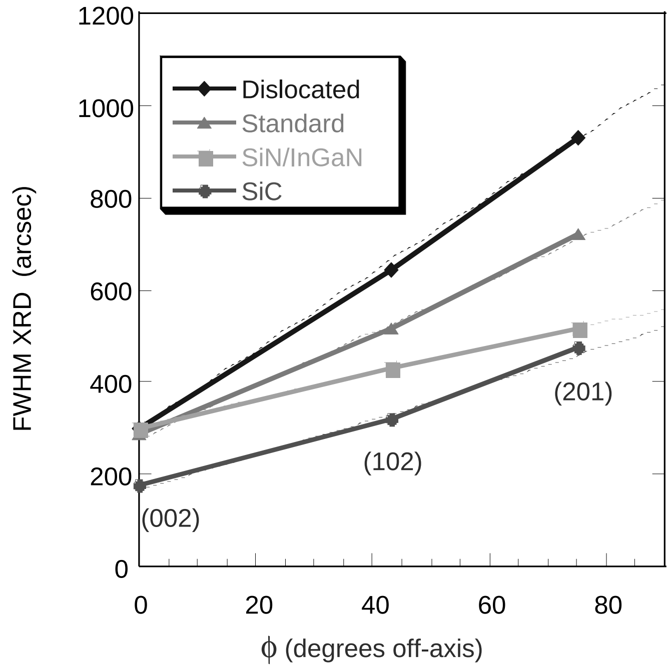

Figure 3.8 FWHM of XRD peaks with increasing measurement inclination angle, ϕ, for templates used in dislocation study.

It can be seen from the on-axis peak widths that the three wafers on sapphire all have comparable densities of TD's with a screw component (mixed character TD's). However the decrease in off-axis widths going from the worst (highly dislocated) wafer to the best (with interlayers) wafer indicates the corresponding decrease in edge-type TDD's (although it may be misleading in the case of the wafer with interlayers, as discussed in 3.2.2). The subgrain mosaic model, although shown by Srikant et al.[47] to be valid for GaN templates on sapphire, probably does not apply to GaN templates grown on SiC substrate, and the low off-axis FWHM values seen here most likely belie the true edge-type TDD. TEM of similar templates revealed a significantly lower density of mixed character TDD but a comparable edge-type TDD to the standard templates on sapphire.

3.2.5 Leakage current and threading dislocations

The photodetector structure deposited on the five templates is indicated in Figure 3.9 – the p-i-n structure had an intrinsic layer thickness of 0.8μm. The device size was 300μm x 300μm. The diodes on the LEO template comprised many seed, wing and coalesced regions, because the LEO pattern used was only 5μm and 15μm for the opening and mask stripe widths, respectively. Therefore the reduction in TDD was for 75% of the active area (with a slight decrease for the other 25% due to the very thick GaN on top of the seed regions).

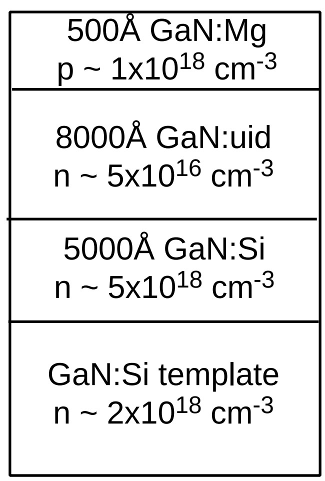

Figure 3.9 Schematic of p-i-n structure for dislocation study

The results of leakage current measurements are shown in Figure 3.10, with typical results represented for each template base. As discussed in 3.1.5, traps associated with dislocations are expected to contribute to thermal current generation through generation and tunneling, which will have a power-law and exponential dependence on voltage, respectively. It can be seen that the devices on LEO have the lowest leakage current, due to the overall reduction in dislocations and therefore of the associated traps, as Kozodoy et al. had previously demonstrated for p-n diodes[35]. The current for the devices on SiC is nearly as low. Therefore reduction of mixed character TDD is more important that reduction of the pure edge TDD. This is in agreement with the recent results of Pernot et al.[40,42] discussed earlier in this chapter, and also correlates with the experiments by Brazel et al.[13], which revealed the presence of localized traps in the vicinity of dislocations with a screw component but not in the vicinity of pure edge dislocations. They did not rule out the presence of traps near pure edge dislocations, but if they were present they were either much lower in density or higher in activation energy. The leakage current for both the LEO and SiC wafers is exponentially varying with voltage, and is most likely due to tunneling. At higher bias this will eventually lead to device breakdown.

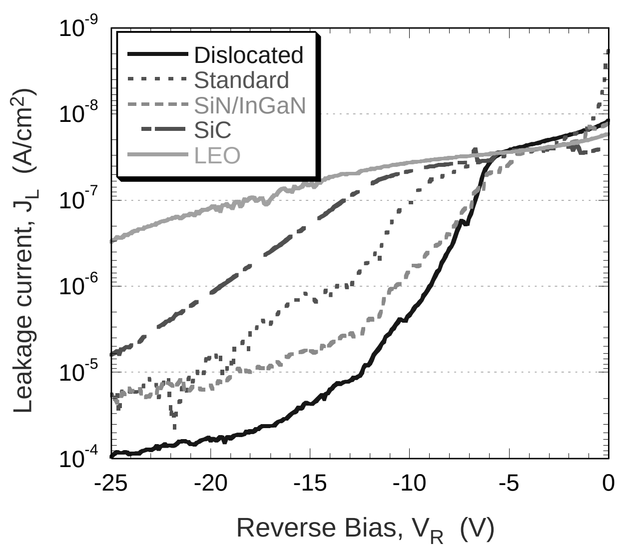

Figure 3.10 Typical reverse bias behavior (leakage current densities) for diodes on each of the different templates.

The smaller influence of edge-type TD's is also indicated by comparison of the leakage currents for the devices on the SiN/InGaN-interlayer, standard, and highly dislocated template bases. There was some variation between devices within each wafer, but in general the devices on the highly dislocated devices had the highest leakage current, while the devices on the SiN/InGaN interlayer template had at best the same leakage current as those on the standard template, and on average slightly worse. It is apparent that at very high densities the presence edge-type TD's (dislocated wafer) do contribute significantly to leakage current, and reduction to the moderately high TDD in the standard wafer results in an improvement. However, further reduction of edge-type TDD beyond these levels (SiN/InGaN wafer) has little or no effect, once again indicating there is less trap-assisted current associated with the edge-type TD's. However, it may also be an indication that the XRD measurements were indeed misleading regarding the occurrence of TDD reduction using the SiN/InGaN interlayers.

Another feature to note is the uneven behavior exhibited by devices from those three wafers on GaN/sapphire templates. Some (although not all) devices from each of these wafers produced this behavior, where the leakage current increases sharply, and then saturates again. Contrast between the low field and the high field behavior has been observed by others for GaN p-n junctions. Kuksenkov et al. attributed the behavior they witnessed at lower fields to carrier hopping between traps[49]. Sampath et al. attributed an initial steep increase in leakage current to a detrapping of donor levels, which were all emptied at larger reverse bias[50]. This may be the situation here, with donor levels associated with the mixed character TD's present in the diodes on sapphire. The region of sharp increase is not exponentially dependent on the bias voltage, but instead exhibits a power dependence $J \sim V^b$, where $b \approx 5\text{-}6$ (fit not shown). Therefore it is not tunneling causing the sharp increase in leakage, and instead it is probably generation from or via traps. At higher fields this effect saturates and the dominant mechanism becomes tunneling, with an exponential dependence on voltage that is much less steep.

3.2.6 Spectral response and threading dislocations

The effect of the different dislocation contents on spectral characteristics was also assessed. Figure 3.11 contains responsivity curves, again for representative devices from each wafer. Here it can be seen that the changes in dislocation densities and character do not affect the strength of the response above bandgap, with peak responsivities of about 0.20A/W at 360nm. The peak responsivity for the device on the SiC substrate is red-shifted by 2nm compared to the other devices, congruent with a slight compression of the GaN epitaxial layer.

There are some differences in the cutoff, however they are marginal and difficult to differentiate when inspecting the curves. Instead, in the inset, the sharpness of the cutoff for each device is represented as the spectral range in which the response drops by three orders of magnitude from the peak value. Many devices were tested from each wafer. Although there was some distribution in measured cutoff sharpness within each wafer, the average values for each wafer confirm the trends shown in the inset.

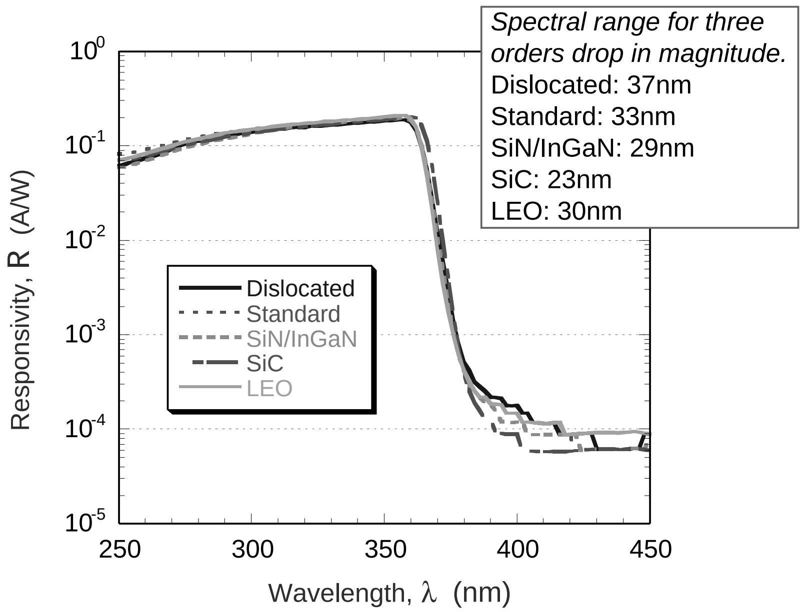

Figure 3.11 Typical spectral response for diodes on each of the different templates. Values given to the right of the plot represent sharpness of cutoff as spectral range in which the responsivity falls by three orders of magnitude from the peak.

Examination of these values reveals that with the exception of the LEO wafer, the cutoff becomes sharper as the TDD is decreased, particularly in the case of the SiC substrate, which mainly has pure edge dislocations. The results for the LEO wafer are in contrast to these results. This is probably due to impurity contributions from the SiO_2 mask in the LEO process. Contrary to most other reported results of when TDD is reduced, Sampath et al.[50] recently reported a similar phenomenon to that seen here, with a degradation in cutoff sharpness for GaN Schottky barrier detectors when grown on an HVPE substrate (whereas leakage current was reduced), which they attributed to band tail states associated with the high background carrier concentration in the HVPE GaN.

3.3 Sources of leakage current in the case of reduced TDD

With threading dislocations confirmed as a major contributor to the leakage current in the p-i-n diodes, we further investigated the source of the remaining leakage current in the absence of threading dislocations. To that end a series of GaN p-i-n diodes was deposited on LEO wafers. For this series, the thickness of the i-layer was varied from 1300Å to 1 μm.

3.3.1 High-quality coalescence of LEO

For these wafers, an improved LEO growth technique was used. Fini et al[51] had developed a two-step technique for LEO coalescence to minimize tilt in the wings, which consequently reduced the formation of dislocations at the coalescence boundary. Furthermore, wafers grown by this technique also exhibited a low TDD above the mask window, presumably due to the thickness of the GaN.

3.3.2 Leakage current and intrinsic layer thickness

In this study, GaN p-i-n diodes were deposited and fabricated in essentially the same manner as for the previous study involving different templates. Three wafers were grown, with intrinsic layer thickness of 1000Å, 5000Å and 10,000Å (the thickness varied across the wafer area – actual thickness in the area in which the diodes were measured has been taken into account in analysis of the results). In order to also establish any perimeter or volume dependence of the leakage current, three diode sizes were used: 300µm x 300µm, 150µm x 600µm, and 500µm x 500µm.

Figure 3.12 compares the leakage currents for 300µm x 300µm devices from each wafer. In order to make a valid comparison, the current is plotted as a function of electric field in the depletion region. It can be seen here that the leakage current becomes worse at a given field for larger values of t_i. This trend indicates that traps due to defects in the i-layer are the cause of the leakage current in the absence of threading dislocations. The intrinsic layer is formed by compensation of the unintentional n-type doping. This is achieved by growing the GaN under those conditions that favor increased impurity incorporation. Consequently it is a straightforward conclusion that the traps causing leakage current in the absence of a large TDD are associated with point defects.

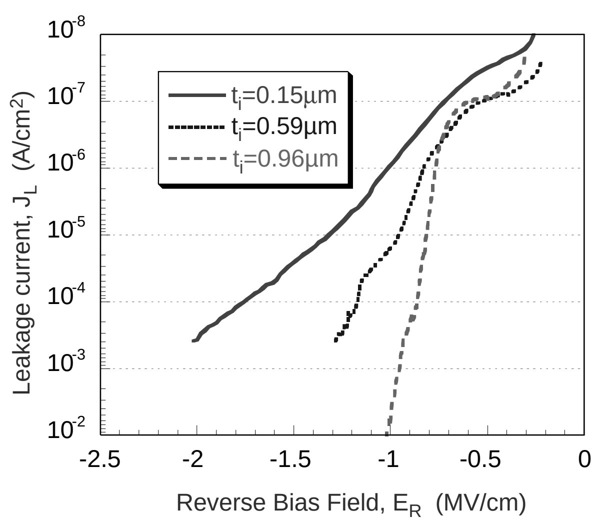

Figure 3.12 Leakage current density plotted against the reverse applied field for GaN p-i-n diodes with different intrinsic layer thickness, t_i.

3.3.3 Leakage current and diode sidewalls

Figure 3.13 presents the leakage current density for three diode sizes (the diodes were side-by-side on the wafer) from the wafer with t_i=5900Å. It is obvious that the perimeter-to-area ratio does not affect the current density, and hence there is no significant sidewall contribution. This was true for diodes measured on the other wafers as well.

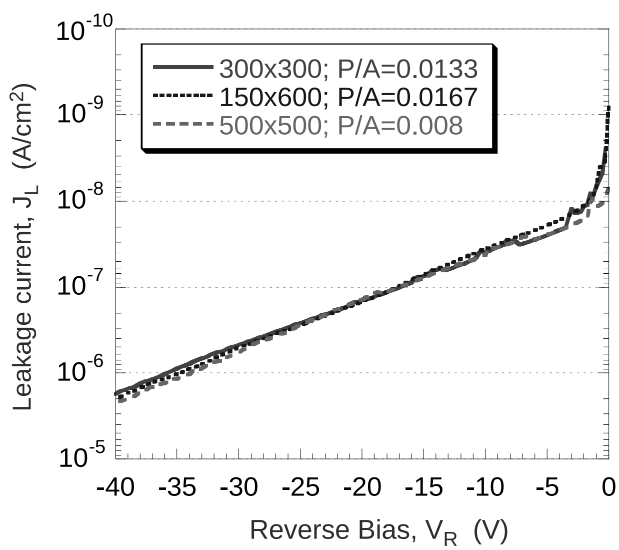

Figure 3.13 Leakage current density for three different diode sizes (and perimeter-to-area P/A) for GaN p-i-n diodes with t_i = 6000Å.

All of these devices had SiO_2 deposited on the sidewalls prior to contact pad deposition. Therefore, to further clarify this result, diodes were fabricated on a similar diode structure (though on a regular GaN/sapphire template and not on LEO GaN), half of which had sidewall passivation with SiO_2 and half of which did not. Leakage current for the best of these devices is shown in figure 3.14. The best devices without SiO_2 are as good as the best devices with SiO_2. It is apparent that even in the presence of a high dislocation density (without LEO template) the sidewall passivation using SiO_2 does not affect the leakage current.

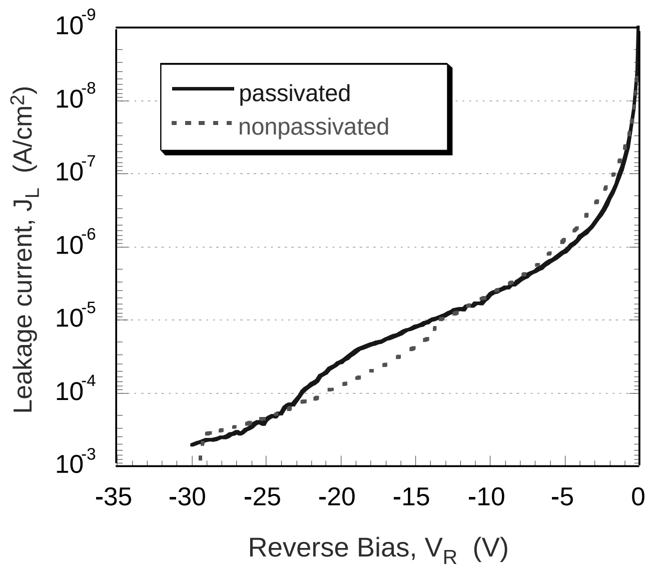

Figure 3.14 Leakage current density for 150μm x 600 μm p-i-n diodes fabricated with and without sidewall passivation by SiO_2 deposition. These were the best diodes measured. For these diodes t_i = 6000Å and a standard GaN template was used.

A further outcome of these experiments is that measurements revealed, in some cases, diodes with massive leakage in both the forward and reverse directions. The reason for why this occurred could be processing-related, possibly due to metal migration through the junction when the contacts were annealed. On some wafers few to none of the devices exhibited such behavior, on other wafers many did and many devices had to be tested to find diodes without such chronic leakage in order to obtain valid comparisons between the wafers.

3.4 TDD reduction for p-GaN/i-AlGaN/n-GaN detector

In addition to the investigations of threading dislocation effects on GaN p-i-n diodes, a separate experiment examined the effect of threading dislocations on GaN/AlGaN/GaN solar-blind p-i-n photodiodes. The diode structure was developed as a result of collaborations with Cree Lighting company (then Witech), where it had originally been conceived by Eric Tarsa and Peter Kozodoy. This structure was deposited on both an LEO GaN template and a dislocated GaN template, similar to the heavily dislocated template used in the work described previously in this chapter.

3.4.1 p-GaN/i-AlGaN/n-GaN structure

The diode structure envisaged by Cree Lighting utilized a GaN/AlGaN/GaN p-i-n structure with only a thin $Al_{0.35}Ga_{0.65}N$ active layer to avoid the thickness limitations in AlGaN growth on GaN templates[52]. As discussed in Chapter 2, high quality AlGaN grown on GaN templates had been developed at UCSB, and was preferable to the poor-quality bulk AlGaN in an all-AlGaN structure. Additionally, the use of p-GaN and n-GaN avoided difficulties in obtaining doped AlGaN of such high composition. Figure 3.15a shows a schematic of the structure. The doping in the p- and n-GaN layers was approximately the same as the GaN p-i-n structures described earlier in this chapter. A 250Å $In_{0.04}Ga_{0.96}N$ softening layer is used underneath the AlGaN to allow a thicker layer to be grown without cracking. Also, n-type $In_{0.2}Ga_{0.8}N/In_{0.04}Ga_{0.96}N$ quantum wells were place between the n-GaN and the i-AlGaN, and p-type $Al_{0.1}Ga_{0.9}N$/GaN quantum wells between the i-AlGaN and the p-GaN, all with carrier concentrations of approximately 1×10^{18} cm^{-3}.

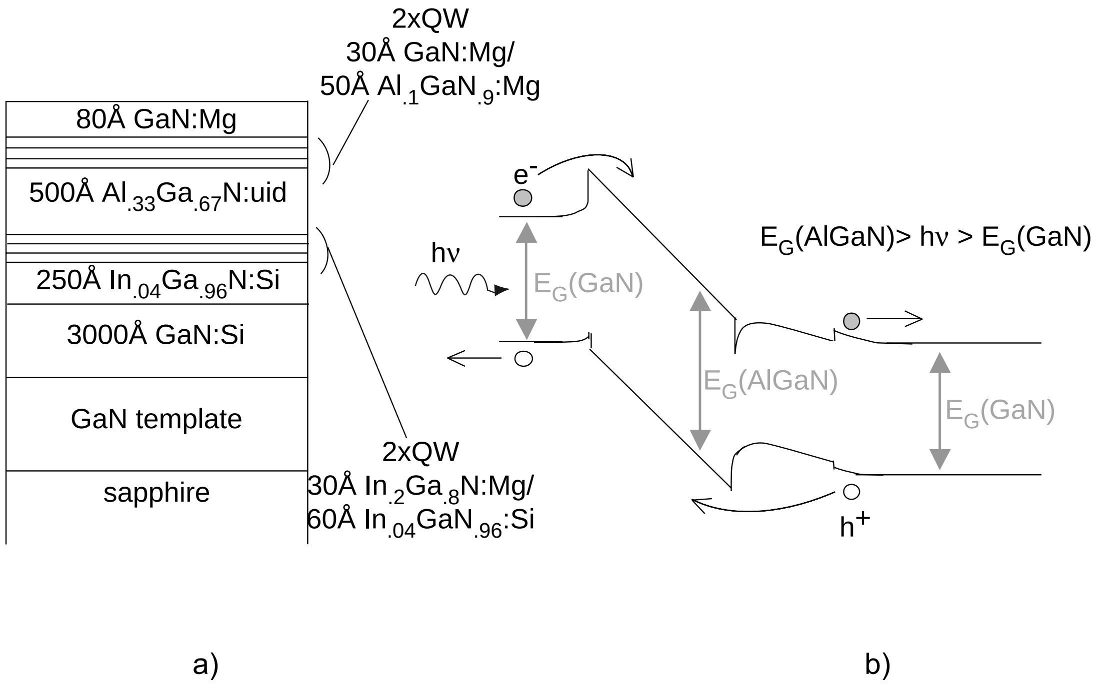

Figure 3.15 p-GaN/i-AlGaN/n-GaN solar-blind detector. a) Schematic of device structure. b) Band diagram (not to scale) of structure in the absence of the quantum well barrier layers, indicating potential for photogenerated electrons and holes from GaN regions to reach AlGaN and contribute to photocurrent.

In Figure 3.15b the band diagram is indicated for such a structure but without the quantum wells. The barrier between the AlGaN and the p- and n- (In)GaN layers is very important. Figure 3.15b indicates how photogenerated holes in the n-GaN and electrons in the p-GaN could surmount ΔE_v and ΔE_c, respectively, between the GaN and AlGaN. Thus for impinging light with E_G(AlGaN)>hν>E_G(GaN) there may be photocurrent due to these which detracts from solar-blind cutoff properties of the AlGaN i-layer. Fortunately, the polarization in GaN/AlGaN/GaN structures grown by

MOCVD on sapphire augments the barrier provided by the energy gap discontinuities. As discussed in relation to AlGaN/GaN HEMTs in the introductory chapter, the polarization induces a large electric field at the AlGaN/GaN interface for AlGaN layers on GaN/sapphire grown by MOCVD. Similarly there will be polarization charge at the upper GaN/AlGaN interface resulting in a large field of the opposite sign at that interface. These fields result in an enhancement of the barriers to minority carriers from the p- and n- regions. The quantum wells provide an additional high-recombination region to further prevent unwanted carrier movement. Simulations by Pulfrey et al.[53] confirmed the beneficial effect of the quantum wells.

3.4.2 TDD study

The photodetector p-i-n structures were deposited by MOCVD on the LEO and dislocated GaN templates, which had been previously grown. XRD measurements revealed the composition of the AlGaN layer to be 33% Al. On the LEO GaN wafer, 10μm x 1000μm mesas were defined so that the active area was entirely contained within the LEO wings. For comparison, 30μm x 1000μm mesas were defined, that additionally spanned the coalesced region between two wings. For both of these diode layouts the active area did not incorporate any of the dislocated seed regions. A photograph of the finished diodes, showing alignment with the underlying LEO pattern, is given in Figure 3.16. Square 300μm x 300μm mesas were defined on the dislocated GaN wafer. In this experiment there was sidewall passivation and large pad deposition only for the devices on LEO, and there was no thin Pd layer on any of the devices.

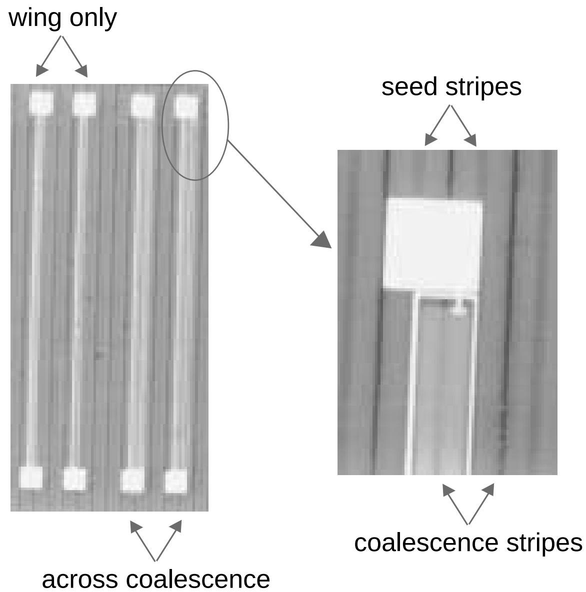

Figure 3.16 Diodes on LEO GaN template after completion of processing. The LEO pattern is visible under the diodes, which were fabricated both on the wing-only regions and spanning the coalescence region.

3.4.3 Leakage current and threading dislocations

Again, reverse-bias current measurements showed that dislocation reduction resulted in a reduction in leakage current. Leakage currents for the various types of diode are plotted in Figure 3.17. The diodes fabricated on the wing region only of the LEO GaN exhibit extremely low current densities of 10 nA/cm^2 at a reverse bias of –5V. At that bias the diodes with the active area encompassing the coalescence region had a leakage current density of 100 nA/cm^2, an order of magnitude higher.

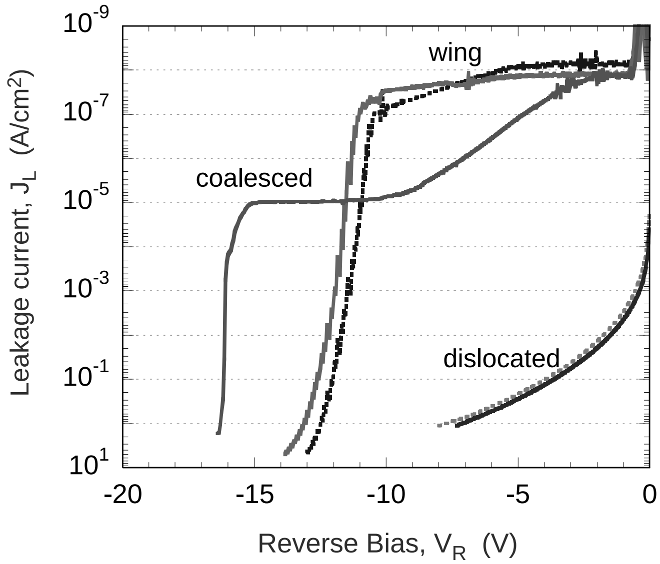

Figure 3.17 Typical leakage current densities for diodes fabricated on the wing region only of LEO GaN, the wing region plus coalesced area of LEO GaN, and dislocated GaN.

These LEO templates were not grown using the low-tilt, smooth-coalescence technique, and microscopic images (secondary electron microscopy and atomic force microscopy) of the as-grown structures had showed voids below the surface and a defective surface structure along the coalescence edges. The AFM voltage amplitude scan in Figure 3.18 gives a surface view of the coalescence boundary and the disrupted morphology in that area. Additionally, for the coalesced region diodes, the reverse bias behavior is similar to that observed earlier for the GaN p-i-n diodes on dislocated GaN templates, with a steep increase in leakage current which saturates and is followed by a more gradual increase in leakage current. Given that the presence of threading dislocations at the coalescence front had been confirmed with AFM images, this is obviously the same mechanism as before, with leakage current due to generation from or via traps.

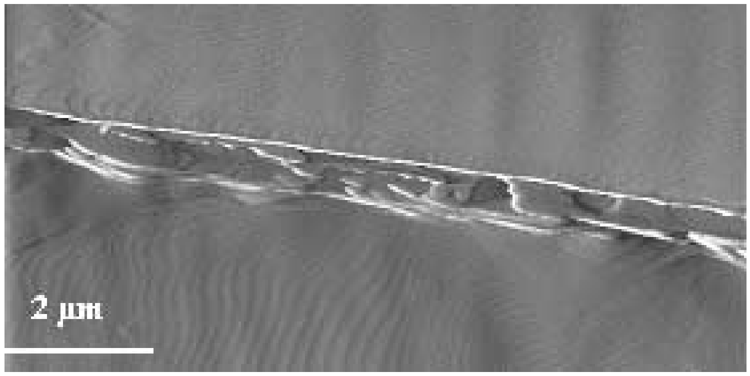

Figure 3.18 AFM (voltage amplitude) image along coalescence boundary of LEO GaN. Greyscale =0.5 V.

The current density of the diodes fabricated on the dislocated GaN was over six orders of magnitude higher again, at 300 mA/cm^2. For all of the diodes on the dislocated wafer, in fact, the forward characteristics also showed heavy leakage. This, coupled with the soft breakdown in reverse bias, attests to the presence of a large leakage path. These diodes had much worse leakage than the GaN p-i-n diodes on the dislocated template observed earlier in this chapter, resulting in a much more dramatic contrast for leakage current with and without threading dislocations. While this severe leakage path may be due to the dislocation-induced enhanced defect formation in AlGaN seen in Chapter 2, it is more likely that, as discussed earlier, it was processing-related.

3.4.4 Spectral response and threading dislocations

The responsivity curves further emphasize the effect of the dislocation structure on the performance of the photodiodes. The best spectral response curves for the different diodes are plotted in Figure 3.19.

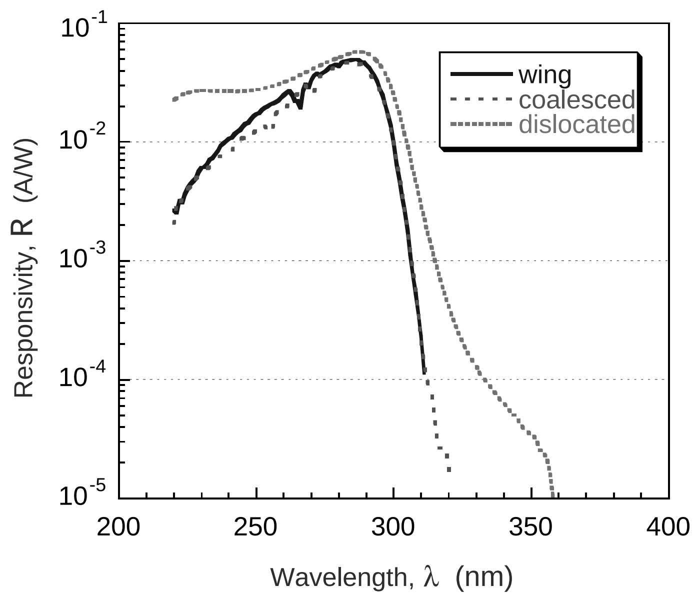

Figure 3.19 Spectral response curves for diodes fabricated on the wing region only of LEO GaN, the wing region plus coalesced area of LEO GaN, and dislocated GaN

The responses for the diodes fabricated on the LEO GaN (both wing-only and coalesced) rise almost linearly with wavelength prior to the peak. The peak responsivities are 0.050 A/W at 286 nm, and 0.047 A/W at 285 nm, for the wing-only and coalesced-region diodes, respectively. (The slight variations in absolute value of responsivity are due to thickness variations across the wafer area.) The responsivities then drop three orders of magnitude over 26 nm and 30 nm, respectively. Beyond that the photocurrent levels were below the detection limits of the experimental setup.

Although the peak responsivity of the diode on the dislocated GaN (0.057 A/W at 287 nm) is comparable to that of the LEO-diodes, the curve itself is significantly different. Firstly, the cutoff is broader – the responsivity takes 54 nm to drop by three orders of magnitude after the peak. Again this can be explained by drawing on the higher dislocation density in these diodes. Beyond the peak wavelength, the incident UV light is not absorbed in the active region, however it will still be absorbed in the p- and n-GaN layers due to the lower bandgap energy. At long wavelengths and due to the thinness of the p-GaN this will mostly occur in the n-GaN below the active region. Recalling the diode structure in Figure 3.15, the generated holes should not contribute to the photocurrent if the valence band discontinuity and quantum wells between the n-InGaN and the $Al_{.33}Ga_{.67}N$ prevent their reaching the high-field region. However for the dislocated GaN, leakage paths through to the depletion region result in photocurrent from these minority holes generated below. This emerges as a significant spectral response for wavelengths above cutoff. This leakage may result from hopping conduction between localized traps associated with the dislocations. Alternatively, the local perturbations in charge around threading dislocations, particularly at the interface, may result in deformation of the band structure, thus lowering the potential barrier and allowing the carriers to reach the depletion region.

The second difference in the spectral response is that the responsivity for wavelengths below 250 nm is higher for diodes on the dislocated wafer. At these short wavelengths most of the absorption will be in the p-GaN (the absorption length in GaN at 250nm is approximately 400Å[54]). Again, photogenerated electrons from the p-GaN will usually be prevented from entering the depletion region by the quantum wells and the conduction band discontinuity between the p-GaN and the $Al_{0.33}Ga_{0.67}N$ on the LEO wafer. However leakage paths in the dislocated wafer allow these photogenerated electrons from the p-GaN to reach the high-field region, resulting in a significant enhancement of the photoresponse. This effect disappears at longer wavelengths, for which a much smaller proportion of the input light is absorbed in the thin p-GaN.

Further contributions to the sub-bandgap response may include band-tail states resulting from traps and alloy clustering occurring in the dislocated structure and not in the LEO structure. It was shown in the previous chapter that the threading dislocations in GaN themselves enhance defect formation in AlGaN layers. The AFM image in Figure 3.20 shows the p-GaN surface a) on LEO and b) on dislocated GaN template, with many pits corresponding to TD's visible for the latter and none visible for the former, and c) the underlying AlGaN (prior to p-GaN cap) on dislocated GaN template showing the defect structure witnessed in Chapter 2 in the presence of TD's. This is in agreement with the results of others discussed earlier in this chapter, in which photodiodes with a large TDD exhibited degraded spectral characteristics as x_{Al} was increased. Note that these structural defects (due to the high x_{Al}) and the broadened pits (due to the InGaN softening layer) in Figure 3.20c have been filled in by the p-GaN in Figure 3.20b, so that the smaller dislocation pits on the p-GaN surface belie the size and quantity of the defects in the underlying AlGaN layer.

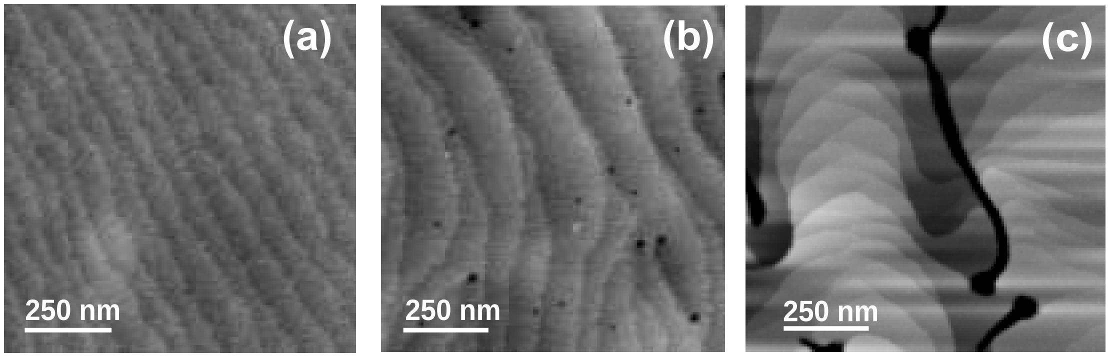

Figure 3.20 AFM images of p-i-n diode: a) p-GaN surface for LEO GaN template, b) p-GaN surface for dislocated GaN template, and c) the underlying i-AlGaN (prior to p-GaN cap) on dislocated template. The large size of the pits in c) is most likely due to the underlying InGaN softening layer.

3.4.5 Pulsed response and threading dislocations

For these devices, response time measurements were made by the use of a HP Infinium 500MHz oscilloscope to measure photocurrent under illumination from a pulsed and frequency-tripled Ti/sapphire laser. The impulse response of the detectors was measured at 263nm. The 90%-10% fall times were extracted from the resulting pulses. The devices fabricated on the LEO wing region were very fast, with fall times of 4.5-6.5ns. The devices which spanned the coalescence region had slightly slower times of 12.9ns or higher, while the devices on dislocated GaN exhibited times of at best 30ns. These times scale approximately with the areas of the three different device types, indicating RC-limited responses. Figure 3.21 shows typical pulses resulting from these measurements.

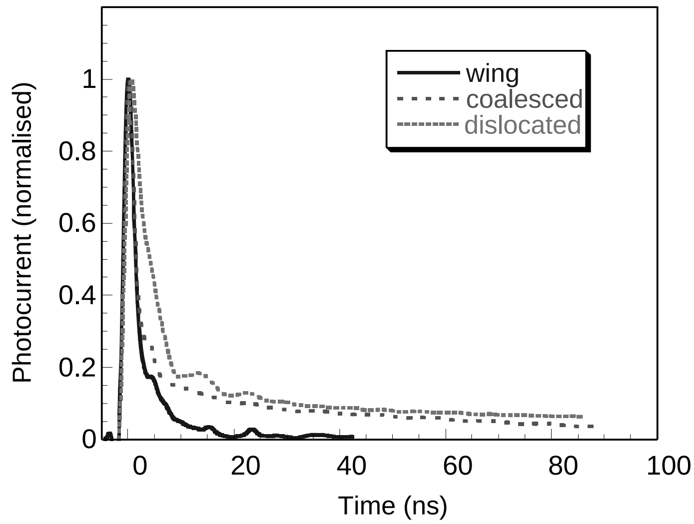

Figure 3.21 Pulsed response at 263 nm for diodes fabricated on the wing region only of LEO GaN, the wing region plus coalesced area of LEO GaN, and dislocated GaN.

A key feature is the long slow "tail" component evident for the coalesced and dislocated devices. In comparison, the pulse for the wing devices has no visible tail and quickly falls to zero current. The dislocation reduction through use of LEO therefore improves device speed by elimination of this effect. This is elucidated in Figure 3.22, which presents the pulsed response for a) the diode on LEO wing and b) the diode on dislocated template, fitted as a sum of two exponentials. The slow tail component of the dislocated device has an exponential decay time of 87.4ns, compared to only 8.8ns for the LEO device. Although not as devastating as that present in GaN photoconductors, there is still some mechanism slowing photodiode response in the presence of a large TDD.

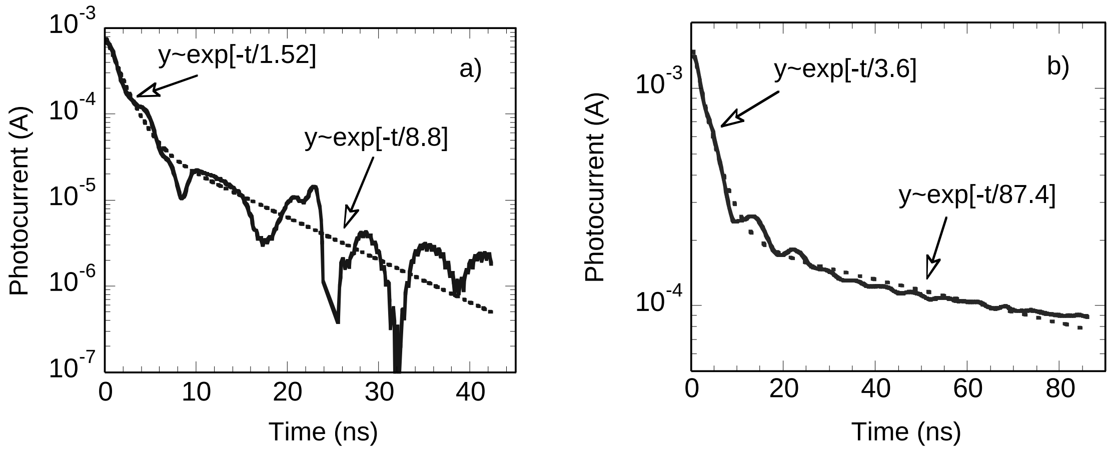

Figure 3.22 Pulsed response at 263 nm for diodes fabricated on a) LEO GaN (wing region only) and b) dislocated GaN, fitted with a sum of two exponentials.

3.5 Conclusions

Tunneling and generation via traps associated with mixed character threading dislocations significantly contributes to leakage current in GaN-based diodes. Edge-type dislocations have less effect, although at very high densities they also contribute to leakage current. In the absence of a large TDD, there is still significant leakage, but it is not due to sidewalls. Leakage paths associated with threading dislocations also contribute to broadening of the spectral cutoff in photodiodes, and to a slow tail in pulsed response, which increases the response time. For p-GaN/i-AlGaN/n-GaN diodes trap levels due to threading dislocations provide a conduction path through or over the heterojunction barrier, so that absorption in the p-GaN and/or the n-GaN contributes to spectral response.

3.6 References

1. D. Hull. *Introduction to Dislocations* (1965), Pergamon Press, Oxford

2. H. Amano, N. Sawaki, I. Akasaki, and Y. Toyoda, "Metalorganic vapor phase epitaxial growth of a high quality GaN film using an AlN buffer layer." *Appl. Phys. Lett*. **48**, 353-355 (1986).

3. B.P. Keller, S. Keller, D. Kapolnek, W.-N. Jiang, Y.-F. Wu, H. Masui, X.H. Wu, B. Heying, J.S. Speck, U.K. Mishra, and S.P. DenBaars, "Metalorganic chemical vapor deposition growth of high optical quality and high mobility GaN." *J. Electron. Mater.* **24,** 1707-1709 (1995).

4. S. Keller, D. Kapolnek, B.P. Keller, Y.-F. Wu, B. Heying, J.S. Speck, U.K. Mishra, and S.P. DenBaars, "Effect of the trimethylgallium flow during nucleation layer growth on the properties of GaN grown on sapphire." *Jpn. J. Appl. Phys.* **35,** L285-288 (1996).

5. X.H. Wu, P. Fini, E.J. Tarsa, B. Heying, S. Keller, U.K. Mishra, S.P. DenBaars, and J.S. Speck, "Dislocation generation in GaN heteroepitaxy." *J. Cryst. Growth* **189/190,** 231-243 (1998).

6. K. Dovidenko, S. Oktyabrsky, J. Narayan, V. Joshkin and M. Razeghi, "Comparative study of typical defects in III-nitride thin films and their alloys." *Mat. Res. Soc. Symp. Proc.* **482**, 411-416 (1998).

7. T. Hashimoto, M. Yuri, M. Ishida, Y. Terakoshi, O. Imafuji, T. Sugino, and K. Itoh, "Reduction of threading dislocation in GaN on sapphire by buffer layer annealing in low-pressure metalorganic chemical vapor deposition." *Jpn. J. Appl. Phys.* **38,** 6605-6610 (1996).

8. H. Lahrèche, M. Leroux, M. Laügt, M. Vaille, B. Beaumont, and P. Gibart, "Buffer free growth of GaN on 6H-SiC by metalorganic vapor phase epitaxy." *J. Appl.Phys.* **87,** 577-583 (2000).

9. P. Waltereit, O. Brandt, A. Trampert, M. Ramsteiner, M. Reiche, M. Qi, and K.H. Ploog, "Influence of AlN nucleation layers on growth mode and strain relief of GaN grown on 6H-SiC(0001)." *Appl. Phys. Lett.* **74,** 3660-3662 (1999).

10. M.D. Bremser, W.G. Perry, T. Zhevela, N.V. Edwards, O.H. Nam, N. Parikh, D.E. Aspnes, and Robert F. Davis, "Growth, doping and characterization of $Al_xGa_{1-x}N$ thin film alloys on 6H-SiC(0001) substrates." *MRS Internet J. Nitride Semicond. Res.* **1,** 8 (1996).

11. A. Kuramato (Fujitsu Laboratories), "Blue lasers on SiC substrate.", UCSB Seminar, Santa Barbara December 2000.

12. P. J. Hansen, Y.E. Strausser, A.N. Erickson, E.J. Tarsa, P. Kozodoy, E.G. Brazel, J.P. Ibbetson, U. Mishra, V. Narayanamurti, S.P. DenBaars, and J.S. Speck, "Scanning capacitance microscopy imaging of threading dislocations in GaN films grown on (0001) sapphire by metalorganic chemical vapor deposition." *Appl. Phys. Lett.* **72,** 2247-2249 (1998).

13. E.G. Brazel, M.A. Chin, and V. Narayanamurti, "Direct observation of localized high current densities in GaN films." *Appl. Phys. Lett*. **74,** 2367-2369 (1999).

14. A.E. Wickenden, D.D. Koleske, R.L. Henry, R.J. Gorman, M.E. Twigg, M. Fatemi, J.A. Freitas Jr., and W.J. Moore, "The influence of OMVPE Growth Pressure on the morphology, Compensation and Doping of GaN and Related Alloys." *J. Electron. Mater.***29,** 21-26 (2000).

15. C. Shi, P.M. Asbeck, and E.T. Yu, "Piezoelectric polarization associated with dislocations in wurtzite GaN." *Appl. Phys. Lett*. **74,** 573-575 (1999).

16. S. Haffouz, H. Lahrèche, P. Vennéguès, P. de Mierry, B. Beaumont, F. Omnès, and P. Gibart, "The effect of the Si/N treatment of a nitridated sapphire surface on the growth mode of GaN in low-pressure metalorganic vapor phase epitaxy." *Appl. Phys. Lett.* **73,** 1278-1280 (1998).

17. H. Lahrèche P. Vennégués, B. Beaumont, and P. Gibart, “Growth of high-quality GaN by low-pressure metal-organic vapour phase epitaxy (LP-MOVPE) from 3D islands and lateral overgrowth.” *J. Cryst. Growth* **205,** 245-252 (1999).

18. T. Wang, Y. Morishima, N. Naoi, and S. Sakai, “A new method for a great reduction of dislocation density in GaN layer grown on a sapphire substrate.” *J. Cryst. Growth* **213,** 188-192 (2000).

19. S. Tanaka, M. Takeuchi, and Y. Aoyagi, “Anti-surfactant in III-nitride epitaxy – quantum dot formation and dislocation termination-.” *Jpn. J. Appl. Phys.* **39,** 831-834 (2000).

20. S. Keller, G. Parish, J.S. Speck, S.P. DenBaars and U.K. Mishra, "Dislocation reduction in GaN films through selective island growth of InGaN." *Appl. Phys. Lett.*, **77**(17), 2665-7 (2000). *J. Appl. Phys* **87**(8) 3900-4 (2000)

21. H. Amano, M. Iwaya, N. Hayashi, T. Kashima, S. Nitta, C. Wetzel, and I. Akasaki, “Control of dislocations and stress in AlGaN on sapphire using a low temperature interlayer.” *Phys. Stat. Sol.* (b) **216,** 683-689 (1999).

22. P. Kung, A. Saxler, D. Walker, X. Zhang, R. Lavado, K.S. Kim, and M. Razeghi “$Al_xGa_{1-x}N$ Based Materials and Heterostructures.” *Mat. Res. Soc. Symp. Proc.* **449,** 79-84 (1997).

23. W.V Lundin, A.S. Usikov, B.V. Pushnyi, U.I. Ushakov, M.V. Stepanov, N.M. Shmidt, T.V. Shubina, A.V. Sakharov, N.N. Faleev, V.A. Solov’ev, A.A. Sitnikova, Yu.A. Kudriavtsev, B.Ya. Ber, and Y.M Zadiranov, “Optical and structural studies of thick AlGaN alloy layers and AlGaN/GaN heterostructures on sapphire substrates.” *Mat. Sci. Forum* **264-268,** 1315-1318 (1998).

24. H. Marchand, X.H. Wu, J.P. Ibbetson, P.T. Fini, P. Kozodoy, S. Keller, J.S. Speck, S.P. DenBaars, and U.K. Mishra “Microstructure of GaN laterally overgrown by metalorganic chemical vapor deposition.”*Appl. Phys. Lett.* **73**, 747 (1998).

25. T.S. Zheleva, O.-H. Nam, M.D. Bremser, and R.F. Davis, "Dislocation density reduction via lateral epitaxy in selectively grown GaN structures." *Appl. Phys. Lett.* **71,** 2472-2474 (1997).

26. D. Kapolnek, S. Keller, R. Ventury, R.D. Underwood, P. Kozodoy, S.P. DenBaars, and U.K. Mishra "Anisotropic epitaxial lateral growth in GaN selective area epitaxy." *Appl. Phys. Lett.* **71,** 1204-1206 (1997).

27. O.-H. Nam, M.D. Bremser, T.S. Zheleva, and R.F. Davis "Lateral epitaxy of low defect density GaN layers via organometallic vapor phase epitaxy." *Appl. Phys. Lett.* **71,** 2638-2640 (1997).

28. M.E. Coltrin, C.C. Willan, M.E. Bartram, J. Han, N. Missert, M.H. Crawford, and A.G. Baca ,"Transport, growth mechanisms, and material quality in GaN epitaxial lateral overgrowth." *MRS Internet J. Nitride Semicond. Res.* **4S1,** G6.9 (1999).

29. F. Binet, J.Y. Duboz, E. Rosencher, F. Scholz, and V. Hãrle, "Mechanisms of recombination in GaN photodetectors." *Appl. Phys. Lett.* **69,** 1202-1204 (1996).

30. Z.C. Huang, D.B. Mott, P.K. Shu, R. Zhang, J.C. Chen, and D.K. Wickenden "Optical quenching of photoconductivity in GaN photoconductors." *J. Appl. Phys.* **82,** 2707-2709 (1997).

31. E. Monroy, J.A. Garrido, E. Muñoz, I. Izpura, F.J. Sánchez, M.A. Sánchez-García, E. Calleja, B. Beaumont, and Pierre Gibart, "Characterization and modelling of photoconductive GaN ultraviolet detectors." *MRS Internet J. Nitride Semicond. Res.* **2,** Article 12 (1997).

32. Z.C. Huang, D.B. Mott, P.K. Shu, J.C. Chen, and D.K. Wickenden, "Improvement of metal-semiconductor-metal GaN photoconductors." *J. Electron. Mater.* **26,** 330-333 (1997).

33. G.M. Smith, J.M. Redwing, R.P. Vaudo, E.M. Ross, J.S. Flynn, and V.M. Phanse, "Substrate effects on GaN photoconductive detector performance." *Appl. Phys. Lett.* **75,** 25-27 (1999).

34. J.T. Torvik, J.I. Pankove, S. Nakamura, I. Grzegory, and S. Porowski "The effect of threading dislocations, Mg doping, and etching on the spectral responsitivity in GaN-based ultraviolet detectors." *J. Appl. Phys.* **86,** 4588-4593 (1999).

35. P. Kozodoy, J.P. Ibbetson, H. Marchand, P.T. Fini, S. Keller, J.S. Speck, S.P. DenBaars, and U.K. Mishra, "Electrical characterization of GaN *p-n* junctions with and without threading dislocations." *Appl. Phys. Lett.* **73,** 975-977 (1998).

36. G. Parish, S. Keller, P. Kozodoy, J. P. Ibbetson, H. Marchand, P. T. Fini, S.B. Fleischer, S. P. DenBaars, U. K. Mishra and E.J. Tarsa, "High-performance (Al,Ga)N-based solar-blind ultraviolet p-i-n detectors on laterally epitaxially overgrown GaN" *Appl. Phys. Lett.* **75**(2), 247-9 (1999).

37. E. Monroy, F. Calle, E. Muñoz, B. Beaumont, F. Omnès, and P. Gibart "Schottky barrier ultraviolet photodetectors on epitaxial lateral overgrown GaN." *Phys. Stat. Sol. (a)* **176,** 141-145 .(1999).

38. P. Sandvik, D. Walker, P. Kung, K. Mi, F. Shahedipour, V. Kumar, X. Zhang, J. Diaz, C. Jelen, and M. Razeghi "Solar-blind $Al_xGa_{1-x}N$ p-i-n photodetectors grown on LEO and non-LEO GaN." *Proc. SPIE* **3948,** 265-272 (2000).

39. A. Osinsky, S. Gangopadhyay, R. Gaska, B. Williams, M.A. Khan, D. Kuksenkov, and H. Temkin, "Low noise *p-π-n* ultraviolet photodetectors." *Appl. Phys. Lett.* **71,** 2334-2336 (1997).

40. C. Pernot, A. Hirano, M. Iwaya, T. Detchprohm, H. Amano, and I. Akasaki "Improvement of low-intensity ultraviolet photodetectors based on AlGaN with low threading dislocation density." *Phys. Stat. Sol. (a)* **176,** 147-151 (1999).

41. C. Pernot, A. Hirano, M. Iwaya, T. Detchprohm, H. Amano, and I. Akasaki, "Solar-Blind UV photodetectors based on GaN/AlGaN p-i-n photodiodes." *Jpn. J. Appl. Phys.* **39,** 387-389 (2000).

42. E. Monroy, M. Hamilton, D. Walker, P. Kung, F.J. Sánchez, and M. Razeghi, "High-quality visible-blind AlGaN *p-i-n* photodiodes."*Appl. Phys. Lett.* **74,** 1171-1173 (1999).

43. E. Monroy, F. Calle, J.L. Paul, F.J. Sánchez, E. Muñoz, F. Omnès, B. Beaumont, and P. Gibart "Analysis and modeling of $Al_xGa_{1-x}N$-based Schottky barrier photodiodes."*J. Appl. Phys.* **88,** 2081-2091 (2000).

44. K.L. Ashley and A.G. Milnes, "Double injection in deep-lying impurity semiconductors" *J. Appl. Phys.* 35**,** 369-374 (1964).

45. S.M. Sze, *Physics of Semiconductor Devices* (1981) John Wiley & Sons, New York.

46. B. Heying, X.H. Wu, S. Keller, Y. Li, D. Kapolnek, B.P. Keller, S.P. DenBaars, and J.S. Speck, "Role of threading dislocation structure on the X-ray diffraction peak widths in epitaxial GaN films." *Appl. Phys. Lett.* **68,** 643-645 (1996).

47. V. Srikant, J. Speck, and D. Clarke, "Mosaic structure in epitaxial films having large lattice mismatch." *J. Appl. Phys.* **82,** 4286-4295 (1997).

48. S. Keller, U.K. Mishra, S.P. DenBaars, and W. Seifert, "Spiral growth of InGaN nanoscale islands on GaN." *Jpn. J. Appl. Phys.* **37**, L431-434 (1998).

49. D.V. Kuksenkov, H. Temkin, A. Osinsky, R. Gaska, and M.A. Khan "Origin of conductivity and low-frequency noise in reverse-biased GaN *p-n* junction." *Appl. Phys. Lett.* **72,** 1365-1367 (1998).

50. A.V. Sampath, E. Iliopoulos, K. Seth, Y. Fedyunin, M. Misra, H.M. Ng, P. Lamarre, Z. Feit, and T.D. Moustakas "GaN photodiodes grown by MBE on HVPE and ELO-HVPE GaN\sapphire substrates." *Proc. SPIE* **3948,** 311-318 (2000).

51. P. Fini, L. Zhao, B. Moran, M. Hansen, H. Marchand, J.P. Ibbertson, S.P. DenBaars, U.K. Mishra, and J.S. Speck "High-quality coalescence of laterally overgrown GaN/sapphire seed layers." *Appl. Phys. Lett.* **75,** 1706-1708 (1999).

52. E. J. Tarsa, P. Kozodoy, J. Ibbetson, B. P. Keller, G. Parish, and U.K. Mishra "Solar-blind AlGaN-based inverted heterostructure photodiodes." *Appl. Phys. Lett*. **77,** 316-318 (2000).

53. D.L. Pulfrey, J.J. Kuek, M.P. Leslie, B.D. Nener, G. Parish, U.K. Mishra, P. Kozodoy and E.J. Tarsa, "High UV/solar rejection ratios in GaN/AlGaN/GaN p-i-n photodiodes." *IEEE Trans. on Electron Device.* **48**(3), 100-102 (2001).

54. G. Yu, G. Wang, H. Ishikawa, M. Umeno, T. Soga, T. Egawa, J. Watanabe, and T. Jimbo, “Optical properties of wurtzite structure GaN on sapphire around ellipsometry and the optical transmission method.” *Appl. Phys. Lett.* **70**, 3209-3211 (1997).

Chapter 4. Thick AlGaN for solar-blind detectors

4.1 Developing a solar-blind p-i-n detector structure

The knowledge gained from the experiments detailed in Chapter 2 and Chapter 3 was combined to design and grow a solar-blind p-i-n detector structure.

4.1.1 Synopsis of this chapter

The study into the effects of dislocations on the p-GaN/i-AlGaN/n-GaN solar-blind detector (Section 3.4) highlighted drawbacks in that particular structure. Firstly there was the non-solar-blind response from the GaN, which broadened the cutoff, particularly in the presence of dislocations. Secondly, the peak responsivity was limited to only 0.05A/W because the thickness of the AlGaN could not be increased without cracking. In this section, some further studies of this structure are presented, along with investigations into dislocation reduction in bulk $Al_{0.35}Ga_{0.65}N$, utilizing LEO techniques. Following that, Section 4.2 details the experiments into growth of thick $Al_{0.35}Ga_{0.65}N$ on SiC substrate. These experiments were undertaken in the hope that the benefits to detector performance, as well as the possibility of avoiding costly and time-consuming LEO, would outweigh the increase in substrate cost, when using SiC substrate. The studies included investigations into the nucleation technique and into the $Al_{0.35}Ga_{0.65}N$ growth conditions and doping, as well as attempts to reduced the high edge dislocation density by using Si_xN_y interlayers. Finally the results for the first solar-blind $Al_xGa_{1-x}N$ detectors grown on SiC substrates are presented in Section 4.3, including a comparison of devices with and without a conducting buffer.

4.1.2 GaN absorption in GaN/AlGaN/GaN p-i-n

A simple experiment was devised to determine whether the source of the longer-wavelength spectral response in the p-GaN/i-AlGaN/n-GaN photodiode was absorption in the p-GaN or in the n-GaN. Figure 4.1 replicates the schematics given in Figure 3.15, of the structure cross-section and schematic, along with an indication of the modifications made for this experiment. Two modified structures were grown, in which the GaN/AlGaN interface barrier was changed. Figure 4.1 illustrates the first of these, in which the conduction band barrier to electrons at the p-GaN/ i-$Al_{0.33}Ga_{0.67}N$ interface was enhanced. This was achieved by grading the AlGaN composition to 0.5 over the last 50Å before the p-GaN. The second modified structure (not shown) had an enhanced valence band barrier to holes at the i- $Al_{0.3}Ga_{0.67}N$ /n-InGaN interface, achieved by grading the AlGaN composition from 0.5 over the first 50Å after the n-InGaN (recall that a thin $In_{0.04}Ga_{0.96}N$ softening layer was used between the n-GaN and the AlGaN). Note that in this study the quantum wells were not included, in order to assess the full effect of the interfacial barriers on carrier transport.

Figure 4.2 compares the spectral response of typical devices for each of the two modified structures. They are designated ΔE_C and ΔE_V, for the structures with enhanced electron and hole barriers, respectively. Many devices were measured from each of the two wafers, and the trends that are seen here were true for all devices.

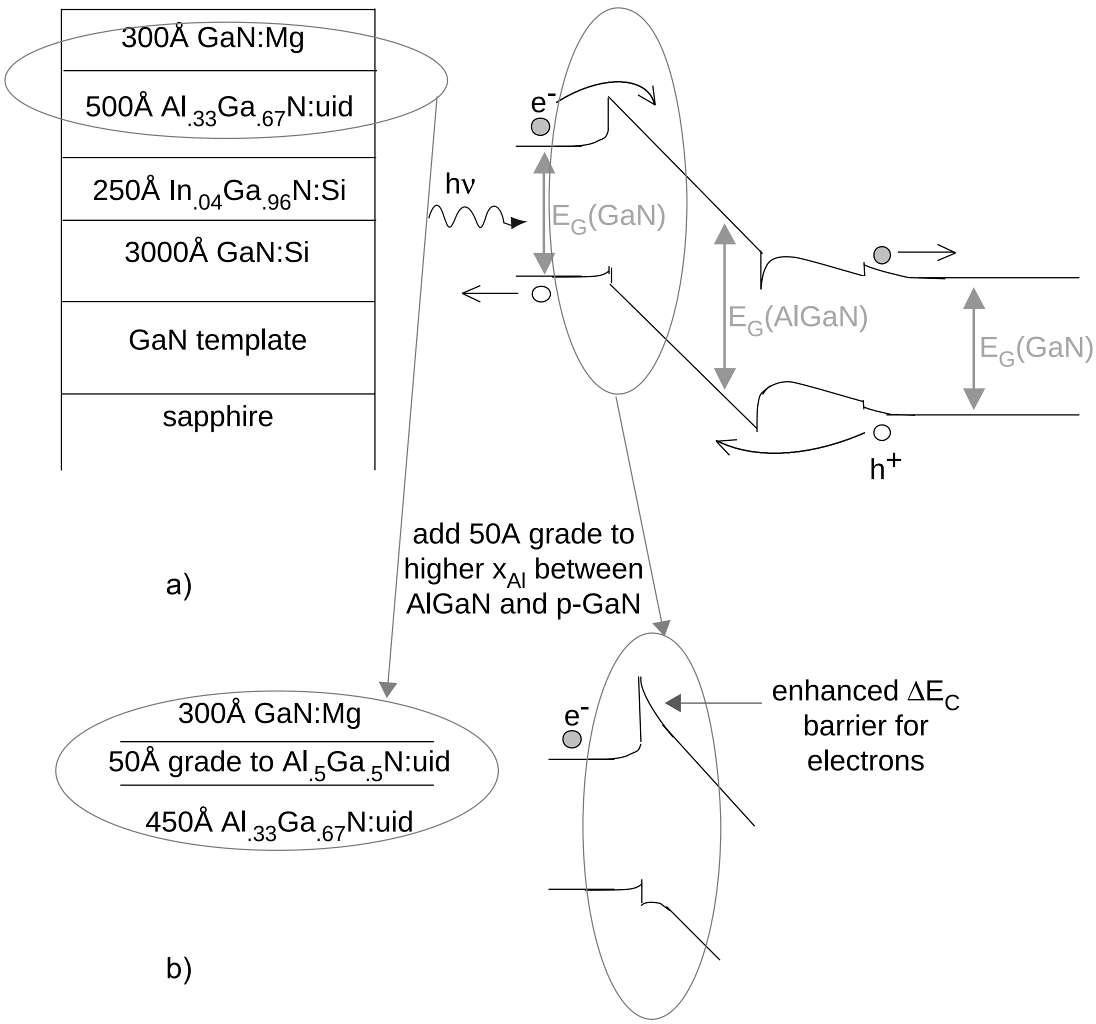

Figure 4.1 GaN/AlGaN/GaN p-i-n solar-blind detector.

a) Schematic of cross-section and band diagram (not to scale) of diode structure in the absence of the quantum well barrier layers, indicating potential for photogenerated electrons and holes from the GaN regions to reach the AlGaN and contribute to photocurrent. b) Schematic of modified AlGaN layer incorporating a grade to $Al_{0.5}Ga_{0.5}N$ to enhance electron barrier at p-GaN/i-AlGaN interface.

The first noticeable feature, for both curves in Figure 4.2, is that there is a much more significant spectral response between 300nm and 360nm than was observed for the devices in Chapter 3. Obviously the quantum wells (absent in these structures) were significantly effective in preventing photogenerated carriers in the GaN and InGaN from reaching the AlGaN depletion region. The other important characteristic in Figure 4.2 is the lower response in this region (300nm-360nm) when the height of the valence band barrier is increased (ΔE_V structure). This was true for all the devices measured. The difference is not large, because the increase in composition to 0.5 only provides a small increment in barrier height, but it is large enough to indicate that holes generated in the underlying n-GaN are the greater source of the response in the 300nm to 360nm spectral range.

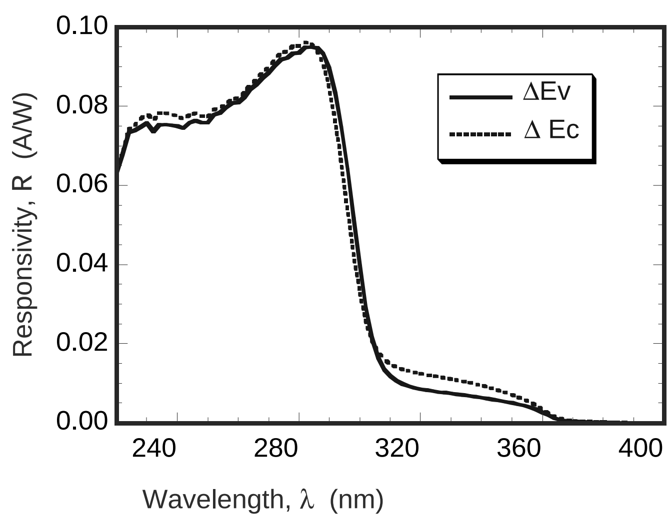

Figure 4.2 Typical spectral response of p-GaN/i-AlGaN/n-GaN photodiodes with enhanced conduction band barrier at p-GaN/ i-AlGaN interface (ΔE_C) and enhanced valence band barrier at i-AlGaN/n-GaN interface (ΔE_V).

To obtain higher responsivity, the requirements of thicker i-AlGaN necessitate growth on an AlGaN template to avoid cracking. That is, the n-layer of the p-i-n should also be AlGaN. Additionally, after now determining that the n-GaN was the main region from which undesired spectral response was originating, it is evident that the use of an n-AlGaN layer will improve the cutoff characteristics. However the p-GaN layer can be retained so as to avoid the difficulties in acquiring p-$Al_{0.35}Ga_{0.65}N$.

4.1.3 Thicker AlGaN by LEO

The investigations in Chapter 3 revealed unequivocally that threading dislocations are detrimental to multiple aspects of device performance. LEO had already proven to be a successful technique for dislocation reduction in GaN. For AlGaN it presents the additional incentive of reduced tension in the overgrown layer and therefore the possibility of growing thick AlGaN layers on GaN templates.

Reports in the literature for $Al_{0.1}Ga_{0.9}N$ had already indicated problems with selectivity of the AlGaN using conventional SiO_2 and Si_3N_4 mask materials, even at low compositions[1]. Thus, several different mask materials were tested for $Al_{0.35}Ga_{0.65}N$ selectivity. Figure 4.3 presents optical photographs of four different mask materials after regrowth, using a mask pattern with stripes oriented at 4° increments. The four mask materials compared were a) SiO_2, b) sapphire, c) Pt and d) TiN. The sapphire “mask” was obtained by etching a GaN template down to the sapphire substrate, in those areas in which SiO_2 would have been deposited for a conventional LEO mask. The TiN mask was obtained by annealing a Ti mask in N_2 ambient. Parameters such as growth temperature, growth rate, and carrier gas were varied, but with no significant effect, and so each picture is actually representative of the typical results for each mask type under all growth conditions.

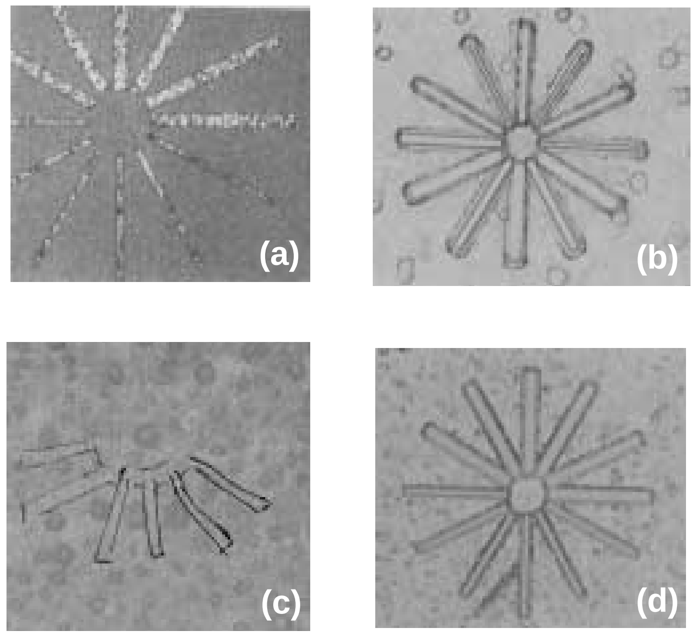

Figure 4.3 Optical photographs of attempts at LEO of AlGaN using mask material a) SiO_2, b) sapphire, c) Pt and d) TiN. In c) the original mask pattern has been indicated by a partial outline.

It can be seen that using the SiO_2 and Pt masks neither lateral growth nor selectivity were achieved. The lack of selectivity with the Pt mask was so severe that the mask pattern was barely discernable (it has been partially outlined in the figure to give an indication of the original pattern). In fact with the Pt mask, subsequent trials revealed that selectivity was not even achieved with GaN. Lateral growth from the sidewalls (visible as broadened pattern edges) was achieved using the sapphire and TiN masks, however there were large polycrystalline deposits on the mask areas as well. (GaN, though, exhibited selective regrowth using these mask materials.) For the sapphire mask, even heating to growth temperature in the absence of NH_3 (to avoid nitridation of the sapphire) did not prevent the formation of these deposits. This lack of selectivity is consistent with the high bond strength of Al to O and N and the low mobility of the Al adatoms on the surface during MOCVD, as discussed in Chapter 2.

Given that no suitable material could be found for LEO of $Al_{0.35}Ga_{0.65}N$, the next most attractive alternative (as seen from Section 3.2) was bulk growth on a SiC substrate.

4.2 AlGaN on SiC

The growth of $Al_xGa_{1-x}N$ films on SiC substrate involves a complex balance between the lattice (compressive) and thermal (tensile) mismatch, with the strain state remaining after growth strongly dependent on the nucleation conditions[2,3,4]. The technique of employing reduced nitrogen overpressure to achieve step flow growth of $Al_xGa_{1-x}N$ (learned in the earlier investigations of $Al_xGa_{1-x}N$ growth on GaN) was applied for all $Al_xGa_{1-x}N$ growth on SiC, and step flow growth was achieved. However, optimization of nucleation conditions to minimize dislocations and cracking required much more thorough investigations.

4.2.1 Experimental conditions

The growth of $Al_xGa_{1-x}N$ on SiC substrates was undertaken in a different MOCVD reactor to the previous experiments described in this thesis. In this case a vertical closed-space rotating disk reactor with a showerhead-type injection scheme was used. The precursors were the same as before. For the $Al_xGa_{1-x}N$ growth the TMGa flow was varied between 3.7 – 29 μmol/min, the TMAl flow between 4.7 – 47 μmol/min, and the ammonia flow between 0.05 – 0.13 mol/min. Variations in growth rate were achieved by changing the group III flows. The thermocouple temperature ranged from 1090 to 1180°C. The thermocouple was situated underneath the SiC-coated graphite susceptor, and the actual surface temperature was approximately 130°C below the thermocouple temperature. All temperatures quoted here will be the thermocouple temperatures. The total gas flow was varied between 5 - 16 l/min, and the reactor pressure was 100 Torr. The solid composition of the bulk $Al_xGa_{1-x}N$ was kept constant at 0.35, although it varied with growth conditions between approximately 0.3-0.4.

4.2.2 Nucleation conditions

Three types of growth initiation were examined for the AlGaN growth on SiC. These were direct, high-temperature growth; graded (from a higher composition of 0.5-0.6) direct growth; and a lower temperature (1050°C) AlN nucleation layer. The graded composition technique will be referred to as the graded buffer in the discussions in this chapter. Schematics of these three types of structures are given in Figure 4.4.

Figure 4.5 displays AFM images for a typical 400nm $Al_{0.4}Ga_{0.6}N$ layer on SiC (with a graded buffer). The image areas are 1μm x 1μm, 5μm x 5μm, and 20μm x 20μm. In the first, 1μm x 1μm image (Figure 4.5a), steps are visible, confirming that step-flow growth mode was achieved. Also apparent in this image is the high density of dark spots, which correspond to threading dislocations. Counting of the visible pits gives a lower bound for the TDD of $4x10^{10}cm^{-2}$ for this particular wafer. In the larger AFM image areas (Figures 4.5b and 4.5c), islands of 1-5μm diameter are visible.

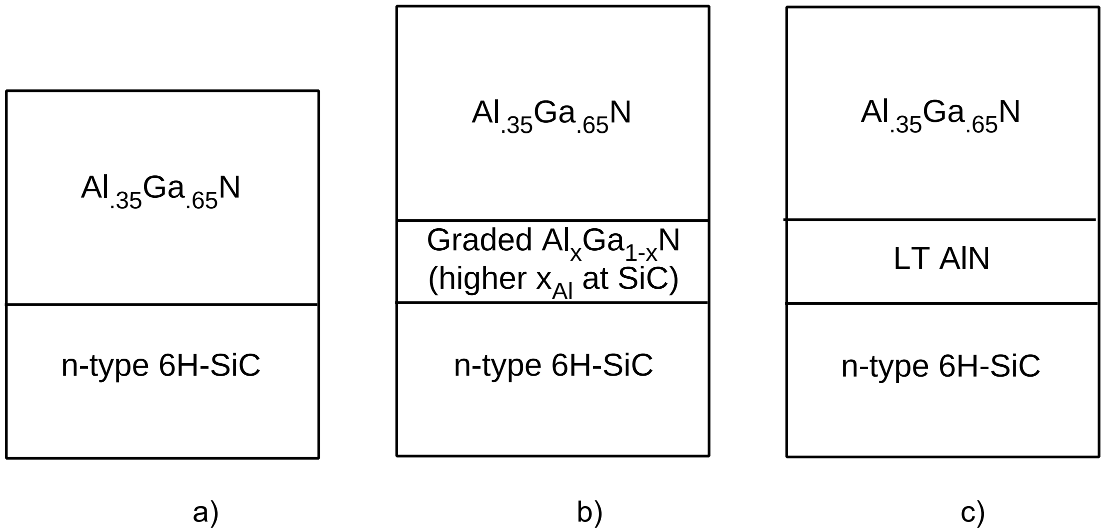

Figure 4.4 Cross-sectional schematics of three methods of growth initiation of AlGaN on SiC: a) direct growth, b) graded composition, and c) lower temperature (LT) AlN layer.

The image height range measured for the $Al_{0.4}Ga_{0.6}N$ in Figure 4.5 was 5.9nm for the 5μm x 5μm scan, and 23.1nm for the 20μm x 20μm scan. Such non-uniformity is undesirable. The surface area of the diodes will enclose many islands, which will result in thickness, strain and possibly composition fluctuations across the devices.

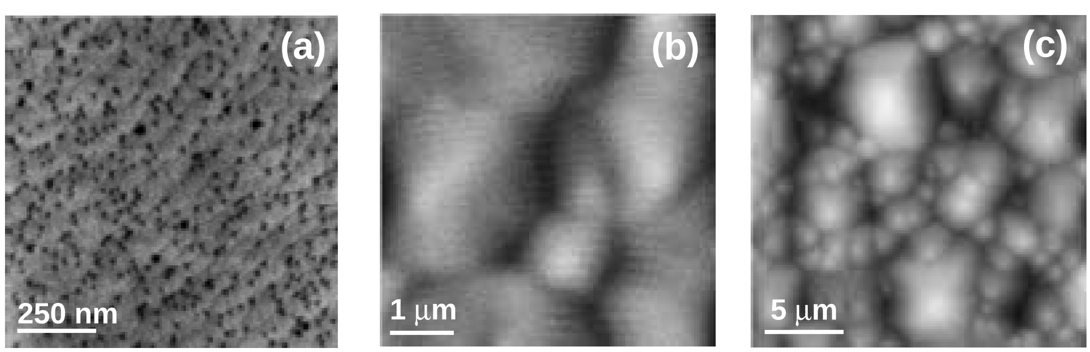

Figure 4.5 AFM images of 400nm thick $Al_{0.4}Ga_{0.6}N$ taken over a) 1μmx1μm area, b) 5μmx5μm area and b) 20μmx20μm area.

Figure 4.6 compares large area (20µm x 2µm) AFM scans of 400nm thick $Al_{0.4}Ga_{0.6}N$ for each of the three different growth initiation techniques. It can be seen that the large islands occur with each of the techniques. However, they are larger and more uniform in size with the AlN buffer. The RMS roughness and image height range with this buffer was also lower, confirming the more uniform growth. The wafers with the graded buffers were also somewhat smoother than the direct growth films, when the grade was concurrent with a ramped growth rate, with an initial (slow) growth rate of approximately 0.6Å/s (the same as was used for the AlN nucleation layer). If the growth rate at the beginning of the compositional grade was the same as the growth rate of the bulk film, the surface was rougher.

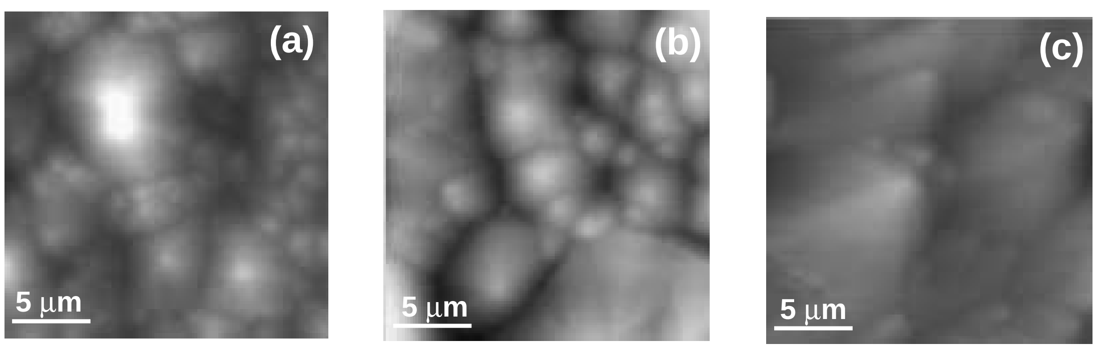

Figure 4.6 AFM images of 400nm thick $Al_{0.4}Ga_{0.6}N$ on SiC with growth initiated by a) direct growth, b) compositional grade and b) AlN nucleation layer.

Dislocation pit counts from smaller area scans of wafers grown by the three techniques, with various growth conditions, revealed that on average the visible TDD was slightly lower for the direct growth technique (low-10^{10} rather than mid-10^{10} cm^{-2}). On the other hand all wafers grown by this technique (with approximately 300-

400nm thickness of AlGaN) were cracked. The same was true for graded buffer wafers without the ramp from slow growth rate. In contrast, the wafers with graded buffer and ramped growth rate, and with AlN nucleation layer, were not cracked (for a thickness of at least 450nm, the thickest films attempted). Initiating growth at a lower growth rate, whether it be for an AlN nucleation layer or graded composition buffer, results in less tensile strain in the post-growth film. This is consistent with the studies of Waltereit et al.[3], in which the lattice mismatch was relieved during growth for direct growth of GaN on SiC, resulting in tensile strain in the final film, whereas use of a coherently grown AlN nucleation layer resulted in a slightly compressive strain in the GaN film. A coherently grown nucleation layer will not relieve lattice mismatch. Obviously the nucleation layer must be grown at a low growth rate for this. Variation of other growth conditions, notably temperature and total flow, did not alleviate the cracking problem for the directly grown films.

Because of the cracking, the direct growth technique was not feasible for detector structures. Instead the graded buffer and AlN buffer structures were used. In the case of a conducting graded buffer, backside contacts can be used to avoid the need for ohmic contacts to the resistive n-type AlGaN. However the distance between the depletion region and the SiC substrate must be sufficient that no photo-generated holes from the SiC will reach the depletion region. Otherwise there will be non-solar-blind response as there was with the p-GaN/i-AlGaN/n-GaN structure (the bandgap of SiC is 2.9eV, even narrower than GaN, although it is indirect and therefore less efficient for photo-generation of carriers).

4.2.3 Growth conditions

Growth conditions were varied to optimize the surface morphology of the thick AlGaN films. Firstly the NH_3 flow was dropped even lower than 0.13 l/min, which had been found to be optimal for the AlGaN/GaN heterostructure growth, to 0.05 l/min. Indeed, the RMS roughness measured by AFM dropped with the lower NH_3 flow. For example, it dropped from 1.35nm to 0.70nm for a 5µm x 5µm area scan.

Total flow was varied between 5l/min and 16l/min, with temperature kept constant at 1120°C. Figure 4.7 presents the 5µm x 5µm images for a total flow of a) 5, b) 12 and c) 16 l/min.

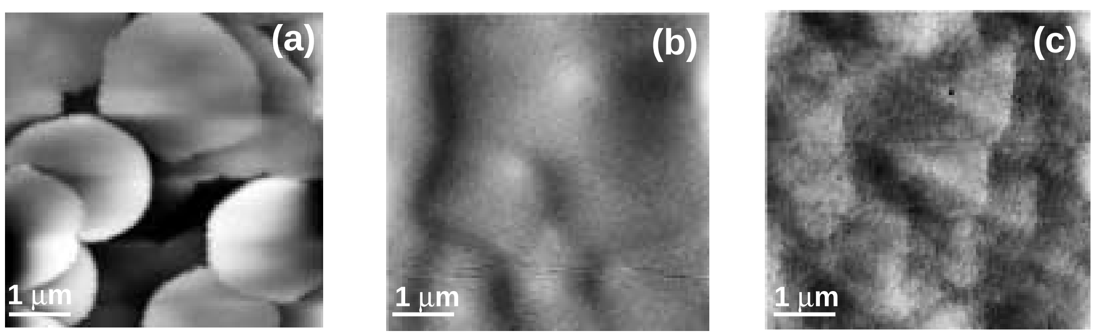

Figure 4.7 AFM images of 400nm thick $Al_{0.4}Ga_{0.6}N$ grown with a) 5l/min total flow, b) 12l/min total flow and c) 16l/min total flow. Note that a) was initiated by direct growth and b) and c) had graded buffers.

From Figure 4.7a it is obvious that 5l/min was too low, with large disk-like features appearing (this film was also hazy to the eye). Conversely, 16l/min was too high, as at such a high precursor velocity the step flow growth mode was lost. Flows of

8l/min (not shown) and 12l/min produced the typical morphology that was portrayed in earlier figures. These flows were comparable to those used for optimized GaN growth. Dislocation pit counts for smaller scans on all but the 5l/min wafer revealed no significant variation in TDD with total flow.

Figure 4.8 plots the AFM image RMS roughness and height range for these 5μm x 5μm images, as well as for several other wafers, as a function of total flow.

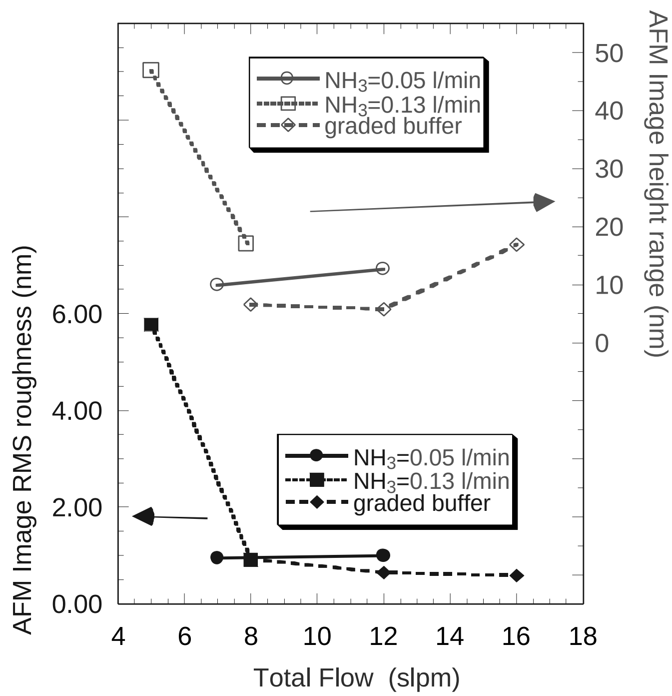

Figure 4.8 RMS roughness and height range of 5μm x 5μm AFM images of 400nm $Al_{0.4}Ga_{0.6}N$, plotted as a function of total flow during growth. Data is taken from $Al_{0.4}Ga_{0.6}N$ grown with 0.05l/min and 0.13l/min NH_3 (direct growth) and with 0.05l/min NH_3 (graded buffer).

The data indicated in Figure 4.8 as 0.05l/min NH_3 and 0.13l/min NH_3 were for wafers with direct growth, and the other data points were for wafers with a graded buffer (with 0.06l/min NH_3). It can be seen that when taking both RMS roughness and image height range into account, a total flow of 8-12l/min is optimal. The smoother morphology obtained with lower NH_3 and with a graded buffer is also evident.

Next, the temperature was varied between 1090 and 1180°C, with total flow of 8l/min or 12l/min. Figure 4.9 presents the 5μm x 5μm images for a) 1090 b) 1120 and c) 1180°C (there were also films grown at 1100, 1140 and 1160°C, not shown). Again the middle ground is optimal. At too low a temperature the low adatom mobility resulted in large pit features (Figure 4.9a). On the other hand, at too high a temperature (Figure 4.9c) step flow growth was again unobtainable, most likely due to too high a dissociation rate of the surface in the H_2 ambient at that temperature and growth rate (approximately 2-3Å/s). Temperatures of 1120-1140°C were ideal for the AlGaN growth at that growth rate.

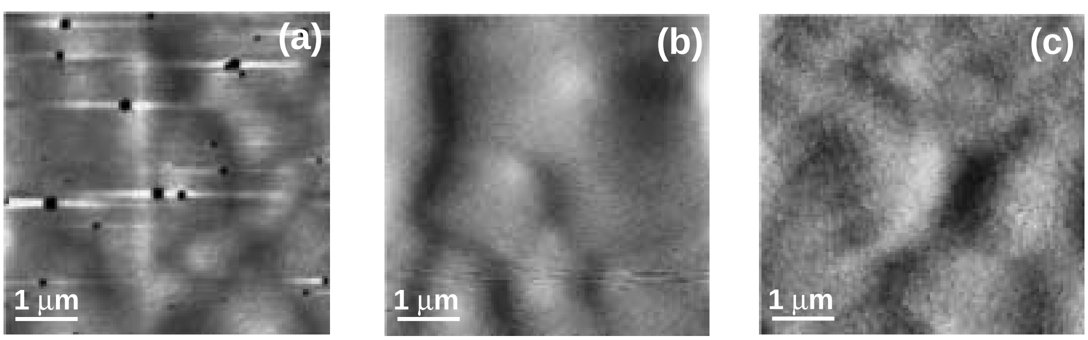

Figure 4.9 AFM images of 400nm thick $Al_{0.4}Ga_{0.6}N$ grown at a thermocouple temperature of a) 1090°C, b) 1120°C and c) 1180°C. Note that a) was initiated by direct growth and b) and c) had graded buffers.

AFM image roughness and image height ranges for 5µm x 5µm scans are again plotted, as a function of the temperature. Inspection of the plot, in Figure 4.10, reveals the increased smoothness as the temperature is raised, due to the increased surface mobility of the adatoms. The smoothness at 1180°C, however, belies the poor step formation seen in the AFM images.

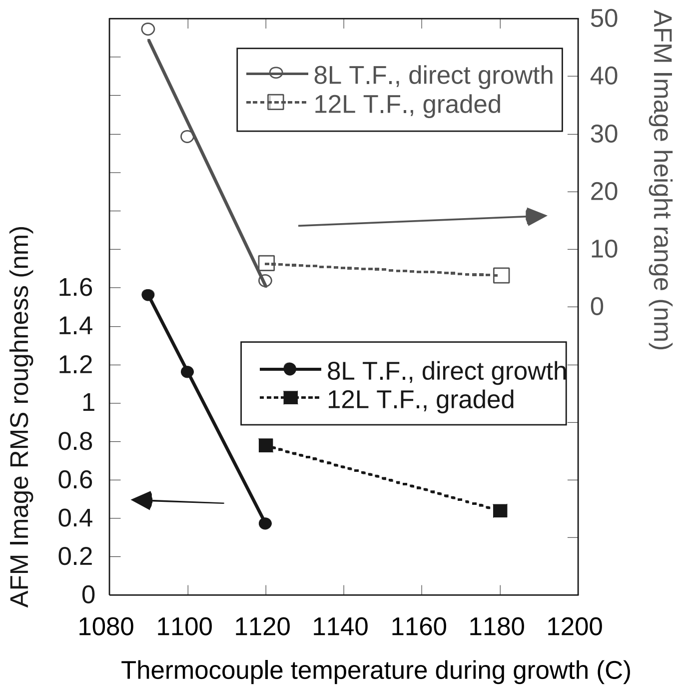

Figure 4.10 RMS roughness and height range of 5µm x 5µm AFM images of 400nm $Al_{0.4}Ga_{0.6}N$, plotted as a function of thermocouple temperature during growth. Data is taken from $Al_{0.4}Ga_{0.6}N$ grown with 8l/min (direct growth) and 12l/min (graded buffer) total flow.

4.2.4 Dislocation reduction using SiN interlayer

The high TDD in the AlGaN, which was not reduced significantly with any of the nucleation techniques or growth conditions, is a matter of concern. GaN templates grown on SiC substrates with the same AlN nucleation layer did not exhibit such a high TDD. XRD rocking curves for such templates presented (0002) FHWM values of 150-200, and $(10\bar{1}2)$ values of 300-400. In contrast the AlGaN films on SiC generally exhibited FWHM values of 200-350 arc-seconds and 750-1100 arc-seconds, respectively (the lower end of the $(10\bar{1}2)$ FWHM range was for the direct growth films, which had slightly lower TDD's). The review of dislocation effects in Chapter 3 has shown that pure edge dislocations have less detrimental effect than mixed character dislocations on photodetector properties. However the inferior properties of the highly dislocated wafer in that study demonstrated that at a high enough density all the dislocations are detrimental.

With such a high edge dislocation density the technique of silicon nitride interlayers was employed to reduce the TDD. However, the use of InGaN layers overgrowth, which was applied for the GaN templates, is undesirable in a solar-blind AlGaN structure due to the narrow bandgap of the InGaN. Meanwhile, Tanaka et al. had successfully demonstrated reduction of (predominantly edge-type) TDD from $2x10^{10}$ to $4x10^{7}$ cm^{-2} in GaN templates on SiC, using Si_xN_y interlayers with GaN and $Al_{0.1}Ga_{0.9}N$ layers grown on top, and no InGaN[5]. This was therefore attempted with the $Al_{0.35}Ga_{0.65}N$ wafers. Wafers with one and with two Si_xN_y interlayers of 0.04-0.6Å were tested, with no apparent reduction in TDD visible in AFM images. Figure 4.11

provides a step-by-step illustration of the process of Si_xN_y deposition and AlGaN overgrowth, with AFM images taken of the wafer at various stages of the process. The images are of a) the initial wafer surface, b) after 0.3Å Si_xN_y deposition, c) after thin (60Å) AlGaN regrowth, d) after thick (600Å) AlGaN regrowth, and e) after a second deposition of 0.3Å Si_xN_y and 600Å AlGaN.

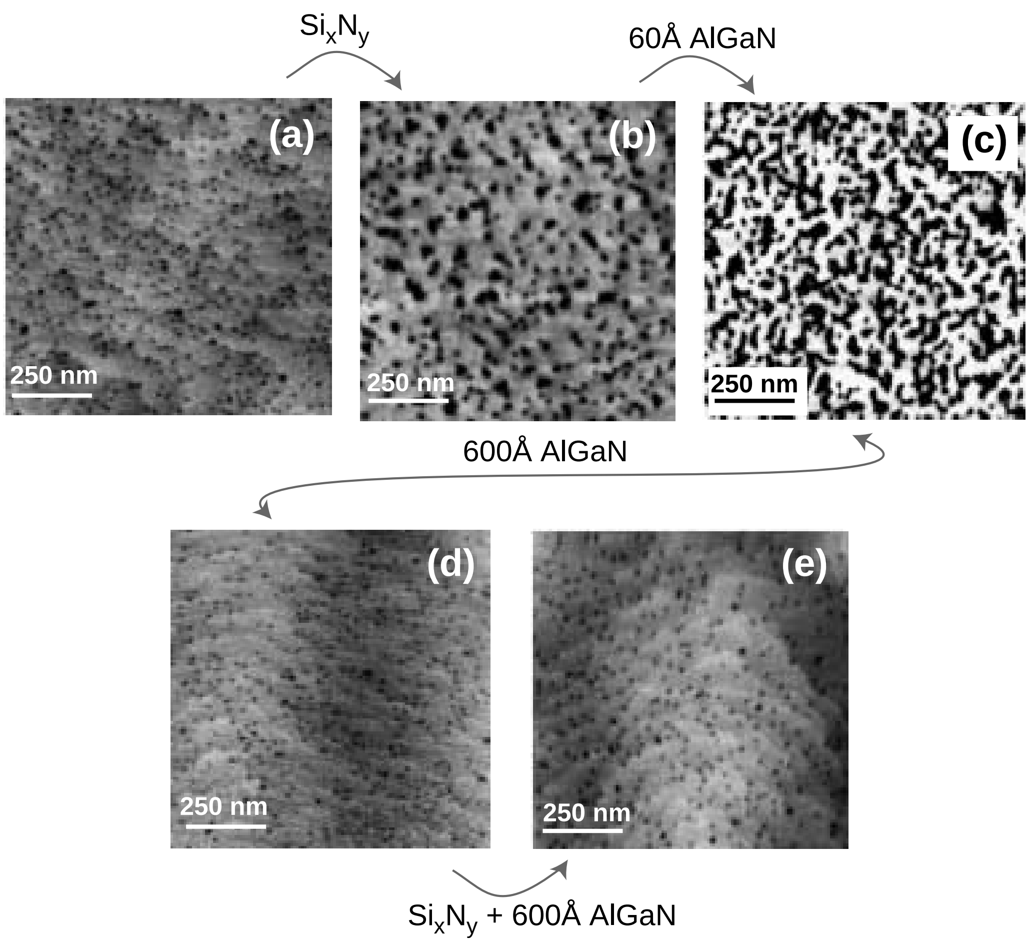

Figure 4.11 AFM images of $Al_{0.4}Ga_{0.6}N$ wafer at different stages of progress during deposition of Si_xN_y interlayers/AlGaN overlayers for dislocation density reduction.

A change in surface morphology after deposition of Si_xN_y and subsequent overgrowth by the AlGaN is visible in Figures 4.11b and 4.11c, respectively. However, the density of nano-scale overgrowth regions prior to coalescence is comparable to the original TDD. Thus, after the AlGaN growth has been completed the TDD is approximately the same as the initial wafer (approximately 5×10^{10} cm^{-2}), even after a second interlayer and overgrowth step (Figs. 4.11e and f).

Obviously, as was experienced with the attempts at conventional LEO of $Al_{0.35}Ga_{0.65}N$, the mobility of the Al adatoms is just too low for overgrowth of dislocations to occur even at this small scale. Given that the technique had been shown by Tanaka et al. to be successful for GaN and low-x_{Al} AlGaN, another experiment was devised in which a thin (60Å) GaN layer was deposited on the Si_xN_y interlayer (and between the interlayers in the case of multiple interlayers) before continuing with the AlGaN growth. Si_xN_y thicknesses of 0.07Å and 0.15Å were used with either one or two interlayers. Again a progressive picture through AFM images is given, in Figure 4.12, for the case where one 0.07Å interlayer was used. So that the GaN layers would be far removed from the depletion layer if a subsequent p-i-n structure were to be grown, the interlayer was deposited after only 600Å of AlGaN had been deposited. Thus it can be seen in Figure 4.12a that the AlGaN islands have not yet fully coalesced after nucleation (this was for a graded buffer). After the GaN growth on top of the Si_xN_y layer, the overgrowth regions do indeed look larger than was seen in the previous experiment (Figure 4.11c). Yet once again, after deposition of a thicker AlGaN layer on top, the TDD counted from AFM images was 3-5×10^{10}cm^{-2}.

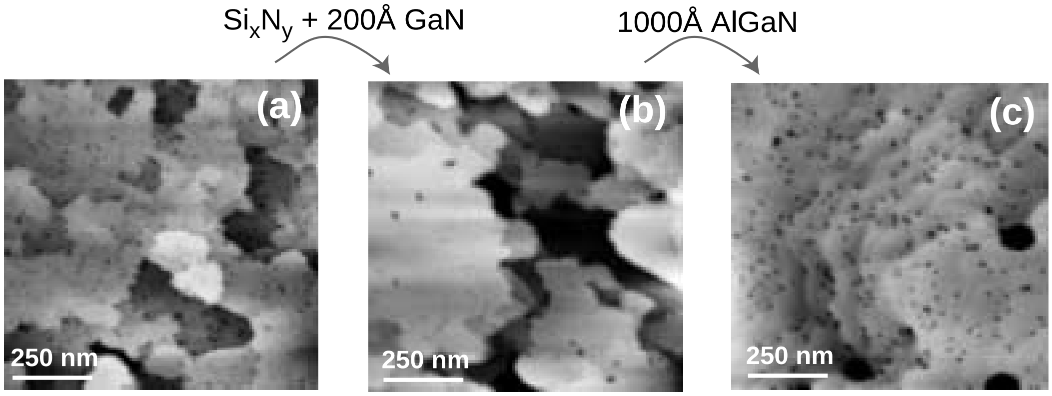

Figure 4.11 AFM images of $Al_{0.4}Ga_{0.6}N$ wafer at different stages of progress during deposition of Si_xN_y interlayer/thin GaN/thick AlGaN overlayer for dislocation density reduction.

Finally an effort was made to enhance the mobility of the adatoms during the AlGaN overgrowth. Several authors had shown that the addition of the precursor TMIn during AlGaN growth could achieve this[6,7,8] (and at the high growth temperatures used for AlGaN, there is no significant incorporation of the In to lower the bandgap). Thus the original experiment with Si_xN_y followed by $Al_{0.3}Ga_{0.7}N$ growth was repeated, but with 0.6Å of Si_xN_y and a TMIn flow of 28μmol/min during the AlGaN growth. Also, the temperature for the AlGaN growth was lowered to 1050°C and the growth rate to 0.5Å/s. To confirm that any perceived effects were not just due to these particular growth conditions, which had not been investigated previously, the Si_xN_y/AlGaN deposition procedure was repeated on another wafer but without the TMIn surfactant. In Figure 4.13 it can be seen that this time the AFM images revealed a dramatic improvement in the surface morphology of the overgrown AlGaN when using the TMIn surfactant. The much improved step flow growth resulting from the enhanced adatom mobility is dramatically evident. Without the TMIn, the surface morphology was unchanged (not shown).

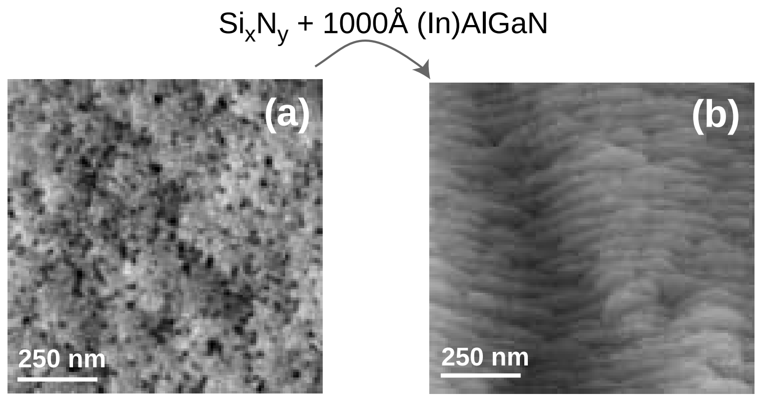

Figure 4.13 AFM images of $Al_{0.4}Ga_{0.6}N$ before and after deposition of Si_xN_y interlayer/AlGaN overlayer with TMIn surfactant during AlGaN overlayer growth.

With these growth conditions, the dislocation pits on the surface had not opened up, and so the technique of pit counting for a TDD lower bound could not be applied. Also, due to slight differences in composition (resulting in slightly offset XRD peak positions) of the underlying wafer and the overgrown AlGaN, the FWHM of XRD rocking curves for the overgrown layer could not be reliably obtained for an assessment of changes in the TDD. Instead, TEM images were obtained for this wafer. These are given in Figure 4.14. As was seen for the GaN template on SiC (figure 3.7), a comparison of g=0002 (Figure 4.14a) and g $=11\bar{2}0$ (Figure 4.14b) reveals a much higher edge-type TDD (on the order of 10^{10} cm^{-2}) than mixed character TDD (on the order of 10^{8} cm^{-2}) for the underlying AlGaN template on SiC. This confirms the TDD estimated from earlier AFM images was accurate.

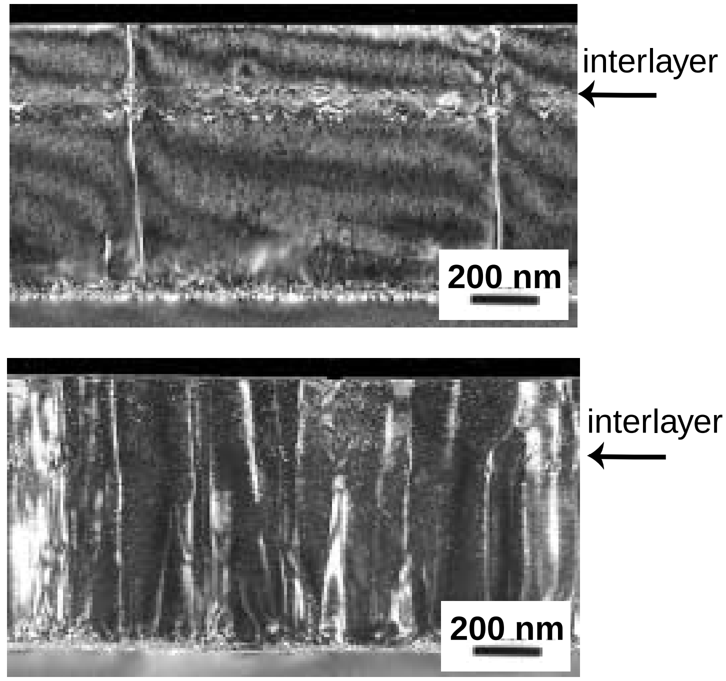

Figure 4.14 Cross-section (bright field) TEM micrograph of $Al_{0.4}Ga_{0.6}N$/SiC template with Si_xN_y interlayer followed by AlGaN overlayer grown using TMIn surfactant. a) g = 0002, b) g = $11\bar{2}0$.

Unfortunately, the TEM images also reveal that the interlayer has not, in this case, reduced the TDD for the overlying TMIn surfactant-assistant layer. Both the edge-type and mixed character TD's can be seen to propagate past the interlayer. However, the dramatic improvement in surface morphology seen in the AFM images does indicate an improvement in mobility of the Al adatoms, and therefore a more detailed investigation of the use of the interlayer may result in a reduction of the high TDD. Note that the areas of contrast underneath the interlayer boundary line in Figure 4.14 are due to the regrowth interface prior to interlayer deposition.

4.2.5 Si doping effects

In the discussion earlier this section about cracking problems with the AlGaN/SiC, it was stated that with the graded and AlN buffer layers cracking was avoided. However, this was for undoped films. With the addition of Si to obtain an n-type bulk AlGaN layer (and in the case of the graded buffer, with Si doping of the graded region also), films of 300-400nm thickness were cracked. Furthermore, the higher the Si doping, the more severe was the cracking. A series of p-i-n structures was grown with identical p-i layers but different DiSi flow (f_{DiSi}) during growth of the n-layer. Figure 4.15 shows AFM images of the n-layers prior to the p-i deposition. The n-layers were 100nm thick, with a 60nm n-type graded buffer doped at the same level as the bulk n-layer. The three images are of $Al_{0.4}Ga_{0.6}N$ with a) f_{DiSi} = 1.8nmol/min, graded from x_{Al} = 0.6, b) f_{DiSi} = 7.1nmol/min, graded from x_{Al} = 0.6, and c) f_{DiSi} = 35.6nmol/min, graded from x_{Al} = 0.5.

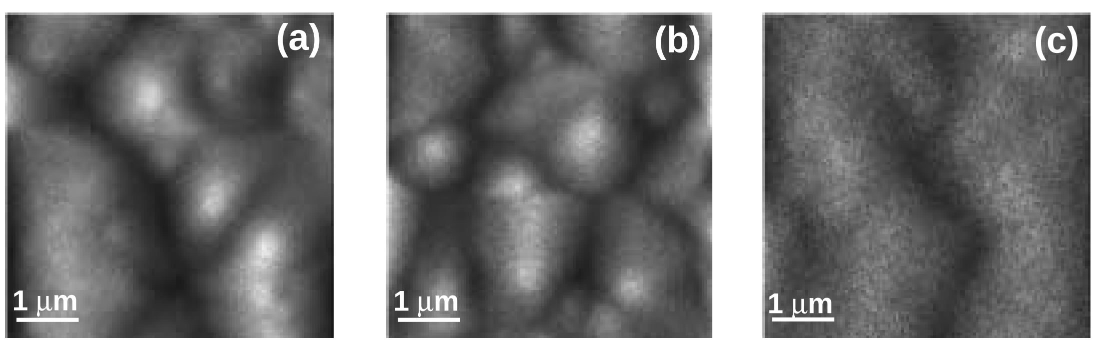

Figure 4.15 AFM images of 100nm $Al_{0.4}Ga_{0.6}N$:Si with DiSi injection of a) f_{DiSi} = 1.8nmol/min, b) f_{DiSi} = 7.1nmol/min, and c) f_{DiSi} = 35.6nmol/min.

A fourth wafer had f_{DiSi} = 7.1nmol/min, graded from x_{Al} = 0.5, and looked similar to b). The third image, of the most highly doped film (Figure 4.15c) is strikingly different in morphology to the others, and to the earlier undoped films. The surface is much smoother, and the islands replaced by a larger scale undulation of film thickness. After the p-i structures (400Å GaN:Mg + 4000Å $Al_{0.4}Ga_{0.6}N$) were deposited, the structure which had this highly doped n- $Al_{0.4}Ga_{0.6}N$ layer underneath was severely cracked. The structures with f_{DiSi} = 7.1nmol/min had only a few cracks, whilst the structure with f_{DiSi} = 1.8nmol/min had no cracks. Evidently the more doped films had a higher tensile strain, which may be the reason for the change in morphology. This was further confirmed by 2θ-ω XRD scans of the wafers. The higher the doping, the further the AlGaN peak position was shifted to the right, indicating greater contraction of the in-plane lattice constant (and therefore greater tensile strain). It was not an indication of higher x_{Al} content, as the SIMS investigations presented in Chapter 2 had shown that the addition of DiSi participates in the pre-reactions involving the TMAl precursor, and therefore would not result in an enhancement of Al incorporation.

4.3 AlGaN detectors on SiC

4.3.1 n-type doping of AlGaN

In order for a high field in the depletion region and efficient carrier diffusion in the bulk p- and n- regions of the photodiode, the p- and n- regions should be reasonably highly doped and not too resistive. This is why p-GaN was used for the diodes in this study, as effective p-type doping of $Al_{0.35}Ga_{0.65}N$ is currently unattainable. On the other hand n-type doping is possible, but increasingly difficult at higher x_{Al}, resulting in resistive layers (see review in Chapter 2). Because of the problems with cracking of thick Si-doped layers, Hall measurements could not be used to assess the efficiency of the Si doping in the AlGaN layers on SiC. Instead, the p-i-n structures that were discussed in the previous section, with different doping levels in the n-AlGaN, were used to compare the n-AlGaN. Figure 4.16 gives schematic cross-sections of the general design of p-i-n diodes on SiC substrate, both with an insulating buffer (Figure 4.16a) and with a conducting buffer and backside contacts (Figure 4.16b).

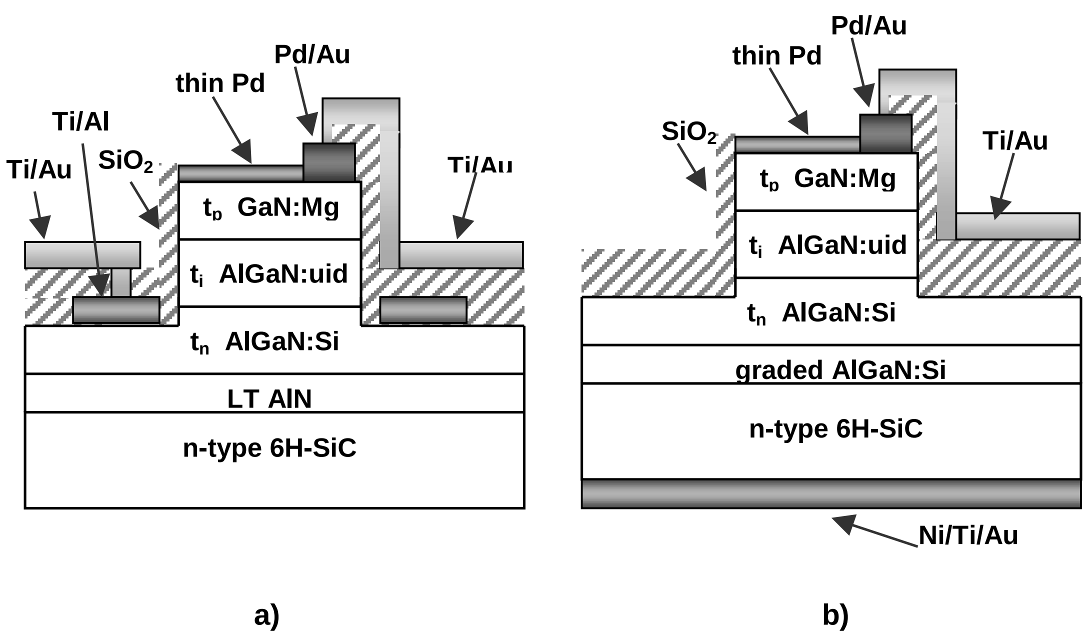

Figure 4.16 p-GaN/i-AlGaN/n-AlGaN diode structures on SiC. a) Insulating buffer (n contacts to the top of the n-AlGaN). b) Conducting buffer (backside n contacts to the n-SiC)

For this n-doping study of the conducting buffer, backside contacts were used. The thickness for each layer, as stated in the previous section, was t_p = 400Å, t_i= 4000Å, and t_n=1000Å, with 600Å buffer graded from x=0.6 or x=0.5. I-V characteristics were measured for this series of wafers. Figure 4.17 indicates the variation of forward bias behavior with Si doping and initial grade composition. Figure 4.17a shows forward bias curves for the devices from each of the three wafers featured in Figure 4.15. A dramatic difference in the resistance of these diodes is evident.

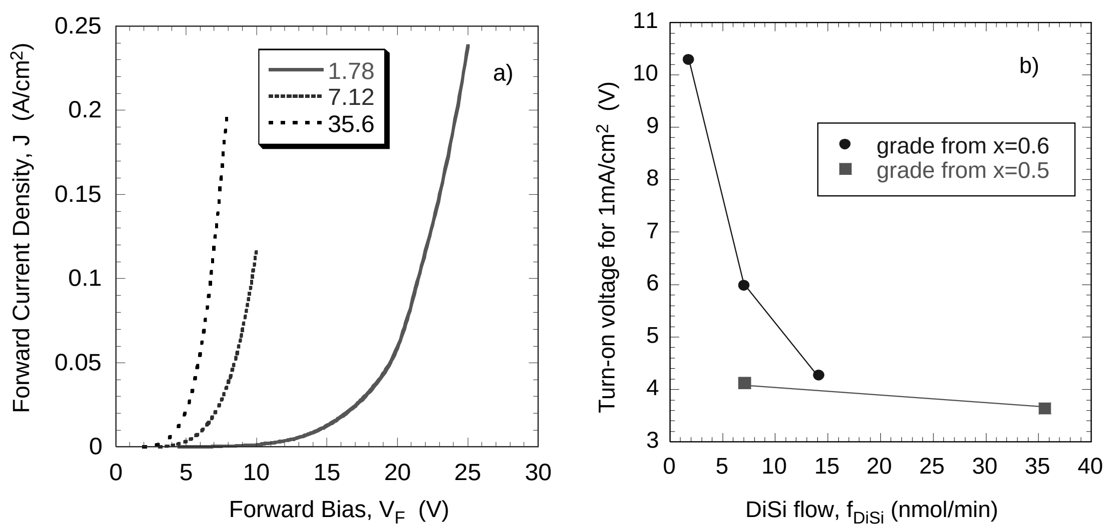

Figure 4.17 Forward bias behavior of conducting buffer p-GaN/ i-AlGaN/n-AlGaN diodes with different Si doping and grading of the n-AlGaN. a) Forward bias characteristics for different values of f_{DiSi} (given in nmol/min). b) Average forward bias value at which current density reached 1mA/cm^2, as a function of f_{DiSi} and initial AlGaN grade composition.

In Figure 4.17b the voltage (averaged over many devices for each wafer) at which the forward current density reached a value of 1mA/cm^2 is plotted against f_{DiSi} for the AlGaN:Si layer. Again the decreasing resistance with increasing f_{DiSi} is clear. The higher resistance is particularly marked when the initial composition for the AlGaN graded buffer is higher, confirming that AlGaN of higher composition is more resistive and more difficult to dope n-type. The effect of the Si doping on tension in the film and resistance of the n-layer thus establishes a tradeoff between minimizing cracking (which results in severe leakage in the diodes) and maximizing conductivity of the AlGaN.

4.3.2 Leakage current

In Chapter 3 it was mentioned that occasionally processing problems or material defects would cause severe leakage in some or all diodes from a wafer. This was true for all of the devices fabricated on the cracked AlGaN structures on SiC substrate. It was also true for most devices on the less cracked structures, however there were also devices with low leakage currents (and reasonable forward bias characteristics, indicating sufficient doping). Figure 4.18 gives the leakage currents for diodes fabricated on a structure which had t_p = 400Å, t_i = 2000Å, t_n = 2000Å, f_{DiSi} = 7.1nmol/min, and an initial grade composition of 0.5. At a reverse bias of –5V the leakage current is around 10-15nA/cm^2. This is comparable to the leakage currents at –5V for the solar-blind devices on LEO GaN (Section 3.4), however with the thicker depletion region the reverse field at that bias is lower in this case. Also, the leakage current more rapidly increases with bias than the devices on LEO. This dislocation-induced soft breakdown indicates that at such high densities of 10^{10} cm^{-2}, even the edge dislocations are contributing to the leakage in the devices.

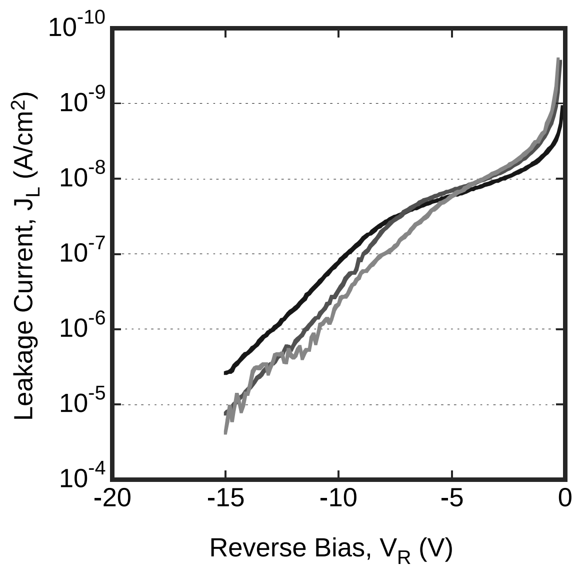

Figure 4.18 Best leakage current densities for conducting buffer p-GaN/i-AlGaN/n-AlGaN diodes on SiC substrate.

4.3.3 Spectral response

Diode structures were grown on SiC with and without a conducting buffer, for comparison of spectral response. Figure 4.19 shows the current responsivity for diodes fabricated on two p-i-n structures with a conducting buffer (see diode schematic in Figure 4.16b). They both have t_p = 400Å and t_i = 2000Å. They differed in thickness of the n-layer above the graded buffer - one had t_n = 1000Å and the other had t_n = 2000Å. It is important to keep in mind that the thickness of the n-layer is representative of the proximity of the i-layer to the SiC (t_n+600Å). It is obvious that the magnitude of the photoresponse of the devices on SiC is significantly less than for the p-GaN/i-AlGaN/n-GaN devices investigated previously (0.02A/W compared to 0.05A/W). Also, comparing the two curves in Figure 4.19, the thinner t_n results in a higher photoresponse at wavelengths above the cutoff wavelength of the $Al_{.4}Ga_{.6}N$ at 280nm. (This will be referred to as the "tail" response in the discussion below.)

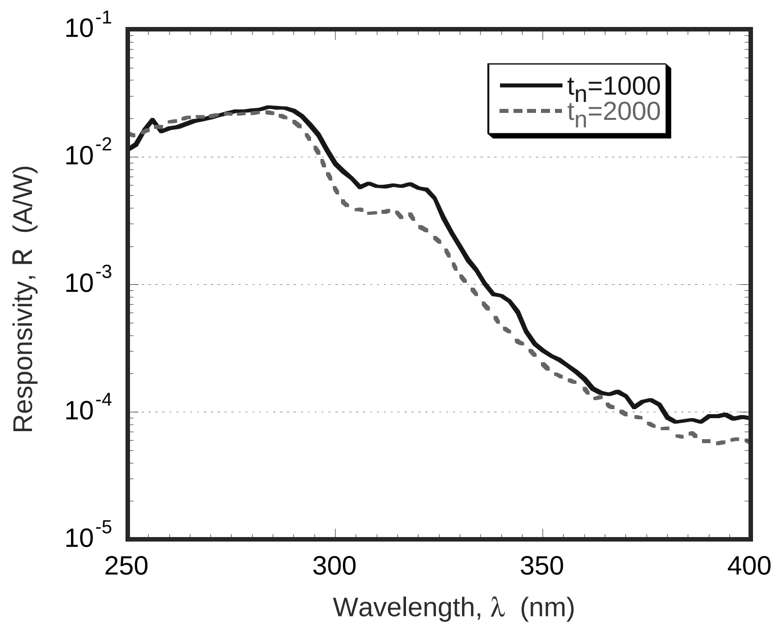

Figure 4.19 Spectral response curves for diodes fabricated on p-GaN/i-AlGaN/n-AlGaN/SiC structure with backside contacts to the conducting buffer. The thickness of the n-AlGaN was 1000 or 2000Å.

To understand these results it is helpful to recall that carriers generated due to absorption in the depletion region (i-layer) must reach the edge of the depletion region and recombine in the bulk p-GaN or n-AlGaN layers in order to contribute to photocurrent (refer to Figure 3.1 in which mechanism of photocurrent in p-i-n diodes is indicated). Similarly, all minority carriers generated in the bulk layers must reach and traverse the depletion layer and recombine as majority carriers in the bulk layer on the other side of the depletion region.

The i-layer in these devices is four times the thickness of the i-layer in the p-GaN/ i-AlGaN/n-GaN devices, and it was expected that these devices would have a higher responsivity due to the greater absorbing region. However this is not the case – implying that less of the absorption in these structures contributes to photocurrent. It is also true that the p-GaN is thicker in this case than for the earlier structures, however there are no quantum wells to impede the minority electron flow into the AlGaN depletion region so this should not be a significant cause of the low responsivity. It is apparent, therefore, that a high proportion of the photogenerated carriers are recombining before they can traverse the depletion region. A high recombination rate suggests that the AlGaN is of poor electrical quality.

Another diode structure was grown with t_p = 400Å, t_i = 4000Å and t_n = 1000Å. Again, if the photogenerated carriers were being efficiently transported across the depletion region, this structure, with a thicker total absorbing region, should have had a higher peak photoresponse. Instead the responsivity was lower still. This further indicates that there is a high incidence of recombination or trapping of carriers in the depletion region. The thicker the depletion region, the more chance of recombination or trapping occurring before the photogenerated carriers can reach the bulk layers.

This third structure also exhibited less of the tail response seen in Figure 4.19, at wavelengths to which the AlGaN is transparent. The tail is most likely due to absorption in the underlying SiC, which has a bandgap energy of 2.9eV. The thicker the total AlGaN, the more there will be recombination of photogenerated holes from the SiC before they can traverse the i-layer and recombine in the p-GaN.

The thickness of the n-layer with a conducting buffer was limited to 2000Å due to tension introduced by the Si-doping. Thus the tail response could not be reduced by increasing t_n instead of t_i. Instead, diodes were fabricated on a structure with an insulating buffer. Such devices were indicated schematically in Figure 4.16a. These diodes had t_p = 250Å, t_i = 2000Å and t_n = 2000Å. Due to temperature drift in the reactor the composition was a little lower than intended, with x_{Al} = 0.3. The insulating buffer was 0.4μm thick, and consisted of a 200Å AlN nucleation layer followed by a 4000Å grade to $Al_{0.3}Ga_{0.7}N$. For comparison to the p-GaN/i-AlGaN/n-GaN diodes in Chapter 2 the p-layer consisted of p-GaN/p-$Al_{0.1}Ga_{0.9}N$ quantum wells with a p-GaN cap. The spectral response is given in Figure 4.20.

It can be seen that with the insulating buffer the spectral response is much improved compared to the conducting buffer structures. The tail due to absorption in the SiC is significantly reduced. Note that the tail is somewhat jagged; this is measurement noise due to insufficient averaging time during measurements. The peak responsivity is 0.08A/W at a wavelength of 292nm, corresponding to an external quantum efficiency of 35%. The optical quality of the AlGaN in the depletion layer has been significantly improved by the addition of the 0.5μm insulating buffer. This large increase in separation of the depletion region from the substrate (and nucleation region) has obviously greatly reduced the optically denigrating defect content in the material.

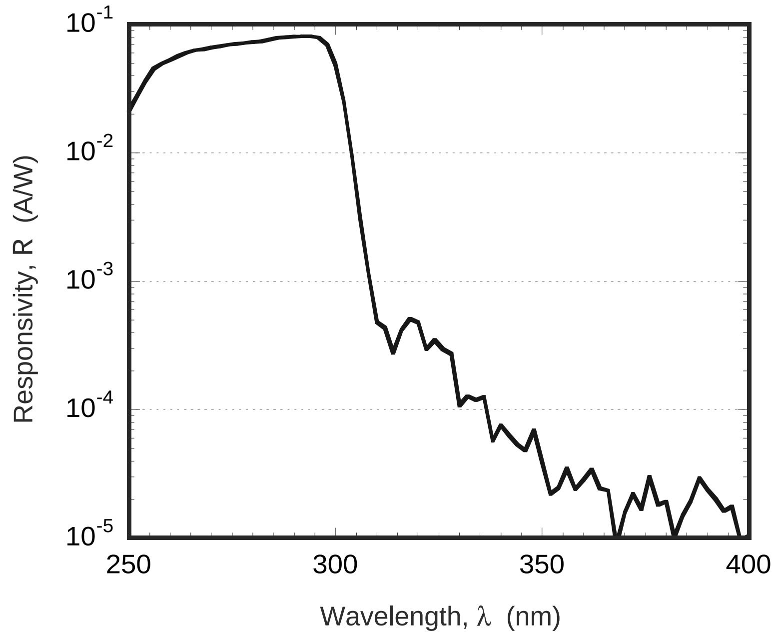

Figure 4.20 Typical spectral response curve for diodes fabricated from a p-GaN/i-AlGaN/n-AlGaN/SiC structure with an insulating buffer.

The initial cutoff is quite sharp, dropping 2 orders of magnitude in 17nm. However 3 orders of magnitude reduction was not achieved until nearly 50nm after the peak. This is due both to the slight contribution from the SiC substrate and to band-tail states from the (still high) dislocation density in the material. Further optimization of the insulating nature of the buffer, combined with dislocation reduction in the AlGaN, should improve both the peak responsivity and the cutoff sharpness.

4.4 Conclusions

Use of GaN for the n-layer in a solar-blind p-i-n detector (with $Al_{0.35}Ga_{0.65}N$ for the i-layer) results in non-solar-blind broadening of the spectral cutoff. Bulk AlGaN growth enables use of an n-AlGaN layer and also a thicker i-AlGaN layer for higher responsivity. Growth of bulk AlGaN on SiC requires careful optimization of the nucleation conditions to achieve a balance between the compressive lattice mismatch and the tensile thermal mismatch. Si doping introduces further tensile strain. The bulk AlGaN grown on SiC has a high edge-type TDD, much higher than GaN grown on SiC. The smoothest surface morphologies were obtained with a total flow of 8-12 l/min, thermocouple temperature of 1120-1140°C, and NH_3 flow of 0.5 l/min. Surface morphology could be significantly improved when TMIn was used as a surfactant to enhance the mobility of the Al adatoms during AlGaN growth.

The p-GaN/i-AlGaN/n-AlGaN diodes on SiC substrate exhibited reasonably low leakage currents and high responsivity. With a conducting buffer the diodes exhibited non-solar-blind spectral response due to absorption in the SiC. With an insulating buffer this tail response was almost eliminated. The TDD must be reduced to further improve the photodiode properties. The use of a Si_xN_y interlayer for TDD reduction was not successful in the studies presented here but combining this technique with the TMIn surfactant effect bears promise for future efforts.

4.5 References

---

1. T. Akasaka, Y. Kobayashi, S. Ando, N. Kobayashi, and M. Kumagai, "Selective MOVPE of GaN and $Al_xGa_{1-x}N$ with smooth vertical facets." *J. Cryst. Growth* **189/190**, 72-77 (1998).

2. M.D. Bremser, W.G. Perry, T. Zhevela, N.V. Edwards, O.H. Nam, N. Parikh, D.E. Aspnes, and Robert F. Davis, "Growth, doping and characterization of $Al_xGa_{1-x}N$ thin film alloys on 6H-SiC(0001) substrates." *MRS Internet J. Nitride Semicond. Res.* **1,** 8 (1996).

3. P. Waltereit, O. Brandt, A. Trampert, M. Ramsteiner, M. Reiche, M. Qi, and K.H. Ploog "Influence of AlN nucleation layers on growth mode and strain relief of GaN grown on 6H-SiC(0001)." *Appl. Phys. Lett.* **74,** 3660-3662 (1999).

4. H. Lahrèche, M. Leroux, M. Laügt, M. Vaille, B. Beaumont, and P. Gibart "Buffer free growth of GaN on 6H-SiC by metalorganic vapor phase epitaxy." *J. Appl.Phys.* **87,** 577-583 (2000).

5. S. Tanaka, M. Takeuchi, and Y. Aoyagi "Anti-surfactant in III-nitride epitaxy – quantum dot formation and dislocation termination-." *Jpn. J. Appl. Phys.* **39,** 831-834 (2000).

6. C.K. Shu, J. Ou, H.C. Lin, W.K. Chen and M.C. Lee, "Isoelectronic In-doping effect in GaN films grown by metalorganic chemical vapor deposition." *Appl. Phys. Lett.* **73,** 641-643 (1998).

7. S. Yamaguchi, M. Kariya, S. Nitta, H. Amano, and I. Akasaki, "Strain relief and its effect on the properties of GaN using isoelectronic In doping grown by metalorganic vapor phase epitaxy." *Appl. Phys. Lett.* **75,** 4106-4108 (1999).

8. G. Pozina, J.P. Bergman, B. Monemar, S. Yamaguchi, H. Amano, and I. Akasaki, "Optical spectroscopy of GaN grown by metalorganic vapor phase epitaxy using indium surfactant." *Appl. Phys. Lett.* **76,** 3388-3390 (2000).

Chapter 5. Conclusions and future work.

With $Al_xGa_{1-x}N$-based material and device technology still at an early stage of development, the studies presented here have resulted in unmistakable advancements in the growth of AlGaN and in knowledge of critical aspects of ultraviolet detector performance and design. Further work, including the recommendations detailed later in this chapter, will certainly lead to yet more advancements and improve upon the detector results presented here.

5.1 AlGaN growth on sapphire substrate.

The studies into $Al_xGa_{1-x}N$ ($x_{Al} \geq 0.3$) growth emphasized that achievement of smooth, defect-free AlGaN (regardless of the substrate and/or underlying layers) is substantially more difficult than for GaN grown by MOCVD. This is due in no small way to the low mobility of Al adatoms on the epitaxial surface, to pre-reactions which necessitate low growth pressures, and to the high bond strength of Al to impurities and to substrate and mask constituents (notably O, C and N).

The studies conclusively demonstrated the tendency of increased defect formation with increasing Al content and increasing strain in the AlGaN layer. When grown on GaN templates the strain increases with x_{Al} due to the increase in lattice mismatch. Too much strain can result in the occurrence of cracking – this occurs during growth and not after cooldown, and is therefore due to the lattice and not the thermal mismatch. The presence of dislocations in the underlying template also enhances defect formation in the AlGaN.

Improvement of the AlGaN morphology and a first-order reduction of the defects requires maximization of surface mobility during growth. It was found that this could be achieved by reducing nitrogen overpressure by reducing NH_3 flow. Thereby the effect of increasing defect formation with Al content could be counteracted, resulting in AlGaN that more resembled GaN in surface morphology for thin AlGaN layers grown on GaN templates. Reduction of threading dislocations by LEO completed this transformation to a low-defect GaN-like morphology.

In addition to extended defects, point defects due to impurity incorporation in GaN and AlGaN are ever-present. SIMS investigations of C and O content showed they could be reduced, by optimizing growth conditions, such as by raising the growth temperature. Incorporation unavoidably increases with Al content though, due to the aforementioned high bond strengths of Al to O and C.

Attempts using non-traditional mask materials for LEO of $Al_xGa_{1-x}N$ (in addition to the traditional mask material SiO_2) were unsuccessful, with no selectivity achieved for SiO_2, sapphire, Pt and TiN masks. Again this is due to the high sticking probability and low mobility of the Al adatoms, on both the masked and unmasked surfaces.

5.2 AlGaN on SiC.

For bulk AlGaN growth on SiC, the initial growth on the substrate will determine whether the (compressive) lattice mismatch will balance the (tensile) thermal mismatch. If the lattice mismatch is relieved too much during growth the residual tensile strain will cause cracking, at a thickness insufficient for device purposes

(<0.5μm). This occurred for direct growth of AlGaN at high temperature and fast growth rate (2-3Å/s). Initiating the growth with a slow growth rate AlN layer (grown at a lower temperature) or graded AlGaN layer (gradually ramped to bulk composition and growth rate) resulted in less residual tensile strain and no cracking.

Unlike the thin layers on GaN templates, the bulk AlGaN layers grown under reduced NH_3 conditions did not show a GaN-like morphology (compared to GaN templates grown on SiC with an AlN nucleation layer). The surface morphology was characterized by large islands which were1-5μm in diameter (with step flow growth on and between the islands). The TDD was also much higher than for the GaN templates, with (mostly edge-type) TDD's of 2-5x10^{10} cm^{-2}.

Once more the low surface mobility of the Al adatoms interfered with TDD reduction techniques. Use of a Si_xN_y submonolayer, which masks edge dislocations and can result in subsequent reduction of the edge dislocations in overgrown layers, did not work when overgrown with AlGaN. The use of TMIn as a surfactant to enhance the mobility shows promise for improvement of surface morphology and reduction in TDD of the overgrown AlGaN.

The addition of Si to thick AlGaN layers grown on SiC substrate increases tension in the layers and causes cracking. Yet with the resistance of the $Al_xGa_{1-x}N$ increasing as x_{Al} increases, higher Si doping is needed for n-type conductivity for p-i-n photodiodes. A tradeoff ensues between n-layer thickness and conductivity, and cracking, for p-i-n AlGaN structures on SiC substrate.

5.3 Dislocations and photodiodes

The investigations into the effect of threading dislocations on GaN and AlGaN photodiodes revealed unequivocally that they are detrimental to detector performance. This study was performed primarily with GaN p-i-n photodiodes grown on GaN templates of various TD compositions and densities.

GaN (and its alloys) when epitaxially grown on sapphire have a high mixed and edge TDD. Optimization of the nucleation conditions can reduce the TDD from 10^9-10^{10} cm^{-2} to low-mid-10^8 cm^{-2}. We used several approaches for further dislocation reduction. The use of a submonolayer silicon nitride (Si_xN_y) interlayer overgrown with thin InGaN layers appears to reduce the edge-type TDD. Growth on SiC substrate reduces the mixed-type TDD. LEO GaN has a dramatically reduced TDD, both mixed and edge character.

The studies showed that the presence of edge dislocations has less effect than mixed on leakage current and spectral broadening. That is, a much bigger decrease in leakage current can be obtained by reducing mixed- than by reducing edge-type TDD's. However, reducing edge-type TDD from very high levels (high being10^9-10^{10} cm^{-2}) does have an effect.

Growth of photodiodes on LEO GaN results in the lowest leakage currents, due to the very low overall TDD. Yet spectral broadening of the GaN photodiode response was a little worse, possibly due to impurities from the SiO_2 mask material. Impurities in the overgrown GaN originating from the mask are an issue that still requires some treatment in LEO studies. Furthermore, although it is reduced, there is still significant leakage current when LEO is used, higher than would be expected in photodiodes with such a wide bandgap.

Measurements of leakage current in GaN photodiodes with a reduced TDD revealed that it is at least partly due to defects in the i-layer. This layer is highly compensated. The leakage current is not due in any part to the sidewalls – devices with and without passivation, and with different perimeter-to-area ratios, did not exhibit differences in leakage currents. This was true even when the TDD was not reduced by LEO.

In a p-GaN/i-$Al_{0.33}Ga_{0.67}N$/n-GaN structure designed to prevent photogenerated carrier movement from p- and n-GaN to the i-AlGaN (for solar-blind behavior), again the TD's were found to increase leakage current and broaden the spectral response. In this case the TD's cause additional broadening of the solar-blind cutoff, by enabling a larger photocurrent contribution from absorption in the GaN. Speed measurements showed that TD's (both edge- and mixed-type) also contribute to a slow tail in the speed response (the pulsed response was the combination of a fast and a slow exponential decay, except on the LEO wing).

5.4 Solar-blind detectors

The p-GaN/i-AlGaN/n-GaN structure has two major drawbacks - the broadening of solar-blind cutoff due to contribution from absorption in the GaN, particularly in presence of TDD, and the limitation of the i-AlGaN thickness to 500Å to avoid cracking, which allows a peak responsivity of only 0.05 A/W (external quantum efficiency of only 22%). Experiments showed that the broadening is due to holes from n-GaN, which combined with the requirement of thicker i-AlGaN necessitates an n-AlGaN buffer for solar-blind p-i-n diode design.

LEO of high-x_{Al} AlGaN was not found to be possible, with four mask materials investigated. SiC substrate was therefore chosen for development of thick AlGaN. The benefits of improved detector performance should outweigh the increased substrate cost. Although the TDD for the bulk AlGaN on SiC was very high it consisted mostly of edge-type dislocations. Thus, solar-blind diodes on SiC substrate exhibit relatively low leakage currents at moderate fields.

The employment of a conducting buffer to enable use of ohmic contacts to the n-type SiC instead of to the n-AlGaN resulted in substantial photocurrent from the SiC. The thickness limitations of the conducting buffer due to the tensile strain introduced by the Si-doping meant that the i-layer was too close to the SiC.

With an insulating buffer, p-GaN/i-$Al_{0.3}Ga_{0.7}N$/n-$Al_{0.3}Ga_{0.7}N$ diodes were fabricated which exhibited good detector characteristics. The peak responsivity was 0.08A/W at 292nm (quantum efficiency of 35%), with a 3 orders of magnitude drop within 50nm. These detectors have a better responsivity but slightly worse cutoff characteristics and leakage currents compared to the p-GaN/i-$Al_{0.33}Ga_{0.67}N$/n-GaN photodiodes. Thicker i-AlGaN layers resulted in decreased responsivity due to the high recombination rates in the highly defective AlGaN.

5.5 Future work.

Improvement of the solar-blind detectors presented here requires first and foremost a reduction in the defect density of the AlGaN. Although growth on SiC substrate does reduce the mixed-type TDD, the edge-type TDD must be reduced below the present levels of 10^{10} cm^{-2}. Optimization of the SiN interlayer technique with TMIn surfactant shows potential and should be developed further – only initial studies were carried out in this work. Furthermore, reduction of the point defects by reduction of the impurities present in the MOCVD system (given that the growth conditions cannot be altered further due to surface morphology and pre-reaction restrictions) is necessary.

Additional defect reduction will be attained if a thicker buffer layer can be grown prior to deposition of the p-i-n structure. The detectors fabricated with the AlN nucleation layer had 0.5µm of insulating AlGaN, graded from AlN to $Al_{0.3}Ga_{0.7}N$, underneath the p-i-n structure. Optimization of both the AlN and the graded layer should enable this insulating layer to be made thicker without cracking the p-i-n structure. Furthermore, with a thick higher-x_{Al} buffer narrow-band spectral response could be achieved with backside illumination. This also holds true for growth on sapphire substrates. With defect reduction, perhaps using a combination of the Si_xN_y/TMIn surfactant technique for the edge-type dislocations and the low-temperature AlN interlayer pioneered by Amano et al.[1] for the mixed-type dislocations, low-defect density bulk AlGaN with a higher-x_{Al} buffer layer could be grown on sapphire substrates too. Recent results have certainly shown that the use of a higher-x_{Al} buffer layer alone, epitaxially grown AlGaN of relatively high quality can be obtained[2,3].

Finally, preliminary temperature-dependent studies of the defect levels causing leakage current in the absence of threading dislocations were inconclusive and therefore not included in this work. A thorough study is required, with temperature both increased above and decreased below room temperature. Other temperature-dependent techniques should also be used, such as deep level transient spectroscopy, in order to pinpoint changes in defect levels with.

5.6 References

1. H. Amano, M. Iwaya, N. Hayashi, T. Kashima, S. Nitta, C. Wetzel, and I. Akasaki, "Control of dislocations and stress in AlGaN on sapphire using a low temperature interlayer." *Phys. Stat. Sol.* (b) **216,** 683-689 (1999).

2. U. Karrer, A. Dobner, O. Ambacher, and M. Stutzmann, "AlGaN-based ultraviolet light detectors with integrated optical filters." *J. Vac. Sci. Technol.B* **18,** 757-760 (2000).

3. D.H. Lambert, M.M. Wong, U. Chowdhury, C. Collins, T. Li, K. Kwon, B.S. Shelton, T.G. Zhu, J.C. Campbell, and R.D. Dupuis, "Back illuminated AlGaN solar-blind photodetectors." *Appl. Phys. Lett.* **77,** 1090-1092 (2000)

Appendix A. Introduction to dislocations

A thorough introduction to the concept of defects is given in the book "Introduction to Dislocations" by Derek Hull[1], and is summarized here.

A.1 Crystal models

Crystal structures can be described in many ways. The atoms comprising the crystal can, for example, be considered as points (the atomic core positions) or as spheres, encompassing the entire spatial extent of each atom. Each of these representations is useful in coming to an understanding of crystal defects. We consider first the crystal lattice model. The lattice is made up of points (representing atoms) and lines (representing bonds), and each lattice formation can be described in terms of a unique unit cell. The unit cell is the smallest division of the lattice into repeated, identical parallelepipeds. Alternatively, with the sphere model, the crystal can be considered as a stack of atomic layers. The crystal is then uniquely identified by description of the atomic arrangement within a layer and the placement of consecutive layers relative to each other. Figure A.1 gives examples of unit cells and of an ABAB… stacking sequence.

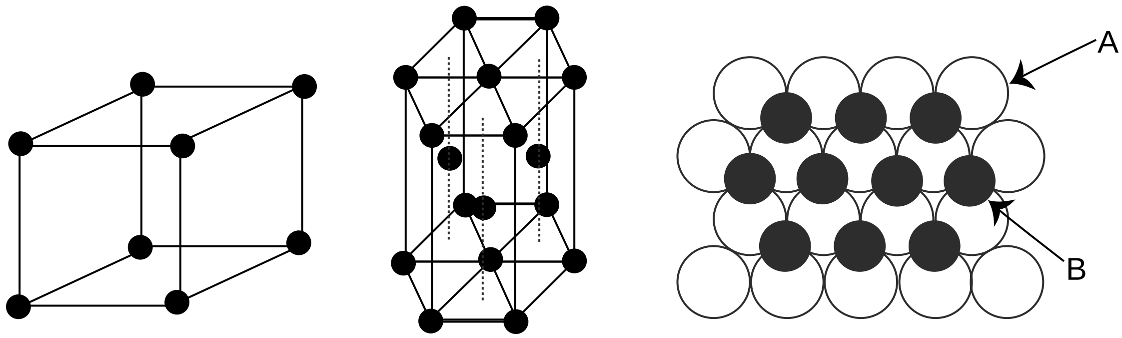

a) b) c)

Figure A.1 Crystal models. (a) Unit cell for the simple cubic crystal structure. (b) Unit cell for the close-packed hexagonal crystal structure. (c) The stacking sequence (ABAB…) of the closed-packed hexagonal crystal structure.

A.2 Crystal defects

A perfect crystal would have all the atoms sitting in the correct positions defined by the crystal type. However, real crystals have lattice imperfections - disorder in the atomic planes or the atomic arrangement. These imperfections include point defects, stacking faults, and dislocations.

A.2.1 Point defects and stacking faults

Point defects in a semiconductor crystal occur when an atomic site is vacant or substituted, or an interstitial site is occupied. Stacking faults, which are surface defects, occur when the regular sequence of close-packed crystal plane stacking is interrupted.

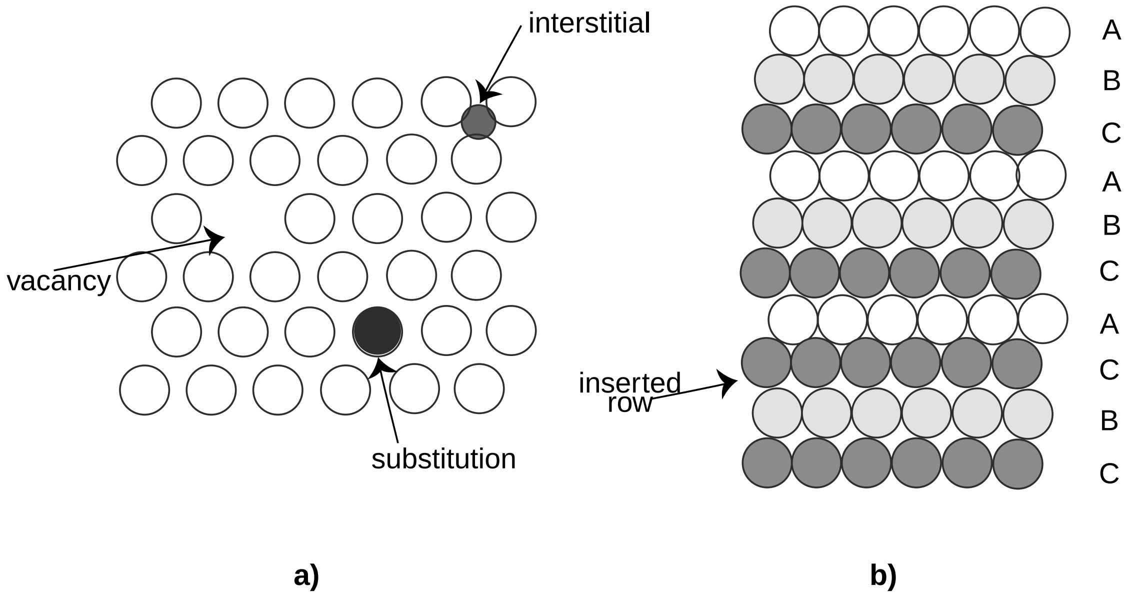

Figure A.2 (a) Examples of point defects – interstitial impurity, vacancy, substitutional impurity. (b) Example of an extrinsic stacking fault – an extra "C" row has been inserted.

In Figure A.2a the interstitial and substitional defects have been shown as impurities. In fact, interstitial defects can arise by introduction of impurities or by displacement of the parent atoms comprising the lattice. Similarly, substitutions can be from impurities or, in the case of ionic crystals, from substitution of cations for anions and vice versa. In Figure A.2b the stacking fault shown is an extrinsic fault, caused by the introduction of an extra layer. That is, the sequence ABCABCABC… is now ABCABCA**C**BC... Intrinsic stacking faults (not shown) occur through removal of a layer, for example ABCABCBC…

A.2.2 Dislocations

Threading dislocations - with which this chapter is primarily concerned - are linear lattice deformations, the two basic geometries of which are edge and screw dislocations, formed by the application of a shear stress to the lattice. Figure A.3[1] illustrates these for a simple cubic lattice.

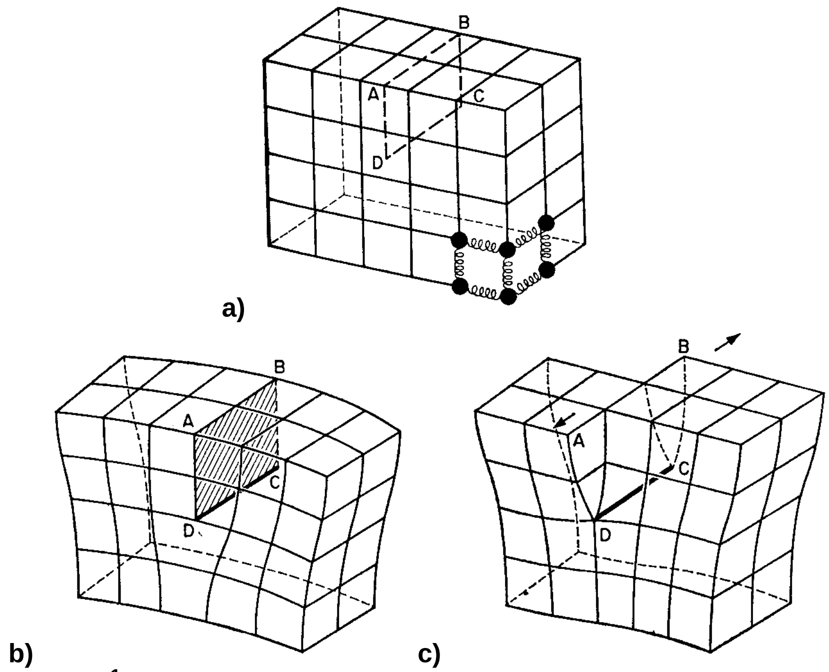

Figure A.3[1] Illustration of edge and screw dislocations in a simple cubic lattice. a) Ball (atoms) and spring (bonds) model has been simplified to straight lines representing the simple cubic lattice structure. The bonds have been broken at the intersection of the plane ABCD with the lattice. b) Edge dislocation - formed by insertion of an extra half-plane of atoms at ABCD. c) Screw dislocation - formed by a displacement of the crystal planes on either side of ABCD.

In Figure A.3a the ball and spring model (representing atoms and bonds), shown in the lower right-hand corner, has been simplified to straight lines representing the bonds. The atoms are understood to be the points at the intersections of the straight lines. The bonds have been broken at the intersection of the plane ABCD with the lattice, and it is at this break in the lattice that the dislocations are formed – an edge dislocation in Figure A.3b and a screw dislocation in Figure A.3c.

Edge dislocations correspond to the insertion or removal of a partial plane of dislocations from the crystal, which displaces the planes on either side. In Figure A.3b a partial plane of dislocations has been inserted into the break formed by the plane ABCD. This is a positive edge dislocation. A negative edge dislocation would occur if an extra plane were inserted below ABCD (in which case ABCD would represent the original position of a plane of atoms that had been removed).

Screw dislocations occur when part of two adjacent lattice planes are shifted laterally with respect to each other. In Figure A.3c the crystal on one side of ABCD has been displaced relative to the crystal on the other side, with the displacement in the direction of the line $\overline{AB}$. To understand how this is a screw dislocation some visualisation is necessary. Imagine taking the line $\overline{AD}$ and rotating it anticlockwise with $\overline{DC}$ as the axis of rotation. After 360° rotation it has moved down one lattice position in an unbroken plane. With successive anticlockwise rotations this line moves through the crystal on a single surface helicoid. Each anticlockwise circuit advances the helix by one plane, and thus the line DC is a left-handed screw dislocation. For a right-handed screw dislocation a clockwise circuit advances the helix.

A.3 Burgers circuits

The previous discussion contributed towards a physical understanding of the dislocations. By far the most common method of defining dislocations is through the Burgers circuit. This is an atom-to-atom path forming a closed loop taken in a crystal containing dislocations. Figure A.4[1] demonstrates the effect of an edge dislocation on the Burgers circuit.

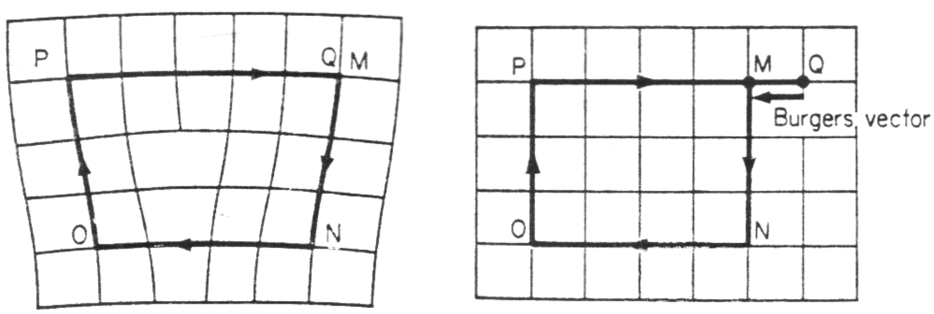

a) b)

Figure A.4[1] Atom-to-atom path (Burgers circuit) MNOPQ taken in a) a dislocated crystal, with an edge dislocation contained within the path loop, and b) a perfect crystal. The Burgers vector for the former is given by the failure in path closure in the latter.

The Burgers vector is obtained by comparison of the Burgers circuit incorporating the dislocation to the same circuit in a perfect crystal. In Figure A.4a the closed loop $\overline{\text{MNOPQ}}$ contains a dislocation. When this same atom-to-atom path is followed in a perfect crystal (Figure A.4b) the circuit does not close. This will occur if and only if the original circuit contained a dislocation. The closure failure $\overline{QM}$ is the Burgers vector. Because it is an edge dislocation, the vector is perpendicular to the line of the dislocation ($\overline{DC}$ in Figure A.3b). In the case of a screw dislocation, the Burgers vector will be parallel to the line of the dislocation. For a mixed character dislocation, the Burgers vector will be at an arbitrary angle to the dislocation line.

The dislocations discussed in the thesis are pure edge dislocations and mixed-character dislocations. Pure screw dislocations are not known to occur in GaN or its alloys.

---

1. D. Hull. *Introduction to Dislocations* (1965), Pergamon Press, Oxford

Appendix B. Processing

B.1 Activation

1.00 **Solvent Clean**
1.01 Soak in acetone (ultrasonic bath) for 1 minute
1.02 Soak in isopropanol (ultrasonic bath) for 1 minute
1.03 Rinse in running DI water for 1 minute
1.04 Blow dry in N_2
1.05 Bake; 120° oven for 5 minutes

2.00 **Activate p-layer**
2.01 Clean PECVD chamber (30 minute clean)
2.02 Load wafer in evaporation chamber
2.03 Evaporate 1000Å SiO_2
2.04 Anneal in RTA (950°C, 3 minutes, N_2 atmosphere)
2.05 Soak in BHF for 5 minutes
2.06 Rinse in running DI for 1 minute
2.07 Blow dry in N_2

B.2 Ohmic p-contacts

1.00 **Solvent Clean**
1.01 Soak in acetone (ultrasonic bath) for 1 minute
1.02 Soak in isopropanol (ultrasonic bath) for 1 minute
1.03 Rinse in running DI water for 1 minute
1.04 Blow dry in N_2
1.05 Dehydration bake; 120° oven for 10 minutes
1.06 Cool samples, 2 minutes

2.00 **Open Windows for p-contact (Image Reversal)**
2.01 Spin HMDS; 40s@6000rpm
2.02 Softbake; 95° hotplate for 1 minute
2.03 Spin photoresist AZ5214; 40s@6000rpm
2.04 Softbake; 95° hotplate for 1 minute
2.05 Remove photoresist at edges (“edge bead”) with acetone swab
2.06 Expose with mask (10s@7.5W/cm^2 UV light)
2.07 Image reversal bake; 110° hotplate for 1 minute
2.08 Flood expose (30s@7.5W/cm^2 UV light)
2.09 Develop in AZ400K:DI 1:5.5, 50seconds
2.10 Rinse in running DI for 1 minute; blow dry in N_2

2.11 Second exposure: flood expose (1 minute@7.5W/cm^2 UV light)
2.12 Develop in AZ400K:DI 1:5.5, 15s
2.13 Rinse in running DI for 1 minute; blow dry in N_2

3.00 Acid Dip
3.01 Soak in HCl for 20s
3.02 Rinse in DI water for 5 minutes
3.03 Blow dry in N_2

4.00 Metal Evaporation
4.01 Load wafer in electron beam evaporation chamber; pump down
4.02 Evaporate 200Å Pd @ 1-2 Å/s
4.03 Evaporate 2000Å Au @ 5-7 Å/s

5.00 Liftoff
5.01 Soak in acetone for 5 minutes
5.02 Finish acetone soak with ultrasonic dip, 10s
5.03 Rinse in isopropanol (ultrasonic bath) for 1 minute
5.04 Rinse in running DI water for 1 minute
5.05 Blow Dry in N_2
5.06 Anneal in RTA (650°C, 1 minute, N_2 atmosphere)

B.3 Transparent p-contact layer

For transparent contact layer: same procedure as ohmic p-contacts (B.2), but evaporate 30Å Pd @ 0.1-0.2Å/s, with no Au (steps 4.02-4.03). No anneal in RTA (step 5.06).

B.4 Mesa etch

1.00 Open Windows for Mesa Etch
1.01 Spin photoresist AZ4110; 40s@6000rpm [or AZ4330 if etch thickness>0.5μm]
1.02 Softbake; 95° hotplate for 1 minute
1.03 Remove photoresist at edges (“edge bead”) with acetone swab
1.04 Expose with mask (10s@7.5W/cm^2 UV light) [or 39s if AZ4330]
1.05 Develop in AZ400K:DI 1:4, 50s [or 70s if AZ4330]
1.06 Rinse in running DI for 1 minute; blow dry in N_2
1.07 Hardbake; 120° oven for 10 minutes

2.00 **Mesa Etch**
2.01 Load wafer in RIE chamber; pump down
2.02 Etch to n-GaN (200W, 5mTorr, 10sccm $Cl_2 \rightarrow$ 1200Å/minute etch rate)
2.03 Soak in acetone (ultrasonic bath) for 1 minute
2.04 Soak in isopropanol (ultrasonic bath) for 1 minute
2.05 Rinse in running DI water for 1 minute
2.06 Blow dry with N_2

B.5 Ohmic n-contacts

1.00 **Solvent Clean**
1.01 Soak in acetone (ultrasonic bath) for 1 minute
1.02 Soak in isopropanol (ultrasonic bath) for 1 minute
1.03 Rinse in running DI water for 1 minute
1.04 Blow dry in N_2
1.05 Bake dry @ 120 deg for 10 minutes
1.06 Cool samples, 2 minutes

2.00 **Open Windows for n-contact (Image Reversal)**
2.01 Spin HMDS; 40s@6000rpm
2.02 Softbake; 95° hotplate for 1 minute
2.03 Spin photoresist AZ5214; 40s@6000rpm
2.04 Softbake; 95° hotplate for 1 minute
2.05 Remove photoresist at edges ("edge bead") with acetone swab
2.06 Expose with mask (10s@7.5W/cm^2 UV light)
2.07 Image reversal bake; 110° hotplate for 1 minute
2.08 Flood expose (30s@7.5W/cm^2 UV light)
2.09 Develop in AZ400K:DI 1:5.5, 50seconds
2.10 Rinse in running DI for 1 minute; blow dry in N_2

3.00 **Descum**
3.01 Load in plasma etch chamber
3.02 Descum: 30s in O_2, 300torr; 100V

4.00 **Metal Evaporation**
4.01 Load wafer in electron beam evaporation chamber; pump down
4.02 Evaporate 100Å Ti @ 1.5Å/s
4.03 Evaporate 2000Å Al @ 5-7Å/s
4.04 Evaporate 500Å Ni @ 1.5Å/s
4.05 Evaporate 2000Å Au @ 5-7Å/s

5.00 **Liftoff**
5.01 Soak in acetone for 5 minutes
5.02 Finish acetone soak with ultrasonic dip, 10s
5.03 Rinse in isopropanol (ultrasonic bath) for 1 minute
5.04 Rinse in running DI water for 1 minute
5.05 Blow Dry in N_2

B.6 Sidewall passivation

1.00 **Solvent Clean**
1.01 Soak in acetone (ultrasonic bath) for 1 minute
1.02 Soak in isopropanol (ultrasonic bath) for 1 minute
1.03 Rinse in running DI water for 1 minute
1.04 Blow dry in N_2
1.05 Bake; 120° oven for 5 minutes

2.00 **Deposit SiO_2 by PECVD**
2.01 Clean PECVD chamber (30 minute clean)
2.02 Load wafer in evaporation chamber with Si blank
2.03 Evaporate 1000Å-4000Å SiO_2 (as required by mesa height)
2.04 Ellipsometry of SiO_2 thickness on Si blank

3.00 **Long-Bake Photolithography for SiO_2 Via Etch**
3.01 Rinse in running DI water for 1 minute
3.02 Blow dry in N_2
3.03 Dehydration bake; 120°C oven for 2 hours
3.04 Cool samples, 2 minutes
3.05 Spin HMDS; 40s@6000rpm
3.06 Softbake; 95°C hotplate for 5 minutes
3.07 Spin photoresist AZ5214; 40s@6000rpm
3.08 Softbake; 95°C hotplate for 1 minute
3.09 Softbake; 90°C oven for 2 hours
3.10 Remove photoresist at edges (“edge bead”) with acetone swab
3.11 Expose with mask (10s@7.5W/cm^2 UV light)
3.12 Image reversal bake; 110° hotplate for 1 minute
3.13 Flood expose (30s@7.5W/cm^2 UV light)
3.14 Develop in AZ400K:DI 1:5.5, 50seconds
3.15 Rinse in running DI for 1 minute; blow dry in N_2

4.00 **Descum**
4.01 Load in plasma etch chamber
4.02 Descum: 30s in O_2, 300torr; 100V
4.03 Hardbake; 120° oven for 10 minutes

5.00 SiO_2 Etch
5.01 Remove SiO_2 from Si test wafer using pad etch solution (recipe below); record the etch time
5.02 Remove SiO_2 from samples using pad etch solution (Etch time: add 5s to time required for Si wafer)
5.03 Rinse in running DI for 1 minute
5.04 Blow Dry in N_2

6.00 Remove Photoresist
6.01 Soak in acetone (ultrasonic bath) for 1 min
6.02 Soak in isopropanol (ultrasonic bath) for 1 min
6.03 Rinse in running DI water for 1 minute
6.04 Blow dry with N_2

B.7 Contact Pad Deposition

For contact pad deposition: same procedure as ohmic n-contact deposition (B.5), but evaporate 3000-4000Å Au, and no Al or Ni (steps 4.03-4.05).

B.8 Pad Etch Recipe

The pad etch is an alternative SiO_2 etch to BHF – it does not etch metal contacts such as the Ti/Al/Ni/Au and Pd/Au used here.

Recipe (percentages by weight): 13.5% ammonium fluoride, 31.8% acetic acid, 4.2% ethylene glycol, and 50.5% deionised water.